STUDIES OF ENERGY RECOVERY LINACS AT JEFFERSON LABORATORY

1 GeV Demonstration of Energy Recovery at CEBAF and Studies of the Multibunch, Multipass Beam Breakup Instability in the 10 kW FEL Upgrade Driver

---

A Dissertation

Presented to

The Faculty of the Department of Physics

The College of William and Mary in Virginia

In Partial Fulfillment

Of the Requirements for the Degree of

Doctor of Philosophy

---

by

Christopher D. Tennant

2006

APPROVAL SHEET

This dissertation is submitted in partial fulfillment of

the requirements for the degree of

Doctor of Philosophy

Christopher D. Tennant

Approved by the Committee, October 2006

Keith Griffioen, Chair

David Armstrong

Fred Dylla

Lia Merminga

Robert Welsh

David Douglas, Jefferson Laboratory

DEDICATION

To my wife Danielle and my mother Karen, for their ceaseless support and love and for the countless sacrifices they have made on my behalf.

TABLE OF CONTENTS

ACKNOWLEDGMENTS

First and foremost I must thank my committee for their wise counsel and guidance over the past several years. It is incumbent upon a student's advisors to choose an appropriate topic of research, and I could not have asked for a more intriguing and rewarding topic to study than the one presented in this dissertation.

Specifically I would like to thank David Douglas who, being the first person I met at Jefferson Laboratory, has literally been there for me from day one. Despite his eternal pessimism, it has been a privilege to learn from one of the best in the "ERL business". I would also like to thank Lia Merminga, whose eternal optimism, steadfastness and demand for perfection have ultimately led to this dissertation. And while their work has largely been behind the scene, I am equally grateful to Fred Dylla and Keith Griffioen for their guidance and quiet leadership.

Although we worked less than three years together, the results presented in this dissertation would not have been possible without Eduard Pozdeyev. I gratefully acknowledge his unwavering support, guidance and friendship during the course of my studies. I suspect there have never been two people who have devoted so much time as we did looking at a screen - computer, network analyzer, spectrum analyzer or oscilloscope - over the course of three years.

I must also thank Raphael Littauer, with whom I had the great privilege to work under while doing research as an undergraduate. The wealth of information which he shared so enthusiastically with me, in addition to his charming personality and pleasant demeanor, greatly influenced my decision to pursue a career in the field of accelerator physics.

There are a number of other individuals whose help over the past several years has been indispensable and I am grateful to them all. They are Kevin Beard, Steve Benson, Jim Coleman, Kevin Jordan, Geoffrey Krafft, Tom Powers, Richard Walker, Haipeng Wang and Byung Yunn from Jefferson Laboratory, Stefan Simrock from DESY, Todd Smith from Stanford and John Dirk Walecka from The College of William and Mary. Thank you.

LIST OF TABLES

LIST OF FIGURES

ABSTRACT

An energy recovering linac (ERL) offers an attractive alternative for generating intense beams of charged particles by approaching the operational efficiency of a storage ring while maintaining the superior beam quality typical of a linear accelerator. Two primary physics challenges exist in pushing the frontier of ERL performance. The first is energy recovering a high energy beam while demonstrating operational control of two coupled beams in a common transport channel. The second is controlling the high average current effects in ERLs, specifically a type of beam instability called multipass beam breakup (BBU). This work addresses both of these issues.

A successful 1 GeV energy recovery demonstration with a maximum-to-injection energy ratio of 51:1 was carried out on the Continuous Electron Beam Accelerator Facility at Jefferson Laboratory in an effort to address issues related to beam quality preservation in a large scale system. With a 1.3 km recirculation length and containing 312 superconducting radio frequency (SRF) cavities, this experiment has demonstrated energy recovery on the largest scale, and through the largest SRF environment, to date.

The BBU instability imposes a potentially severe limitation to the average current that can be accelerated in an ERL. Simulation results for Jefferson Laboratory's 10 kW free electron laser (FEL) Upgrade Driver predict the occurrence of BBU below the nominal operating current. Measurements of the threshold current are described and shown to agree to within 10% of predictions from BBU simulation codes. This represents the first time the codes have been benchmarked with experimental data. With BBU limiting the beam current, several suppression schemes were developed. These include direct damping of the higher-order mode using two different cavity-based feedbacks and modifying the electron beam optics to reduce the coupling between the beam and mode. Specifically the effect of implementing (1) point-to-point focusing (2) a reflection of the betatron planes about 45° and (3) a rotation of the betatron planes by 90° is measured. Each method increased the threshold current for stability. Beam optical control methods proved to be so effective that they are routinely used in the operation of the 10 kW FEL Upgrade.

STUDIES OF ENERGY RECOVERY LINACS AT JEFFERSON LABORATORY

CHAPTER 1

Introduction

An increasing number of scientific applications require intense electron beams of superior quality (extremely small 6-dimensional phase space), for the investigation of fundamental processes as well as the generation of highly coherent, high average brightness photon beams. These applications include electron-ion colliders for nuclear and particle physics research, and synchrotron radiation sources and free electron lasers (FEL) for the generation of photon beams for atomic and molecular physics and biology. Traditionally the demands for beams with these characteristics have been met by storage rings, which over the years have been performing at increasingly high quality. However, the ultimate performance of storage rings is limited by the fact that electrons are stored for many hours in an equilibrium state. The equilibrium between radiation damping and quantum excitation sets a fundamental limit on the minimum emittance and bunch length that can be achieved.

On the other hand, the linear accelerator (linac), another traditional accelerator, can deliver beams with very small emittance, energy spread, and very short bunch length, as these properties are established by phenomena in the low-energy electron source and can be well preserved during acceleration to high energy. How-

ever, linacs are limited to accelerating small amounts of average beam current due to the prohibitively expensive radio-frequency (RF) power required.

An energy recovering linac (ERL) is a powerful alternative accelerator concept which combines the desirable characteristics of both storage rings and linacs, by having the potential to accelerate hundreds of milliamperes of average current to several giga-electron volts in energy while maintaining excellent beam quality.

1.1 Energy Recovering Linear Accelerators

The idea of energy recovery was first proposed in 1965 for use in a collider [1]. While such a collider has yet to be realized, within the last decade energy recovery has found a niche in drivers for light sources. A schematic for a generic ERL based light source is given in Fig. 1.1. Electrons are generated in a high brightness injector, accelerated through a linac and then transported to a region where the desired radiation is generated (e.g. an undulator or a wiggler). After performing their intended purpose, the electrons are returned to the linac 180° out of phase with respect to the RF accelerating field for energy recovery. At the exit of the linac, the energy of the decelerated beam is approximately equal to the injection energy and the beam is directed to a beam dump. In ERLs the decelerated beam cancels the beam loading effects of the accelerated beam. Therefore ERLs can, in principle, accelerate very high average currents with only modest amounts of RF power.

Because the net RF current seen in the linac is negligible, high average currents can be accelerated economically. Furthermore, since the electron beam only exists in the accelerator for a short time (typically two passes), the equilibrium that is unavoidable in a storage ring does not have time to develop. Thus the beam quality in an ERL is determined, to a large extent, by the injector. This combination of

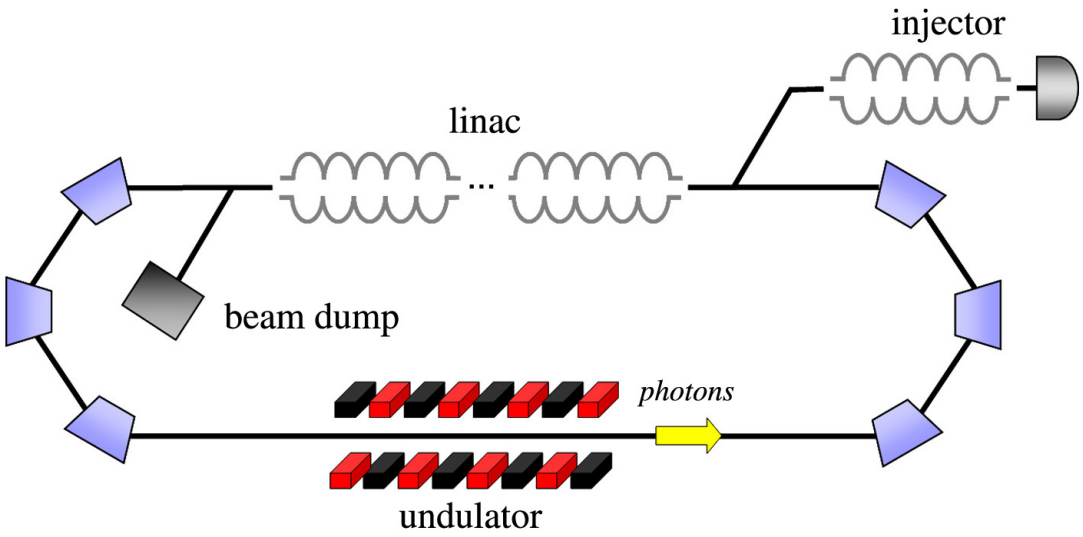

FIG. 1.1: Schematic of a generic light source based on an energy recovering linac driver.

high average current capability and high beam quality make ERLs attractive as, among other things, drivers for oscillator FELs and synchrotron light sources.

Another advantage of ERLs results from the fact that the energy recovered beam loses energy as it gets decelerated and is dumped at an energy close to its injection energy. Thus the beam dump design is simplified because the energy of the beam is reduced by a factor of (E_{max}/E_{inj}) where E_{max} is the energy of the beam before energy recovery and E_{inj} is the injection energy.

Energy recovering linacs are not without their challenges, however. One of the most severe limitations to ERL performance is a form of regenerative beam breakup (BBU), called multipass, multibunch BBU, and is the primary subject of this dissertation.

The mechanism for BBU begins when a beam bunch passes through an RF cavity off-axis, thereby exciting dipole higher-order modes (HOMs). The magnetic field of an excited mode deflects following bunches traveling through the cavity. Depending on the details of the machine optics, the deflection produced by the

mode can translate into a transverse displacement at the cavity after recirculation. The recirculated beam induces an HOM voltage which depends on the magnitude and direction of the beam displacement. Thus, the recirculated beam completes the feedback loop which can become unstable if the average beam current exceeds the threshold current for stability.

Beam breakup is of particular concern in the design of high average current ERLs utilizing superconducting RF (SRF) technology. If not sufficiently damped by the HOM couplers, dipole modes with quality factors several orders of magnitude higher than in normal conducting cavities can exist, providing a real threat for BBU to develop. The effect of the instability is to limit the average current that can be accelerated, which can severely affect machine performance when this occurs at currents below the designed operational current.

1.2 Superconducting Radio Frequency Technology

While in principle there is nothing that prohibits the use of normal conducting RF cavities for energy recovery, superconducting RF has many advantages which have made it the technology of choice for nearly all ERL designs, past and present. The primary features which make it so attractive are the high quality factor of the accelerating mode and the ability to operate in continuous wave (cw) mode while maintaining relatively high accelerating gradients.

The basic building block of the linacs at Jefferson Laboratory's electron accelerators - the Continuous Electron Beam Accelerator Facility (CEBAF) and the 10 kW FEL Upgrade Driver - is the SRF cavity shown in Fig. 1.2. The standard CEBAF style cavity is based on a Cornell University design and consists of five elliptically

FIG. 1.2: A CEBAF 5-cell cavity with a waveguide higher-order mode coupler (left) and fundamental power coupler (right).

shaped resonators, or cells, which are coupled. The cavity is a standing wave structure and operates in the π-mode with a fundamental frequency of 1497 MHz. The elliptical cell shape prevents multipactoring, which plagued early cavity designs, and also provides good mechanical rigidity to combat the effects of external mechanical vibrations, known as microphonics [2]. Each cavity is equipped with two couplers, a fundamental power coupler (FPC) on one end and an HOM coupler on the other. The cavities are constructed from niobium which becomes superconducting below 9.2 K. Cavities are hermetically paired and installed in cryounits where they are immersed in a liquid helium bath at 2.1 K. A single cryomodule is comprised of four cryounits. Each of the two linacs in CEBAF contain 20 cryomodules, while the FEL Upgrade Driver's linac consists of 3 cryomodules.

A brief introduction to some of the most important figures of merit used to characterize an SRF cavity is given below.

1.2.1 Figures of Merit

Radio frequency accelerating structures utilize the electromagnetic fields within microwave cavities to accelerate beams of charged particles. One of the most important properties of a cavity is the accelerating gradient, which is quoted in units of accelerating voltage per meter. Typical values for SRF cavities in operation at CEBAF are 7 MV/m, although gradients exceeding 15 MV/m have been demonstrated in the FEL Upgrade Driver [3]. The maximum energy gained through a single cavity by an electron, for example, is ($e \times$ the gradient $\times$ the length of the cavity).

Another important figure of merit is the quality factor of cavity modes. The unloaded quality factor is defined as the ratio of the energy stored to the energy dissipated in the cavity walls in one RF period and is written as

$$Q_o = \frac{\omega U}{P_{diss}} \tag{1.1}$$

where U is the energy stored in the cavity, ω is the angular frequency of the mode and P_{diss} is the power dissipated on the cavity walls. Often it is more useful to quote the loaded quality factor of a mode which takes into account the total power loss due to leaks in the cavity couplers in addition to the ohmic heating of cavity walls. The loaded Q is defined as

$$Q_L = \frac{\omega U}{P_{tot}} \tag{1.2}$$

where P_{tot} is the total power dissipated. The Q_L indicates how many oscillations it will take for the mode to dissipate its stored energy. For a cavity whose RF power source is turned off, the stored energy evolves as

$$\frac{dU}{dt} = -P_{tot} = -\frac{\omega U}{Q_L}. \tag{1.3}$$

The solution to Eq. (1.3) is

$$U(t) = U_o e^{-t/\tau_L} \tag{1.4}$$

where U_o is the stored energy at $t = 0$ and $\tau_L = Q_L/\omega$, is the decay time constant. Because SRF cavities are characterized by their very high quality factors, they are exceptionally good at storing energy. For example, an SRF cavity operating at 1500 MHz with a Q_L of $2{\times}10^7$ would have a time constant of 13 ms. On the other hand, for a normal conducting cavity operating at the same frequency, the loaded Q is typically 3 orders of magnitude lower and leads to a time constant of 13 μs. While a high quality factor for the accelerating mode is desirable, care must be taken to reduce, or damp, the quality factors of HOMs. If not sufficiently damped, the energy deposited into these modes by the beam will remain on time scales long enough such that multibunch instabilities, like beam breakup, develop.

The shunt impedance is a quantity used to characterize losses in a cavity and is defined as

$$R_a = \frac{V_{acc}^2}{P_{diss}} \tag{1.5}$$

where V_{acc} is the accelerating voltage and P_{diss} is the power dissipated on the cavity walls. From Eq. (1.5) it is clear that the goal is to maximize the shunt impedance for the accelerating mode in order to minimize the power dissipated. The reverse is true for higher-order modes, where the aim is to decrease the shunt impedance. Taking the ratio of Eq. (1.5) and Eq. (1.1) results in another useful figure of merit

$$\frac{R_a}{Q_o} = \frac{V_{acc}^2}{\omega U} \tag{1.6}$$

which depends solely on the geometry of the cavity. The ratio (R/Q) of a mode is used to indicate the extent to which the mode is excited by passing charges. In that

sense it measures the strength of the coupling between the mode and beam. One of the primary challenges in designing a cavity is to ensure that the accelerating mode has a large (R/Q) while minimizing the (R/Q) of higher-order modes.

1.2.2 ERLs Utilizing SRF Technology

There is an increasing demand for accelerators to provide high duty factor, or cw, beams. The duty factor refers to the percentage of time the beam is on and a continuous wave beam is one in which the duty factor is 100%. In this case the beam pulse is continuously on at the RF repetition rate or at one of its subharmonics. The high Q_o of SRF cavities means very little power is dissipated on the cavity walls, which in turn allows cavities to operate in cw mode while maintaining relatively high gradients. This is in stark contrast to normal conducting cavities. Because of the resistive heating in the normal conducting material (e.g. copper), the linac can only operate in pulsed mode, requiring large time gaps between accelerated bunches to allow the cavities to cool. Operating copper cavities in cw mode limits gradients to less than 2 MV/m. On the other hand, at the Jefferson Laboratory FEL SRF-based Driver, cw beam is provided by operating up to the 20^{th} subharmonic of the fundamental RF frequency, while maintaining cavity gradients in excess of 10 MV/m. Thus, the operation of a high duty factor accelerator necessitates the use of SRF technology.

Another important advantage of SRF cavities is the ability to increase the beam aperture. While this decreases the (R_a/Q_o) of the fundamental mode, the effect can be absorbed by the extremely high Q_o since the goal is to minimize the dissipated power, which from Eq. (1.5) is inversely proportional to $(R_a/Q_o)Q_o$. A larger aperture ensures increased beam quality by reducing the short range wakefields and thereby reducing emittance growth along the linac, it ensures greater beam stability

by reducing the impedance of HOMs, and reduces beam loss from scraping. All of these benefits combine to make it possible to accelerate and preserve a high quality beam.

Furthermore, in SRF cavities there is a high RF power to beam power efficiency compared to their normal conducting counterparts. As a way to quantify the efficiency of an ERL, the concept of a multiplication factor is used and defined as [4]

$$\kappa = \frac{P_b}{P_{RF}} \approx \frac{I_o(E_{max}/e)}{I_o(E_{inj}/e) + P_{RF,linac}} \tag{1.7}$$

where P_b is the power of the beam and P_{RF} is the power required to operate the RF cavities. The beam power is given by the product of the average beam current and the maximum energy (i.e. before energy recovery) divided by the charge of the electron, e. For a machine operating in the regime of perfect energy recovery (the accelerated and energy recovered beams cancel), P_{RF} consists of two terms; the first is the power required to accelerate a beam current I_o in the injector (which is not energy recovered) to an energy E_{inj} and $P_{RF,linac}$, is the power required to establish the accelerating field in the linac cavities. Note that the last term is independent of beam current. This term is inversely proportional to Q_L which, in SRF cavities, is typically three orders of magnitude greater than in normal conducting cavities. Consequently, for an ERL with energy and average beam current comparable to a storage ring, using SRF technology would ensure an efficiency several orders of magnitude greater than for the same machine based on normal conducting technology.

1.3 Historical Development of ERLs

To provide the proper context for the research presented in this dissertation, a brief historical overview of the development of ERLs is given [5]. Particular attention will be given to ERLs at Jefferson Laboratory where, for the past decade, the

implementation of energy recovery has been most active.

The first demonstration of energy recovery occurred at Chalk River Nuclear Laboratories in 1977 using a two-pass reflexotron [6]. In a reflexotron the beam passes through an accelerating structure and is returned through the structure in the opposite direction by a 180° reflecting magnet. By changing the distance of the reflecting magnet from the accelerating structure, the phase of the beam relative to the accelerating field can be made to generate either energy doubling or energy deceleration and recovery. Using this method, output energies between 5 MeV (with energy recovery) and 25 MeV (with energy doubling) were achieved.

In 1985 a 400 MeV electron beam was energy recovered to 23 MeV at the MIT-Bates Linac as part of an experiment to operate the recirculation system under a variety of conditions [7]. A unique three pass beam operation scenario was also demonstrated by producing a re-injection phase of 90° relative to the accelerating field with the recirculator. In this way, the second pass beam traveled through the linac without feeling any acceleration. A third pass beam was re-injected into the linac with a 180° phase difference relative to the accelerating field and energy recovered. Beam transmission was poor on the third pass however, due to the large energy spread acquired.

In 1986, Stanford University's Superconducting Accelerator (SCA) energy recovered 150 μA of average beam current from 55 MeV to 5 MeV [8]. This experiment was significant in that it marked the first time energy recovery had been demonstrated in a superconducting RF environment.

At about the same time, the free electron laser at Los Alamos National Laboratory demonstrated energy recovery in a unique configuration where the decelerated beam deposited energy in a different cavity from which it was accelerated [9]. This scheme represents a departure from the previous examples of "same-cell" energy recovery. Using this setup, they successfully energy recovered 21 MeV to 5 MeV.

Despite its success, this method of energy recovery has not been used since. The subsequent material in this dissertation is focused solely on accelerators utilizing same-cell energy recovery in superconducting RF cavities.

1.3.1 Jefferson Laboratory and ERLs

Over the course of 12 years, from 1993 to 2005, Jefferson Laboratory successfully demonstrated same-cell energy recovery in four different accelerators. Due in large part to the success of the IR FEL Demo in the mid 1990's, there has been a renewed interest in ERLs as drivers for applications ranging from electron-ion colliders, to electron coolers, to light sources and FELs.

As discussed in Section 1.2, combining the principle of energy recovery with SRF cavities leads to an accelerator capable of generating an intense beam with excellent beam qualities in an efficient and economical manner. Initial experience with SRF cavities, however, presented formidable challenges. In the early 1970s, when Stanford University began operation of the SCA, multipactoring in the SRF cavities severely limited the gradients and consequently the final beam energy. To overcome this obstacle, transport elements were installed to recirculate the beam multiple times through the linac [10, 11]. When the beam was recirculated, insufficiently damped HOMs caused beam breakup, thereby limiting the achievable average beam current. Thus, despite the great potential of SRF cavities, the first accelerator to implement SRF technology was limited in beam energy (due to multipactoring) and average beam current (due to BBU).

When in 1985 it was proposed to build a 4 GeV electron accelerator for nuclear physics based on SRF technology at Jefferson Laboratory, a great effort was made to address the issues of implementing SRF technology on such a large scale [12]. By this time Cornell University had designed a cavity using an elliptical cell shape which

all but eliminated multipactoring. And while the Cornell cavity exhibited greater HOM damping than the cavities used in the SCA, much was done to address the potential problem of multipass, multibunch BBU.

During the initial construction of CEBAF, the injector linac was used in conjunction with a single recirculation line to experimentally investigate the problem of BBU [13, 14]. The injector was capable of providing over 200 μA of average beam current. Beam was injected into the linac at 5.5 MeV and accelerated to 43 MeV by two cryomodules. Next, the beam was recirculated and sent through the linac for a second pass where it could either be accelerated to 80 MeV or the recirculator could be configured for energy recovery in which the beam was decelerated to 5.5 MeV. With no energy recovery, over 200 μA was successfully transported through the system. In the energy recovery mode, the average current was limited to 30 μA due to poor transmission of the second pass beam which led to intolerable beam losses. In neither operating scenario were there indications of the development of BBU.

Even before CEBAF was completed, proposals were made for using an SRF linac as a driver for an FEL [15]. In addition to the ability of an SRF linac to maintain superior beam quality, the ability for cw operation opened up the possibility of achieving high average output power while using bunches of modest charge. It had been recognized that invoking energy recovery would increase the system efficiency while at the same time reducing the need for expensive, high power RF sources [16]. An initial design for an ERL-based driver for an FEL at Jefferson Laboratory was developed in 1991 [17]. This design was significant in that it marked the first time energy recovery was implemented as the nominal mode of operation.

By 1998 the Jefferson Laboratory IR FEL Demo successfully energy recovered 5 mA of average beam current through a single cryomodule from 48 MeV to the injection energy of 10 MeV [18]. By the end of 2001, as the IR Demo was being decommissioned to prepare for an upgrade, the machine had operated at, or exceeded,

design parameters, most notably achieving over 2 kW of average IR power.

As a result of the IR FEL Demo's demonstrated success, the attractive features of an SRF linac with energy recovery became apparent. Applications of ERLs were extended to synchrotron radiation sources, electron cooling and electron-ion colliders. However, these new applications require a significant extrapolation of the operating parameters achieved at the FEL, such as beam energy and current.

In 2001, a proposal was put forth to non-invasively test energy recovery on a large scale using CEBAF [19]. Because it is a recirculating linac, operating CEBAF with energy recovery requires only minor modifications. The two major components installed were a magnetic chicane to provide a half-RF wavelength delay and a beam dump. In 2003, 80 μA of average beam current was successfully energy recovered from 1056 MeV to the injection energy of 56 MeV [20]. The experiment demonstrated that large scale energy recovery - through 312 SRF cavities and transported through 1.3 km of beamline - is feasible. The details of this experiment are the topic of Chapter 2.

The most recent ERL at Jefferson Laboratory is the upgrade to the IR FEL Demo. Regarding the driver, the most substantial upgrades are an additional two cryomodules to increase the beam energy to 145 MeV and doubling the injected current from 5 mA to 10 mA. In 2004 with all three cryomodules installed, 7.5 mA of average beam current was energy recovered from 145 MeV to 9 MeV [21]. This represents 1.1 MW of recirculating beam power. Due to insufficiently damped HOMs in the final cryomodule installed, beam breakup has developed at currents below the nominal operating current. The investigation of this instability in the FEL Upgrade is the primary topic of this dissertation and is covered in Chapter 3 through Chapter 7.

1.4 Fundamental ERL Challenges

While ERLs exhibit tremendous potential, there also exist many formidable challenges. Generally speaking, these challenges can be grouped into three categories: the injector, machine optics, and superconducting RF [22]. A brief introduction to some of the most important issues and challenges are discussed below, with particular attention towards applications to light sources. Issues specific to the Jefferson Laboratory FEL Driver will be addressed more fully in Chapter 3.

1.4.1 Injector

The injector includes the gun and an accelerating, or booster, section. The injector is a vital component of an ERL because it determines, to a large extent, the beam quality that can be achieved. There has been much debate with regard to the type of gun best suited for ERL applications. Options include DC, normal conducting RF and superconducting RF guns [23]. While persuasive arguments can be made for each, regardless of the technology chosen, the gun must be able to provide a high brightness, high average current, cw electron beam.

The most mature technology for cw applications is the DC gun which is used at both CEBAF and the FEL at Jefferson Laboratory. The FEL gun has delivered up to 9 mA of cw beam at a repetition rate of 74.85 MHz [24]. Extending the capability of a DC gun to produce a cw electron beam on the order of 100 mA will require increasing the cathode's quantum efficiency and lifetime and designing a suitable drive laser system. Once the electron beam is extracted from the cathode, the challenge will be to generate, and then maintain, a small beam emittance.

1.4.2 Machine Optics

The second category of challenges is machine optics which requires proper management of the 6-dimensional beam phase space throughout the machine. There are three primary regions of interest: the linac optics, the recirculation optics and the merger optics. The linac optics requires a design that cleanly transports two co-propagating beams of different energy. The recirculation optics is vital in maintaining the beam quality delivered to the insertion device (accelerating beam) and then to the beam dump (decelerated, energy recovered beam). Finally, the merger section, where the low energy beam from the injector is merged with the high energy recirculated beam, must be carefully designed to avoid beam degradation.

1.4.3 Superconducting RF

There exist many challenges with regard to SRF technology, including maximizing the cryogenic efficiency, maintaining precise control of cavity fields in the presence of microphonics and Lorentz force detuning, achieving strong HOM damping and efficiently extracting HOM power [25]. The issue of HOM damping is considered specifically as insufficiently damped HOMs lead to BBU - one of the most severe performance limitations of ERLs.

While high Q_o and Q_L can be achieved for the fundamental mode in SRF cavities, an unfortunate consequence is the presence of HOMs with very high Qs as well. This requires strong HOM damping to avoid beam instabilities. Recirculating linacs, and ERLs in particular, are more susceptible to these instabilities because they can support currents approaching, or exceeding, the threshold current.

The instability of greatest concern is transverse, multipass, multibunch beam breakup [26]. This form of BBU was first observed in 1977 at the Stanford SCA [11] and later that year at the University of Illinois' MUSL-2 (Microtron Using a

Superconducting Linac) machine [27]. Most recently, in 2004 beam breakup was observed for the first time in an ERL at the Jefferson Laboratory FEL Upgrade Driver [28].

1.5 Outline

The majority of the proposed applications for ERLs require an order of magnitude higher average beam current and/or an order of magnitude higher beam energy than has currently been demonstrated. Making these extrapolations raises many unanswered questions. The aim of this dissertation is to address issues with respect to both beam energy and average beam current.

Chapter 2 describes an experiment that successfully energy recovered the beam in the CEBAF accelerator. By doing so, issues related to the energy recovery of a high energy beam and the preservation of beam quality of two co-propagating beams through a large-scale transport channel were addressed. In addition, operation with a lowered injection energy was demonstrated, thereby showing the viability of a high maximum-to-injector energy ratio (E_{max}/E_{inj}) of 51:1.

The remaining chapters are dedicated to studying the effects of high average current, specifically the multipass beam breakup instability, in Jefferson Laboratory's ERL-based FEL Upgrade Driver. Chapter 3 provides an overview of the Driver. The Upgrade's predecessor, the IR FEL Demo, set the standard for ERL light sources by achieving a world-record (at the time) 2 kW of average laser power while also serving as a user facility. With the 10 kW FEL Upgrade, the frontier of energy recovering linacs continues to expand. Currently, the Upgrade Driver is the most substantial demonstration of energy recovery in the world, having recovered in excess of 1 MW of beam power.

Chapter 4 derives an analytic model for BBU. Although relatively simple, the

analytic model elucidates many important features of the instability and yields a formula for the threshold current for beam stability. Application of this formula is restricted to simple systems (one cavity containing one HOM) and so it is necessary to use computer simulation codes to analyze more complex systems. A brief overview of three BBU codes developed at Jefferson Laboratory is given. Microwave measurements to characterize the HOMs in the FEL cryomodules were performed and used as inputs to the simulation codes. The results predict the onset of the BBU instability in the Upgrade Driver at 2 mA - well below the design operating current of 10 mA.

Chapter 5 presents the results of experimental measurements to characterize BBU which was observed in the FEL Upgrade first in 2004. The primary goal of the measurements was to benchmark BBU simulation codes with experimental data. To that end, several methods to measure the threshold current for stability were developed. The beam transfer function measurement is described and shown to be a particularly useful technique as it can be used to extract the threshold current for a system while working in a regime where the beam is stable. This is in contrast to the method of measuring growth rates, which requires working in the regime where the beam is unstable. Together, however, these two techniques provide a complementary set of measurements. The measured threshold currents and the threshold current predicted from simulations were shown to agree to within 10% which represents the first time the codes have been benchmarked with experimental data.

With the knowledge that BBU poses a threat to beam operations, Chapter 6 and Chapter 7 describe several BBU suppression techniques that were demonstrated - all with varying degrees of success.

Chapter 6 discusses beam optical suppression techniques that require modifying the electron beam optics in a way so as to prevent the beam from coupling as strongly to harmful HOMs. These include implementing point-to-point focusing which is

straightforward, as well as more complicated coupled optics suppression schemes such as reflecting the betatron planes about 45° and a rotation of the betatron planes by 90°.

Chapter 7 discusses suppression techniques utilizing feedback mechanisms; both cavity- and beam-based. Two cavity-based feedback systems, one using an active circuit and the other using a 3-stub tuner, were experimentally shown to increase the threshold current. Beam-based feedback systems, while used extensively in high average current storage rings, present unique challenges for implementing in ERLs. The threshold current for BBU with feedback is derived and simulation results of the effects of a simple feedback system in an ERL are presented.

Finally, a summary of the contributions of the work presented in this dissertation, some concluding remarks and future directions for research are presented in Chapter 8.

CHAPTER 2

CEBAF with Energy Recovery

2.1 Motivation

High energy (of order GeV), high current (of order 100 mA) beams would require gigawatt-class RF systems in conventional linacs - a prohibitively expensive proposition. Invoking energy recovery alleviates RF power demands, improves linac efficiency and increases cost effectiveness. Yet the previous demonstrations of energy recovery using SRF technology discussed in Section 1.3 were performed on relatively small machines. Consequently the beam energy never exceeded 100 MeV until the recent commissioning of the FEL Upgrade Driver. With the increased interest in using ERLs as drivers for synchrotron light sources, the beam energies must far exceed those presently used in FELs. To bridge the gap between the current state of ERLs, which exist on smaller scales, to the future ERLs, an experiment to energy recover the beam in Jefferson Laboratory's CEBAF machine was proposed [19]. Consisting of 312 cavities and having a circumference of 1.3 km, a successful demonstration of energy recovery in CEBAF is an important step on the path to the next generation of ERLs. Such a demonstration requires addressing issues related

to maintaining adequate control over two co-propagating beams of different energy traveling through a common transport channel while preserving beam quality.

An illustrative plot showing the current state of ERLs and trends towards the future is shown in Fig. 2.1. Each point on the plot marks the maximum energy and maximum average current for energy recovery. Only same-cell energy recovery in SRF cavities is considered. The black markers represent machines where energy recovery has already been demonstrated while the red markers represent proposed ERL based accelerators. Making the leap from the current state of the art to the next generation of ERLs will require roughly an order of magnitude increase in the energy and an order of magnitude in average beam current. To date, the CEBAF with energy recovery (CEBAF-ER) experiment has energy recovered the highest beam energy while the highest average beam current was energy recovered in the Jefferson Laboratory 10 kW FEL Upgrade Driver.

2.1.1 CEBAF Overview

The CEBAF machine at Jefferson Laboratory is a five-pass recirculating linac based on SRF technology. The machine is a dedicated user facility for nuclear physics experiments and is capable of delivering cw beam to three experimental halls simultaneously [29].

Construction of CEBAF commenced in 1987 and by 1995 successful five-pass operation with a 4 GeV beam had been demonstrated. The two innovations which made CEBAF unique at the time were the choice of superconducting RF technology and the use of multipass beam recirculation. The motivation for using multiple beam recirculations was twofold. The first was to reduce the costs associated with implementing a long linac and the second was to reduce the real estate required. Recirculating the beam n times through a linac with an energy gain $1/n$ trades

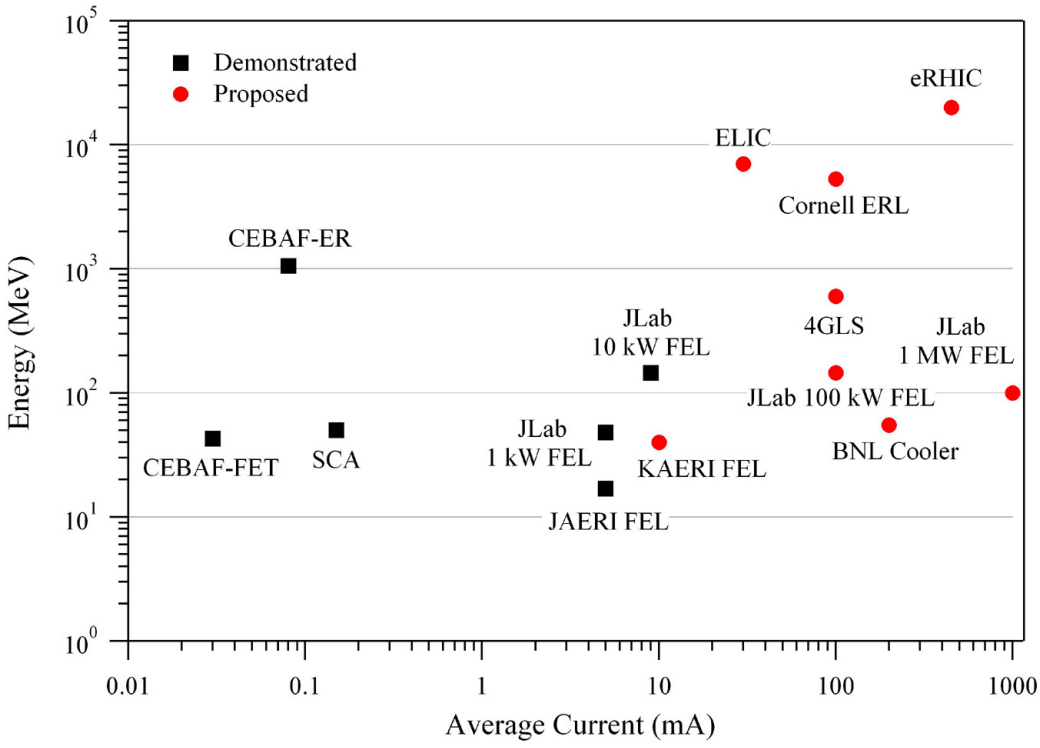

FIG. 2.1: Energy versus average current for machines which have demonstrated energy recovery (black) and for proposed machines (red).

expensive SRF accelerating structures for less expensive magnets required for recirculation.

CEBAF is in a racetrack configuration, comprised of two antiparallel linacs with 180° recirculation arcs connecting them. Because of the difference in energy, each recirculation pass needs to be handled by an independent beam transport system [29]. At the exit of each linac, a spreader region is used to separate the beam via differential vertical bending according to energy into several transport lines. At the end of the arc a recombiner section is used to merge the individual beams and match them for acceleration through the next linac. The arcs themselves consist of a total of nine transport lines (five in the east arc and four in west arc) making it possible for a total of five passes. The arcs were designed to image the beam phase space

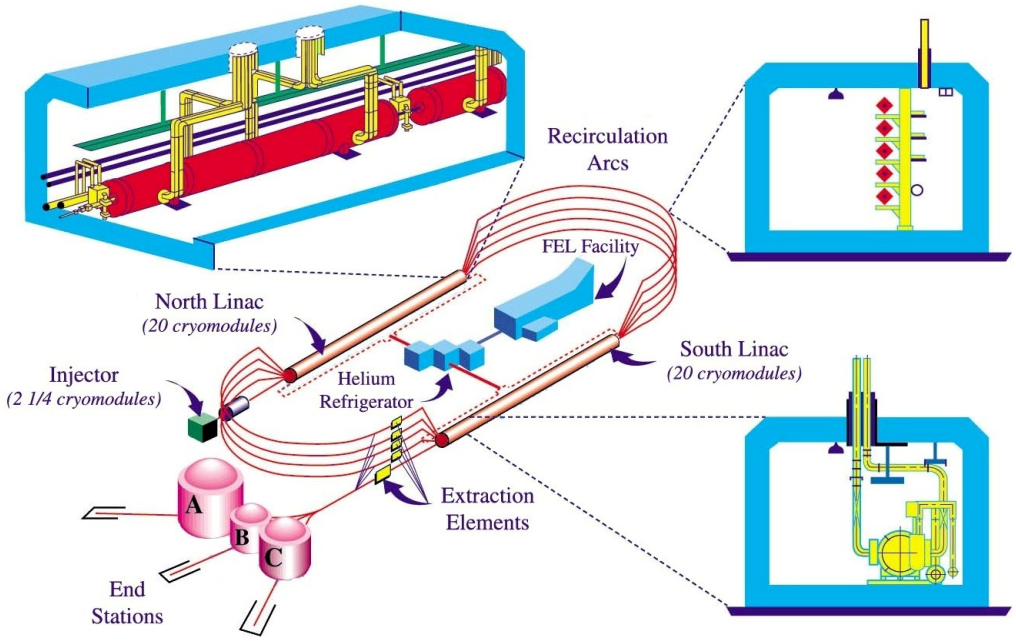

FIG. 2.2: Schematic of the CEBAF accelerator.

from linac to linac. In addition an arc must provide a path length that is equal to an integer multiple of the fundamental RF wavelength to provide proper phasing for beam acceleration. A schematic of the CEBAF machine and the user end stations is depicted in Fig. 2.2.

2.2 Issues and Challenges

In principle, the steps to allow for energy recovery in a recirculating linac like CEBAF are straightforward - simply provide a path length differential of 1/2-RF wavelength after the passing through the north and south linacs. Fortunately the design and construction of CEBAF made provisions for future energy upgrades. To that end, several cryomodule slots were left vacant at the end of the north and south linac. In time, cryomodules will be installed in these spaces to increase the beam energy. The 8.25 m slot length is an ideal space to install the two major components

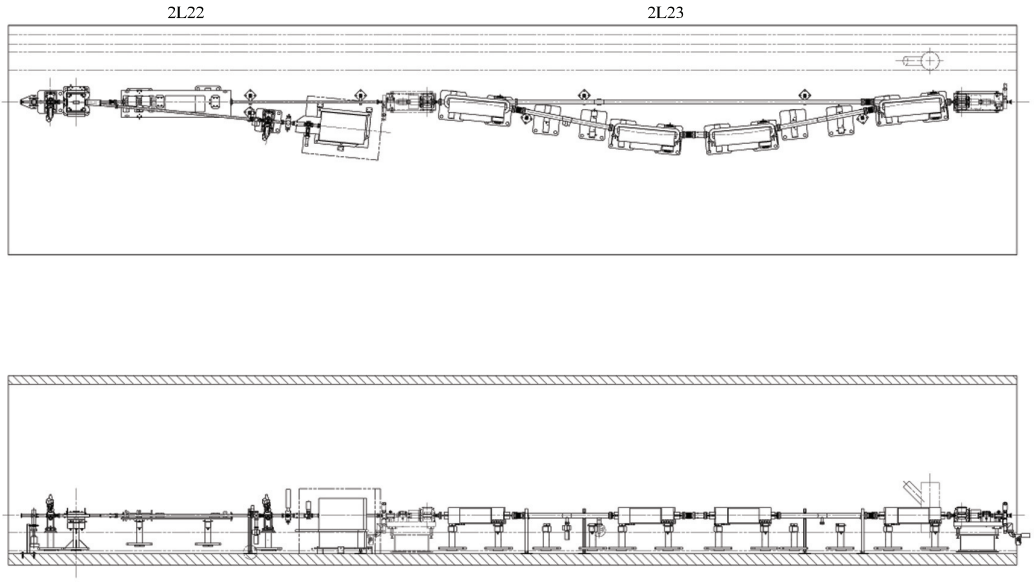

FIG. 2.3: Additional hardware installed to energy recover the beam in CEBAF. The phase delay chicane is installed in an empty cryomodule slot denoted as 2L23 and the beam dump is installed in empty cryomodule slot 2L22. An overhead view of the region is given in the upper drawing and a ground level view is on the bottom.

required to energy recover the beam in CEBAF, a phase delay chicane and a beam dump and beamline outfitted with appropriate diagnostics. These components were installed in regions of the south linac denoted as 2L22 and 2L23 and are shown in Fig. 2.3. The new hardware did not interfere with CEBAF's primary function of providing beam to the nuclear physics community. The energy recovery experiment was noninvasive in the sense that with the dipole string of the phase delay chicane deactivated, it remains transparent to standard CEBAF operations.

The CEBAF-ER experiment operated with a one-pass up, one-pass down scheme. The electron beam was injected into the north linac at 56 MeV where it was accelerated to 556 MeV. The beam traversed arc 1 and then began acceleration through the south linac where it reached a maximum energy of 1056 MeV. Following the south linac, the beam passed through the newly installed phase delay chicane and through arc 2. The chicane generated a path length differential of 1/2-RF wavelength so that

upon re-entry into the north linac, the beam was 180° out of phase with respect to the accelerating RF waveform and was decelerated to 556 MeV. After traversing arc 1 a second time the beam entered the south linac - still out of phase with the RF accelerating field - and was decelerated to 56 MeV at which point the energy recovered beam was deflected to a dump. Upon configuring the machine for energy recovery, measurements were performed to characterize the beam phase space at various points in the machine. These will be discussed in detail in Sections 2.4, 2.5 and 2.6. Once satisfactory measurements were obtained using the 56 MeV injection energy, the measurements were repeated for a lower injection energy of 20 MeV to study the parametric dependence on high maximum-to-injection energy ratios.

While the modifications required to transform CEBAF into an ERL-based accelerator are relatively minor, the fact that CEBAF was not originally designed with the intention of performing energy recovery presents challenges. The following sections will discuss some of those issues and challenges.

2.2.1 Phase Delay Chicane and Beam Dump

The purpose of the phase delay chicane is to provide a path length differential such that the beam enters the north linac on the second pass 180° out of phase with respect to the accelerating RF field. The wavelength corresponding to the fundamental frequency of 1497 MHz is given by

$$\lambda_{RF} = \frac{c}{f_{RF}} = 0.2 \text{ m} \tag{2.1}$$

where c is the speed of light in vacuum. For energy recovery a path length differential of $\lambda_{RF}/2 = 10$ cm is required. The phase delay chicane consists of four dipole magnets and is achromatic, which means that the beam transport does not depend on beam momentum. Because the chicane is installed in a non-dispersive region, it

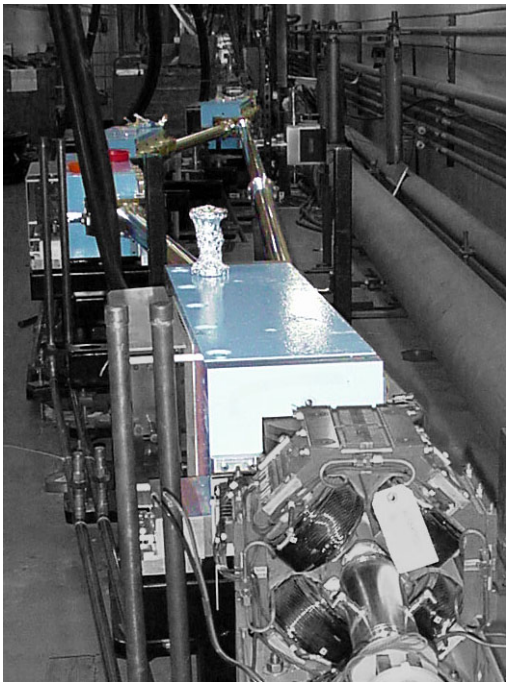

FIG. 2.4: A picture of the energy recovery phase delay chicane to the left of the nominal straight ahead CEBAF beamline. The chicane is comprised of four dipole magnets.

is expected that no remnant dispersion will be generated by the dipoles. Figure 2.4 shows the chicane - installed in region 2L23 - as seen by the beam after exiting the last cryomodule of the south linac.

The beam dump was moved from the injector region, where it was used in conjunction with a spectrometer to measure the injection energy into the linac, to region 2L22. Figure 2.5 shows the dump beamline instrumented with a wire-scanner, beam current monitor (BCM), beam position monitor (BPM) and optical transition radiation (OTR) monitor. The wire-scanner was used to measure beam profiles, the BPM provided information about the position of the beam, the BCM registered the beam current getting to the dump and the OTR monitor allowed confirmation that the beam was reaching the dump face through visual inspection.

In addition to the beam dump, region 2L22 also contains a second, smaller chicane. The purpose of the chicane is to correct the high energy beam orbit which

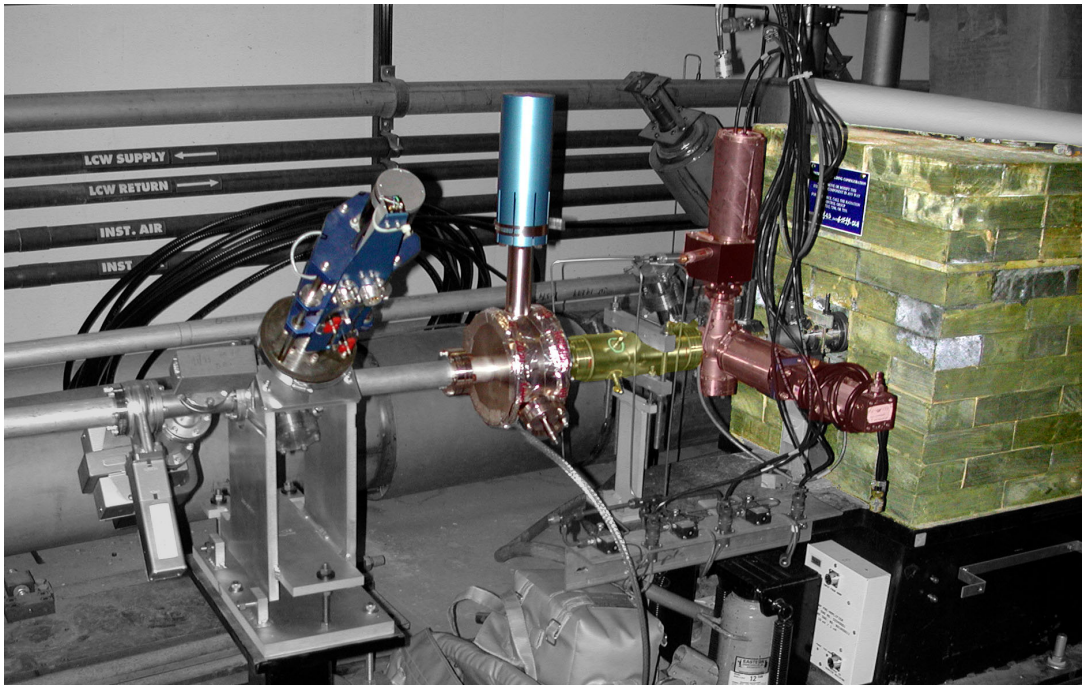

FIG. 2.5: The dump and instrumented beamline during installation. From left to right, the components are a wire-scanner, beam current monitor, beam position monitor (highlighted in yellow), optical transition radiation monitor (highlighted in red) and the beam dump.

is perturbed by the upstream dipole magnet used to deflect the decelerating beam to the dump.

2.2.2 Machine Optics

One of the primary challenges for achieving energy recovery in CEBAF was maintaining adequate control of two co-propagating beams with up to a factor of 51 difference in energy through the same transport channel.

Each linac segment in CEBAF consists of 12 1/2 FODO cells with two embedded cryomodules per cell in each of the first 10 cells [30]. The empty cryomodule slots in the remaining 2 1/2 cells allow for energy upgrades. The half-cell length is 9.6 m while the length of the cryomodule is 8.25 m. The remaining 1.35 m is a warm beamline section connecting adjacent cryomodules which contains quadrupoles, steering

dipoles and beam diagnostics such as OTR viewers and BPMs.

The linac optics were configured such that the lowest energy beam in each linac (the accelerating pass in the north linac and decelerating pass in the south linac) maintain the 120° betatron phase advance per cell that is used for the first pass in standard CEBAF operation. As a consequence, the higher energy beams through each linac will be mismatched. Because only one beam is present in arc 2, the quadrupoles in the spreader and recombiner region are free knobs that can be used to compensate mismatches introduced by optimizing the linac optics for the lower energy beam. In addition to the spreader and recombiner, quadrupoles in the south linac which are downstream of the beam dump can also be used to match the beam. The optics for arc 1, which transports both the first and second pass beams, uses standard CEBAF optics and does not require modification since both beams are assumed to be of the same energy. A description of how this energy balance was achieved is given in Section 2.2.4.

The beta functions for each pass through the north and south linacs after optimization are displayed in Fig. 2.6 and Fig. 2.7.

2.2.3 SRF Induced Effects

One of the primary concerns in preparing for CEBAF-ER was the anticipated harmful RF cavity induced effects on the beam. Whereas the CEBAF Front End Test demonstrated energy recovery through 2 cryomodules (sixteen CEBAF 5-cell SRF cavities), the CEBAF-ER experiment required energy recovering a beam through 39 cryomodules. Consequently, any adverse effects induced by the RF system on the beam become more pronounced.

It is known that the waveguide higher-order mode coupler on each cavity introduces a phase-dependent skew quadrupole component which couples the horizontal

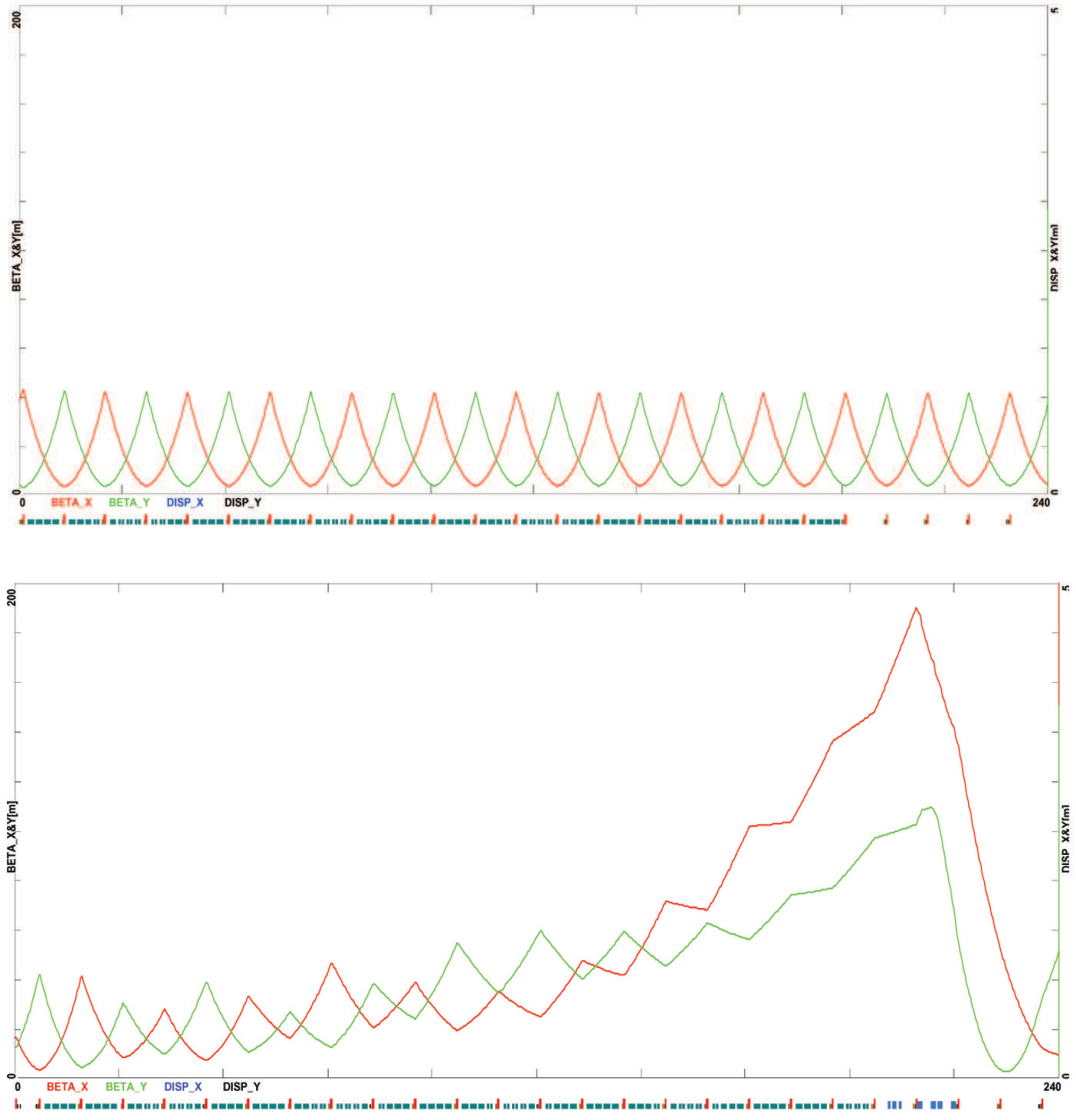

FIG. 2.6: Horizontal (red) and vertical (green) beta functions for the accelerating pass through north linac (top) and the accelerating pass through the south linac (bottom).

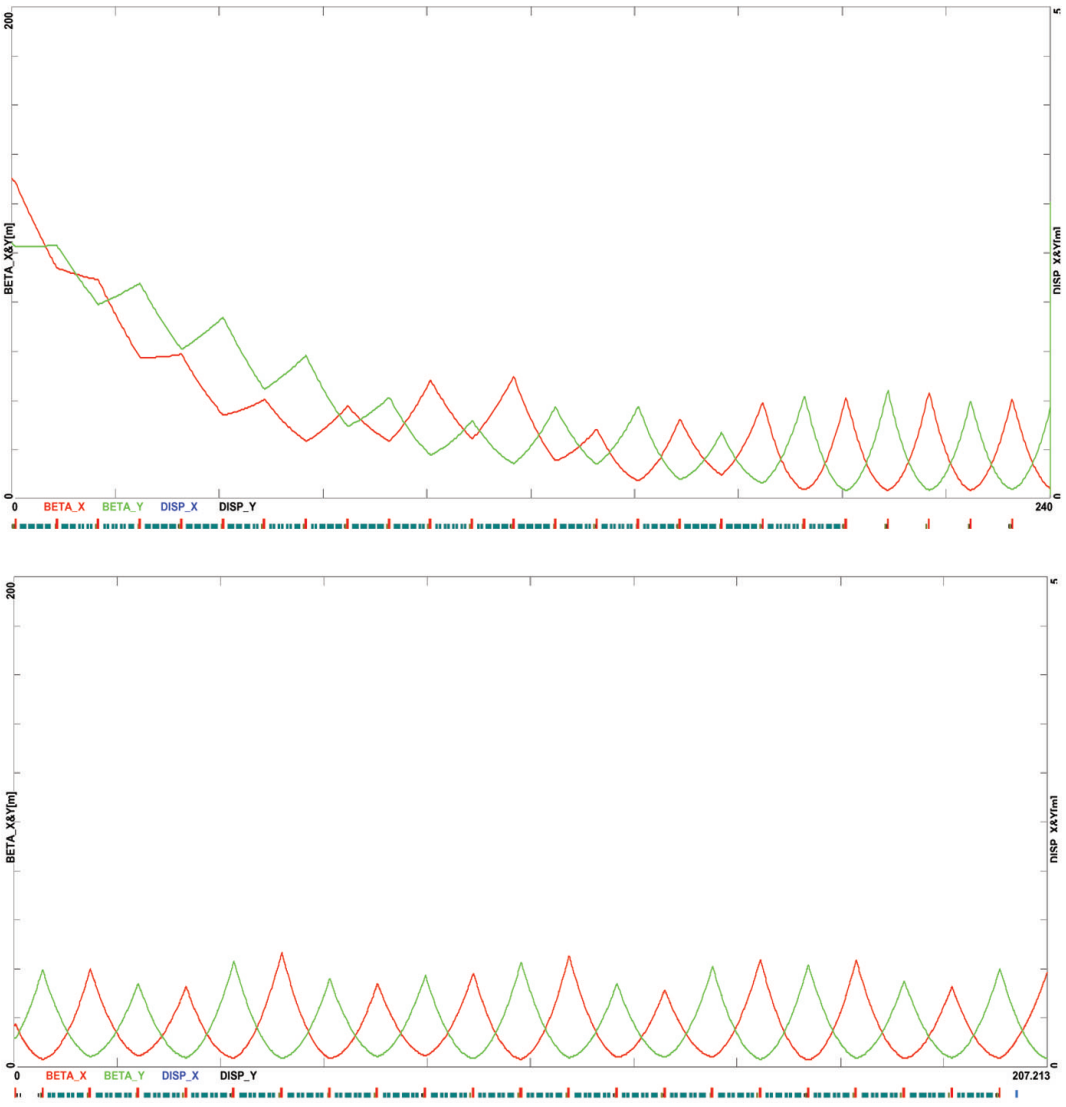

FIG. 2.7: Horizontal (red) and vertical (green) beta functions for the decelerating pass through north linac (top) and the decelerating pass through the south linac (bottom).

and vertical betatron oscillations [31]. In standard CEBAF operation this effect is mitigated by the use of a magnetic skew quadrupole field between cryomodules to produce a compensating gradient integral. However, in CEBAF-ER operation, the sign of the induced skew quadrupole changes since the second pass beam is 180° out of phase with the first pass. Therefore, although the external skew quadrupoles can locally correct the coupling for a single pass through the linac, the effect of the coupling will double on the other pass. This effect makes it difficult operationally to propagate the beam through the machine.

To alleviate the consequences of the coupling, a so-called "up-down" correction scheme was implemented in which the lower energy beams in each linac were corrected using skew quadrupoles. Although the coupling is not fully suppressed with this configuration, it was the most attractive solution based on simulations showing that the initial projected emittances would be recovered after energy recovery [32].

In addition to the fields in the HOM coupler, a transverse electric field gradient exists in the 5-cell cavity's fundamental power coupler. This field gradient not only can transversely deflect the bunch centroid but can also differentially steer the head and tail of a bunch [33]. While the effects of centroid steering can be minimized using correctors, the differential steering of the electron bunch can lead to emittance growth and presents a more difficult problem. Similar to the HOM coupler skew quadrupole coupling, the dipole steering is a phase dependent effect. Unlike the coupling, the effect of the dipole steering depends strongly on the RF feed geometry. That is, the strength of the steering depends on whether the FPC is located at the downstream or upstream end of the cavity and whether the RF power is fed in from the left or right side (as seen by the beam). Therefore the magnitude of the effect can be minimized with an appropriate choice of RF feed geometry.

Because cavities are joined in pairs and the FPCs placed at the center of each cavity pair, alternating the feed direction for each cavity is not feasible technically.

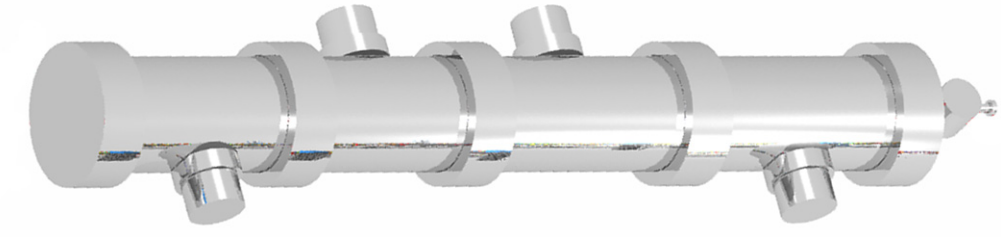

FIG. 2.8: Illustration of the cryomodule RF feed geometry used to minimize the FPC induced dipole kick.

The RF feed geometry that minimizes the emittance dilution due to head-tail steering, while remaining technically viable, is illustrated in Fig. 2.8 [33]. Within each cavity pair, the downstream FPC is followed by a cavity with an upstream FPC. The RF power to the two outer cavity pairs is fed from the same direction, while the two middle cavity pairs are fed in the opposite direction.

Note that these SRF-induced effects are due to particular features of the CEBAF 5-cell cavity design and do not represent fundamental limitations of the energy recovery process. In principle, a well designed SRF cavity can avoid these problems altogether.

2.2.4 Balancing Linac Energy

An important step in configuring CEBAF for energy recovery was balancing the north and south linac energy gains to within the machine acceptance. This is to ensure that arc 1 can cleanly transport the two co-propagating, yet equal energy, beams. Operationally, the linac energies were balanced using a deceleration experiment, wherein beam was accelerated through the north linac, decelerated through the south linac and sent to the energy recovery beam dump [34]. Decelerating the beam through the south linac was accomplished by changing the RF ganged phases by 180°. The linac energies are balanced when the injected energy is equal to the

decelerated beam energy. A spectrometer in the injector region was used to measure the injected energy and the magnet which deflects the beam to the dump was used to measure the decelerated beam energy.

2.3 Transporting Beam to the Energy Recovery Dump

The CEBAF-ER experiment started in earnest on March 25, 2003 using a 56 MeV injector setup and by the following day energy recovered beam was successfully transported to the beam dump. That in itself satisfied the primary goal of the experiment - to demonstrate the feasibility of energy recovery on a large-scale machine and at high energy.

The experiment started by balancing the linac energy as described in Section 2.2.4. After the linac energies were balanced, the RF ganged phases in the south linac were returned to their nominal settings to accelerate the first pass beam. The arc 2 optics, with the spreader and recombiner set to match the beam into the north linac for deceleration, were then loaded into the machine.

2.3.1 Setting the Path Length

To achieve good performance with energy recovery, the decelerated pass must be exactly 180° out of phase with respect to the accelerating pass. Operationally, the proper path length differential was achieved in the following way [35]: first, note that the energy of the first pass beam through arc 1 is

$$E_{A1}^{(1)} = E_{inj} + E_{NL}\cos\theta_{NL} \tag{2.2}$$

where E_{inj} is the injected beam energy, E_{NL} is the energy gain through the north

linac and θ_{NL} is the RF phase. The energy of the beam in arc 2 is

$$E_{A2} = E_{inj} + E_{NL}\cos\theta_{NL} + E_{SL}\cos\theta_{SL} \tag{2.3}$$

where E_{SL} and θ_{SL} are the energy gain and RF phase in the south linac, respectively. The energy of the second pass beam through arc 1 is

$$E_{A1}^{(2)} = E_{inj} + E_{NL}\cos\theta_{NL} + E_{SL}\cos\theta_{SL} + E_{NL}\cos(\theta_{NL} + \delta) \tag{2.4}$$

where δ is the change in RF phase due to the effect of passing through the phase delay chicane. For perfect energy recovery, the energy gained on the first pass exactly cancels the energy lost by the second pass beam through the north linac. The energy in arc 1 is then

$$E_{A1}^{(2)} = E_{inj} + E_{SL}\cos\theta_{SL} \tag{2.5}$$

Equation (2.5) says that for perfect energy recovery, $\delta = \pi$, the energy of the second pass beam in arc 1 is independent of θ_{NL}. Through an iterative process of adjusting the field strength of the phase delay chicane dipole string (to vary the path length) and then varying the RF phase in the north linac, the condition of Eq. (2.5) could be satisfied.

The strategy for threading the beam through the machine was to use minimal steering on the first pass. In that way local corrections could be used to alleviate any harmful RF effects incurred on the second pass. At low energy, and particularly on the second pass, transverse coupling was present. The source of this coupling is the presence of the skew quadrupole fields in the waveguide HOM coupler. This coupling was observed, for example, by inserting a beam viewer and watching the beam spot move diagonally across the screen when steering with a horizontal (or

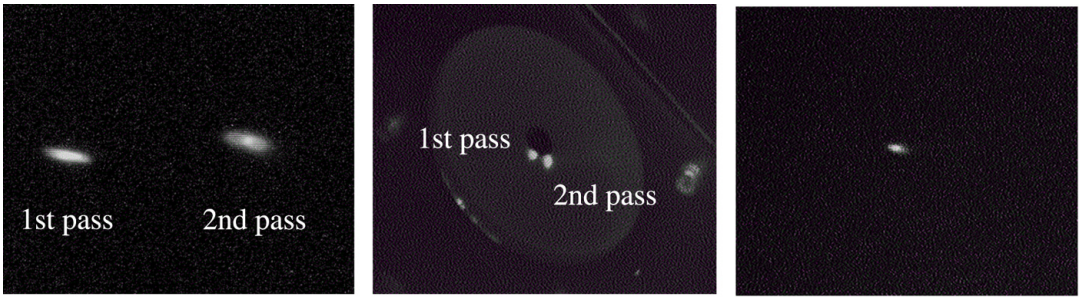

FIG. 2.9: Images of the beam at various locations in the machine. Two co-propagating beams in arc 1 (left), the south linac (middle) and the energy recovered beam image at the dump (right).

vertical) corrector. While this effect presented operational challenges, it did not limit machine performance.

The difficulties in steering the beam were compounded by the lack of functional beam diagnostics in the energy recovery regime [36]. The beam viewers in the linacs have holes to pass the primary beam so later passes can be seen as shown in Fig. 2.9. Viewers in the arcs, however, were never intended to see multiple beams and have no holes. They are only useful for looking at first pass beam. Furthermore, standard arc BPMs were incapacitated during energy recovery due to the destructive interference of the two out-of-phase beams. The only real-time, cw diagnostics capable of measuring the energy recovered beam were the synchrotron light monitor (SLM) at the midpoint of arc 1A and the dump beamline diagnostics. These problems arose simply because the diagnostics for CEBAF were designed for a different set of requirements, namely operating in a non-energy recovery regime.

Despite the operational difficulties, the beam was energy recovered and steered to the dump. The following days were dedicated to making a number of measurements which will be described in the following sections. After measurements were completed using the 56 MeV injection energy, the injector was set to provide beam at 20 MeV and the measurements were repeated.

2.4 Transverse Emittance

One of the most important measurements is the transverse beam emittance. The emittance is a figure of merit that can be used to characterize the extent to which beam quality is preserved. To observe the effects of energy recovery on the beam quality, the emittance of the beam in the injector, in arcs 1 and 2 and of the energy recovered beam were measured.

Each particle in the machine is defined by a point in six dimensional phase space with coordinates $(x, p_x, y, p_y, \ell, \delta)$ where x (y) is the horizontal (vertical) displacement from the central trajectory, p_x (p_y) is the deviation of horizontal (vertical) momentum, ℓ is the path length differential from the synchronous particle and δ is the deviation of the longitudinal momentum from the design orbit. To study the collective motion of a bunch, the ensemble of electrons is projected onto two-dimensional phase sub-spaces. That is, the horizontal, vertical and longitudinal phase spaces are the projections of the beam onto the (x, p_x), (y, p_y), and (ℓ, δ) coordinate systems, respectively. The emittance is defined as the area of the ellipse enclosing the beam in the phase space divided by π. There are two transverse emittances, horizontal and vertical, and one longitudinal emittance. Whereas the transverse emittances are commonly used as figures of merit, the bunch length and energy spread are often used in lieu of the longitudinal emittance.

For an ensemble of non-interacting particles, Liouville's Theorem states that under the influence of conservative forces the density of particles in the phase space remains constant [37]. In the (x, p_x) and (y, p_y) phase sub-spaces, the area of the beam ellipse is defined as the normalized emittance, ϵ_N. An alternate definition is the geometric emittance, ϵ_g, which is the area of the beam ellipse in the (x, x') and (y, y') coordinate systems. Here $x' = dx/dz$ $(y' = dy/dz)$ and is the angle the trajectory makes in the horizontal (vertical) plane. The normalized and geometric

emittances are related simply by

$$\epsilon_N = \beta\gamma\epsilon_g \tag{2.6}$$

where $\beta = v/c$ and $\gamma = 1/\sqrt{1-\beta^2}$ is the Lorentz factor. In an ideal machine the normalized emittance would remain constant from the source through the entire transport. In reality non-linear magnetic fields and wakefields, among other things, act to degrade the emittance.

Emittance measurements were made for three different beam regimes; the beam in the injector, the first pass accelerating beam in each of the arcs and the beam after energy recovery. Measuring the emittance of the energy recovered beam proved to be most challenging as it had to be performed in the presence of the accelerating beam. The following section describes the details of this measurement.

2.4.1 Emittance Measurement Using a Quadrupole Scan

One of the most common beam line configurations used to make emittance measurements consists of a quadrupole followed by a drift of length L to a beam profile monitor. The premise of the quadrupole scan emittance measurement is to determine the horizontal (or vertical) beam size with the profile monitor as function of the strength of the upstream quadrupole. Performing the measurement for three different quadrupole strengths is sufficient to calculate the horizontal (or vertical) emittance.

Denote the betatron functions just prior to entrance of the quadrupole as β_1 and α_1 and those at the downstream observation point by β_2 and α_2. For a non-dispersive region the beam size squared is

$$\sigma_2^2 = \beta_2\epsilon_g \tag{2.7}$$

where σ_2 is the rms beam size measured by a beam profile monitor and ϵ_g is the rms geometrical emittance. By knowing how the Twiss parameters propagate, β_2 can be related to the beta function upstream, β_1, via

$$\begin{pmatrix} \beta_2 \\ \alpha_2 \\ \gamma_2 \end{pmatrix} = \begin{pmatrix} M_{11}^2 & -2M_{11}M_{12} & M_{12}^2 \\ -M_{11}M_{21} & M_{12}M_{21} + M_{11}M_{22} & -M_{12}M_{22} \\ M_{21}^2 & -2M_{21}M_{22} & M_{22}^2 \end{pmatrix} \begin{pmatrix} \beta_1 \\ \alpha_1 \\ \gamma_1 \end{pmatrix} \tag{2.8}$$

where the M_{ij} are the elements of the transfer matrix that propagates beam from the quadrupole to the wire scanner. Using the result of Eq. (2.8) in Eq. (2.7) gives

$$\sigma_2^2 = \beta_2 \epsilon_g = \epsilon_g \left[M_{11}^2 \beta_1 - 2M_{11}M_{12}\alpha_1 + M_{12}^2 \gamma_1 \right] \tag{2.9}$$

For the specific case of a quadrupole-drift, the M_{ij} elements are found by multiplying the transfer matrices for a quadrupole (in the thin lens approximation) and a drift of length L

$$\begin{pmatrix} 1 & L \\ 0 & 1 \end{pmatrix} \begin{pmatrix} 1 & 0 \\ \frac{1}{f} & 1 \end{pmatrix} = \begin{pmatrix} 1 + \frac{L}{f} & L \\ \frac{1}{f} & 1 \end{pmatrix} \tag{2.10}$$

Plugging the appropriate matrix elements from Eq. (2.10) into Eq. (2.9), the relationship between the beam size and the beta function prior to the quadrupole entrance can be expressed as

$$\sigma_2^2 = \beta_2 \epsilon_g = \epsilon_g \left[\left(1 + \frac{L}{f} \right)^2 \beta_1 - 2L \left(1 + \frac{L}{f} \right) \alpha_1 + L^2 \gamma_1 \right] \tag{2.11}$$

Inspection of Eq. (2.11) shows that the beam size squared varies quadratically with the quadrupole strength, k $(= \frac{1}{f})$. Measuring the beam size for three values of the quadrupole strength results in three equations which is sufficient to solve for the three unknowns; $(\beta_1 \epsilon_g)$, $(\alpha_1 \epsilon_g)$ and $(\gamma_1 \epsilon_g)$. This process is known as a quadrupole

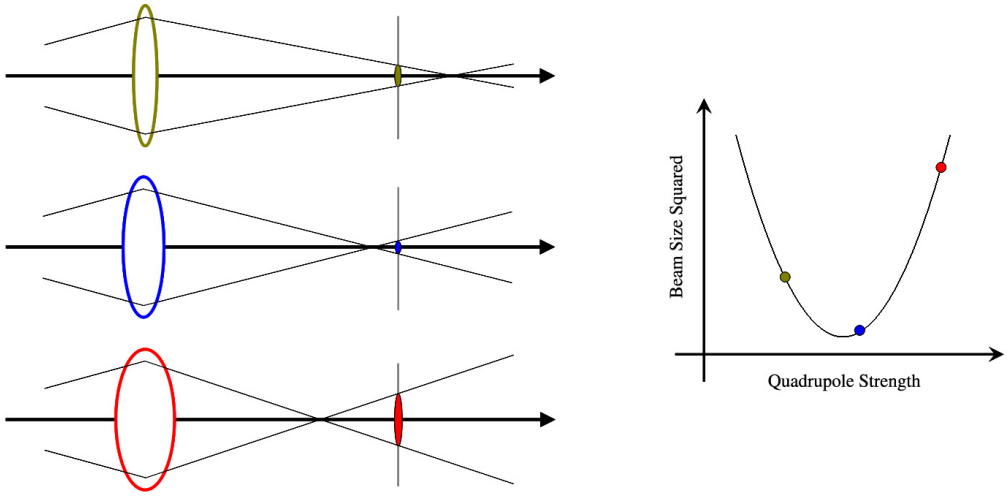

FIG. 2.10: Illustration of quadrupole scan method to measure the transverse emittance. The strength of a quadrupole is varied while the downstream beam size is measured. From Eq. (2.11) and Eq. (2.13) the emittance can be extracted by fitting data with a quadratic fit.

scan and is illustrated in Fig. 2.10. In practice, the quadrupole is scanned over many values of the strength. By fitting the data with a least-squares quadratic fit the unknown quantities are extracted.

Because the transfer matrix has a unit determinant, the following relation holds [38]

$$\beta\gamma - \alpha^2 \equiv 1 \tag{2.12}$$

where $\gamma \equiv (1+\alpha^2)/\beta$. Using the three fitting parameters from the quadratic fit, $(\beta_1\epsilon_g)$, $(\gamma_1\epsilon_g)$, $(\alpha_1\epsilon_g)$, and using Eq. (2.12), the emittance can be calculated

$$\epsilon_g^2 = (\beta_1\epsilon_g)(\gamma_1\epsilon_g) - (\alpha_1\epsilon_g)^2 \tag{2.13}$$

The technique described above is straightforward for a linac, however for a recirculating linac like CEBAF, the situation becomes more complicated. The difficulty arises because the quadrupole used for the scan is common to two co-propagating

beams. The effects of varying the quadrupole strength on the energy recovered beam, in terms of machine performance, is minimal because the beam is immediately deflected to the dump. The accelerated beam, however, also feels the effects of the quadrupole change which creates a mismatch between the beam and the design machine optics. The consequences of this mismatch is twofold. First, since the emittance measurement assumes that the beta functions prior to the scanning quadrupole remain constant, if left uncorrected, the mismatched beam will recirculate through the machine and arrive at the quadrupole with different beta functions. Second, for large excursions of the quadrupole strength the mismatch can become severe, leading to excessive beam loss and thereby causing the machine to trip off. The solution for both problems is to produce compensatory optics downstream of the scanning quadrupole to re-match the beam to the rest of the machine.

Note that placing a quadrupole in the dump beamline would avoid this complication altogether. In this case the quadrupole could be scanned without the need to produce compensating optics. Unfortunately due to constraints in time and in the available space on the dump beamline, this option was not feasible.

2.4.2 Measuring Beam Sizes

The beam profile monitor used for the measurement is an intercepting device known as a wire scanner, although other beam profile monitoring devices such as fluorescent screens and OTR monitors could also be used. Wire scanners are routinely used throughout the CEBAF accelerator to measure the beam profile by recording the charge and position of a thin wire as it passes through the beam [39]. The wire scanner consists of an assembly that rigidly holds three 25 μm tungsten wires oriented along the x, x-y and y axes. An illustration of a 3-wire scanner is shown in Fig. 2.11.

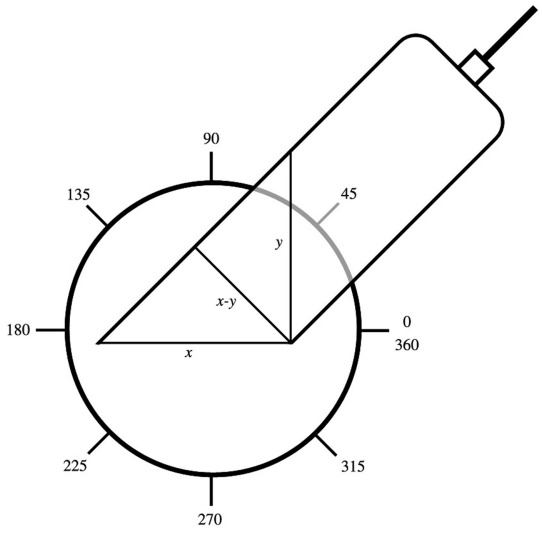

FIG. 2.11: A 3-wire scanner oriented at 45° with respect to the horizontal plane.

In order to get sufficient resolution of the beam sizes, the horizontally focusing quadrupole at 2L21 was scanned to extract the horizontal emittance and the vertically focusing quadrupole at 2L22 was scanned to extract the vertical emittance. A 3-wire scanner - installed approximately 30 cm upstream of the dipole magnet used to deflect the energy recovered beam to the dump - was used to measure beam sizes. An actuator drives the wire scanner which is mounted at an angle of 45° with respect to the horizontal axis. Using a 3-wire scanner (to measure x, x-y, y profiles) each scan yielded six distinct peaks (3 wires $\times$ 2 beams). Initially, there was some concern as to how to differentiate each peak and assign them to the appropriate beam. However it soon became clear that the energy recovered beam (56 MeV or 20 MeV, depending on the injector setup) did not produce nearly as high, sharp peaks as the accelerated beam (1056 MeV or 1020 MeV). This fact was easily confirmed by using dipole correctors to locally steer the beam and identifying the displaced peaks with the lower energy beam. A typical scan is shown in Fig. 2.12. Because the capability to automatically extract beam sigmas from the wire scans did not exist at the

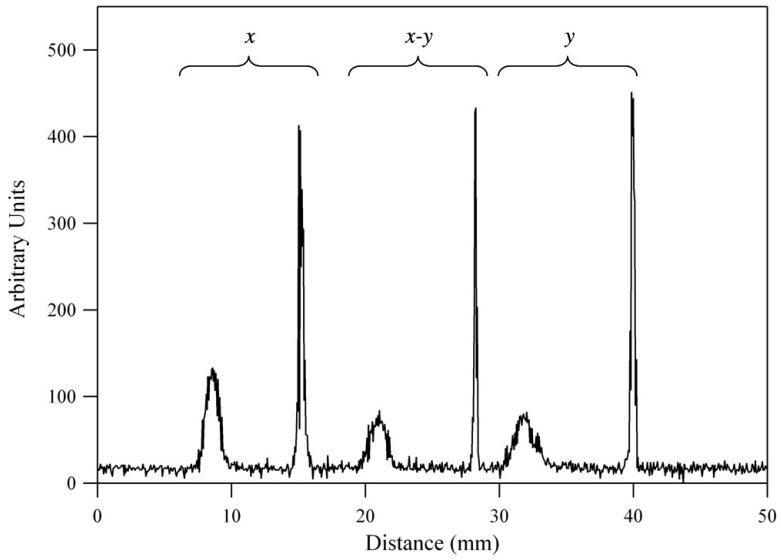

FIG. 2.12: A typical wire scan near the extraction region showing six distinct peaks as a result from a 3-wire scanner passing through two co-propagating beams.

time of the experiment, analysis was performed off-line. This resulted in unforeseen difficulties which will be discussed in Section 2.4.3.

The data analysis program Igor Pro [40] was used to analyze the raw wire scans. The program has the feature that only regions selected by the user are used for curve-fitting. This is convenient for the wire scans since there are multiple peaks and also because there is the possibility of peaks which are partially merged. The program applies a Gaussian fit to the data of the form

$$y(x) = \frac{A}{\sqrt{2\pi}\sigma} e^{-\left(\frac{x-B}{\sqrt{2}\sigma}\right)^2} \tag{2.14}$$

To account for the effect of the 45° angle of the wire scanner on the x and y profiles (the x-y profile requires no correction) the extracted sigmas are divided by a factor of $\sqrt{2}$.

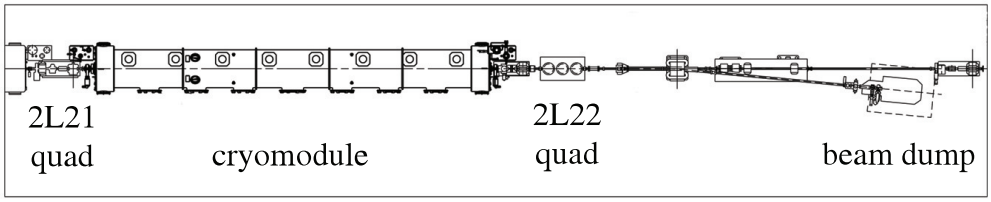

FIG. 2.13: A schematic of the 2L21 and 2L22 regions of CEBAF and the location of the quadrupoles used to measure the emittance.

2.4.3 Data Analysis

Scanning the quadrupole at 2L22 to measure the vertical emittance constitutes a simple quadrupole-drift scheme. Based on simulated emittance measurements using design optics, measuring the horizontal emittance using the 2L22 quadrupole would require huge changes in field strength which create very large beta functions downstream. To remedy the problem, the quadrupole at 2L21 was used to measure the horizontal emittance. During the experiment a new cryomodule installed in the slot between the 2L21 and 2L22 quadrupoles was being commissioned. During emittance measurements the cavities in the cryomodule were set to zero accelerating gradient thereby effectively making the cryomodule a drift space. Consequently, the horizontal emittance is based on a quadrupole-drift-quadrupole-drift scheme where the 2L22 quadrupole remains at a fixed field and the 2L21 quadrupole strength is varied. Figure 2.13 shows a layout of the region. In terms of the analysis in Section 2.4.1, Eqs. (2.7), (2.8) and (2.9) remain the same and only Eq. (2.10) is modified to reflect the new beam line configuration.

While the preceding analysis has modeled the quadrupoles as thin lenses, the program used to fit the experimental data was modified to model a thick lens quadrupole. The major difference in terms of analysis is that now, not only does the M_{11} transfer matrix element depend on the quadrupole strength, but so too does the M_{12} element. From Eq. (2.9) this rules out being able to perform a simple

quadratic fit and a multiple regression fit is required.

The data for the four emittance measurements - two transverse planes (vertical and horizontal) for each of the two injector energy setups - are presented in Fig. 2.14 and Fig. 2.15. Before discussing the specifics of each measurement, some general comments are in order. Each plot displays the beam size squared versus the magnification, or M_{11} matrix element. The red data points in each plot represent the data on which the multiple-regression fit is being performed, whereas the blue data points represent those points which have been omitted (for reasons discussed below). The error bars on the data points are the errors associated with extracting the beam sizes from the raw wire scans.

Horizontal Emittance: E_{inj}= 56 MeV

The limited number of data points reflects the fact that this was the first attempt at an emittance measurement. As with all future emittance measurements there was some local steering required to ensure that the signal of interest from the wire scan was not overlapping an adjacent peak. Despite the limited data the beta function passed through a minimum, which is critical for getting a good fit with a quadratic function. The leftmost data point - corresponding to a quadrupole strength furthest from the nominal set point - was omitted in the fit. The reason is that a fit on all data points results in an unphysical solution, namely $\epsilon_g^2 < 0$. Omitting the point results in a physically realizable emittance. Judiciously omitting data points which lead to nonsensical emittances was often required in subsequent measurements.

Vertical Emittance: E_{inj} = 56 MeV

Despite the large number of data points, because the quadrupole was not scanned far enough to allow the beta function to pass through a minimum, fit-

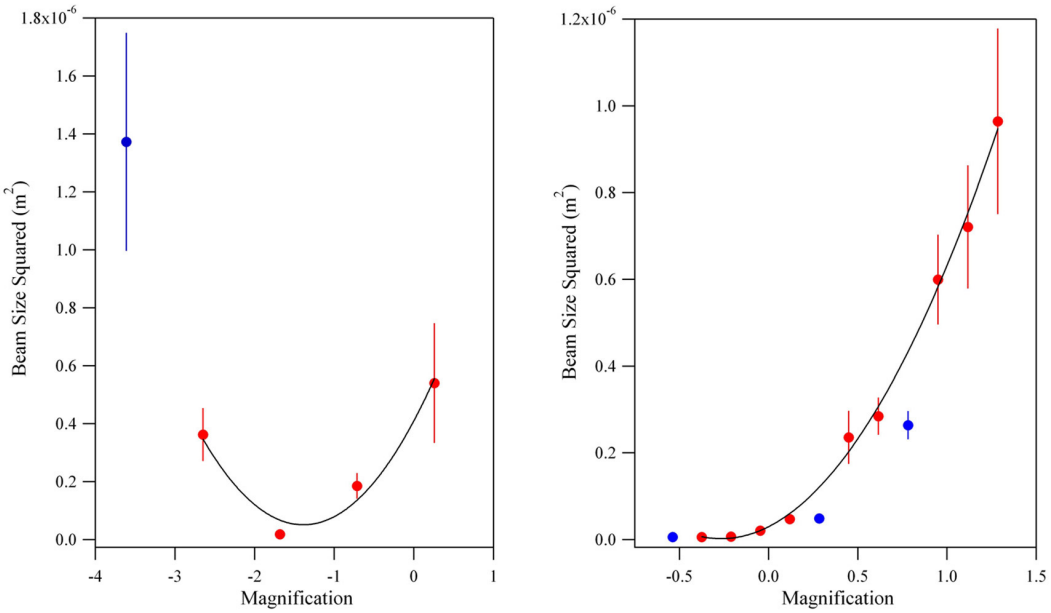

FIG. 2.14: Measured data for extracting the horizontal (left) and vertical (right) emittance at an energy of 56 MeV. Blue markers denote data points that were not used in the multiple regression fit.

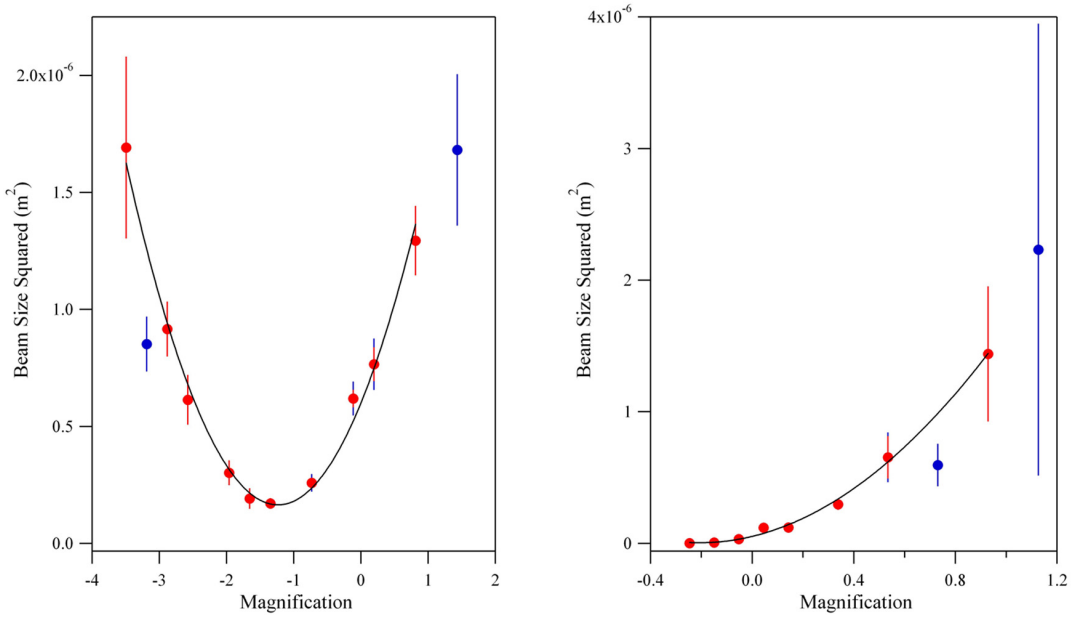

FIG. 2.15: Measured data for extracting the horizontal (left) and vertical (right) emittance at an energy of 20 MeV. Blue markers denote data points that were not used in the multiple regression fit.

ting the data is difficult. Without the ability to extract beam sizes in real time, this was only revealed after the fact. As with the previous measurement, fitting the complete data set results in an unphysical emittance. Since a unique beam size is expected for each value of the quadrupole strength, points were omitted that violated this condition. The result is a physically acceptable emittance.

Horizontal Emittance: $E_{inj} = 20$ MeV

This data set represents an ideal measurement - a large number of data points with the beta function sweeping through a minimum. The two points that were omitted were outliers.

Vertical Emittance: $E_{inj} = 20$ MeV

This measurement shows once again that the quadrupole strength was not sufficiently scanned and the fitting must be applied to half of a parabola. The points omitted were done so for obvious reasons; the rightmost point was omitted due to an excessively noisy wire scan (note the large error bar), while the other omitted point is an outlier.

When scanning the quadrupole, not only is the energy recovered beam affected, but perhaps more importantly, so is the accelerated or first pass beam. The importance results from the implicit assumption that the Twiss parameters at the entrance of the scanning quadrupole remain the same. In order to meet that requirement, a family of quadrupoles (downstream of the reinjection chicane) was used to produce compensating optics to counter the effects produced by the scanning quadrupole.

Prior to the CEBAF-ER experiment, the emittance measurements were simulated in Optim [41], including producing appropriate compensatory optics. During the CEBAF-ER experiment however, the machine optics used for the $E_{inj} = 20$ MeV configuration were not those used in the simulations. Hence, compensating op-

tics could not be loaded. Because the quadrupoles were running at strengths $(E_{max}/E_{inj}) = 51$ times smaller than in standard CEBAF operations, scanning the quadrupole by tens of Gauss has a negligible effect on the emittance measurement - despite not producing compensatory optics. An expression for the relative change in the beta functions due to a focusing error is given by [42]

$$\frac{\delta\beta}{\beta_o} = \mp\frac{\beta_i}{f}\sin(2\Delta\psi) \tag{2.15}$$

where β_i is the initial, unperturbed beta function, $\Delta\psi$ is the phase advance for a single revolution in the machine starting from the location of β_i, f is the focal length of the focusing error and the upper (lower) sign applies to the horizontal (vertical) plane. To first order the betatron phase advances can be determined from the model optics and are 60° and 145° for the vertical and horizontal planes, respectively. Assuming a focusing error of 150 G (the extent to which each quadrupole was scanned) gives

$$\frac{\delta\beta}{\beta_o} = -\beta_i\left(\frac{150}{33.365\cdot 1020}\right)\sin(2\cdot 145^\circ) \simeq \beta_i(0.004) \tag{2.16}$$

$$\frac{\delta\beta}{\beta_o} = \beta_i\left(\frac{150}{33.365\cdot 1020}\right)\sin(2\cdot 60^\circ) \simeq \beta_i(0.004) \tag{2.17}$$

where Eq. (2.16) corresponds to the horizontal plane and Eq. (2.17) corresponds to the vertical plane. For the first pass beam with an initial unperturbed beta function of 100 m, the result of the focusing perturbation caused by not producing compensating optics leads to a contribution of 40 cm to the beta function on the second pass. Because the beta functions are on the order of 35 m, the contribution is approximately 1% and can safely be ignored.

Other sources of error include errors in the magnet-to-harp distance, magnet power supplies, quadrupole excitation calibration, and beam energy. However, the

primary source of error is measuring the beam spot diameters with the other sources of error being negligible in comparison [43].

2.4.4 Emittance Measurement Using Multiple Monitors

In addition to the quadrupole scan technique, the emittance can also be measured using multiple wire scanners in conjunction with multiple beam optics. The latter method is used in standard CEBAF operations to measure transverse emittances in the injector and in the arcs.

In the injector region, a single quadrupole is scanned three times while five downstream wire scanners record the transverse beam sizes. A chicane used to merge the injected beam into the main linac provides a region of dispersion where the energy spread can be measured in addition to the emittance.

For the emittance measurement in the arcs, an insertable dump was used to intercept the beam prior to re-entry into the north linac. In this way only the accelerating pass is transported in arc 1 and the emittance is readily measured using standard CEBAF procedures. The measurement uses two wire scanners in each arc. One wire scanner is located in a region of zero dispersion and used to extract the emittance, while the second is located downstream in a region of high dispersion and used to measure the energy spread. The method requires varying the quadrupoles between a location upstream of the wire scanners where the emittance will be measured (referred to as the fit point) and the first wire scanner. To ensure a good measurement, two primary criteria must be satisfied; first, the emittance measurement must be done in a region of zero dispersion and second, the matrix that defines the transport between the location of the fit point to the wire scanners must be well known. A scheme to measure the emittance and energy spread of the second pass beam proved to be too difficult. Hence the only quantitative measurement of

TABLE 2.1: Normalized transverse emittances measured with the injector set to 56 MeV.

Location	ϵ_x (mm-mrad)	ϵ_y (mm-mrad)	Energy (MeV)
Injector	0.120 ± 0.001	0.189 ± 0.005	56
Arc 1	0.434 ± 0.106	0.257 ± 0.008	556
Arc 2	2.393 ± 0.350	2.065 ± 0.037	1056
Extraction	0.588 ± 0.233	1.051 ± 0.396	56

TABLE 2.2: Normalized transverse emittances measured with the injector set to 20 MeV.

Location	ϵ_x (mm-mrad)	ϵ_y (mm-mrad)	Energy (MeV)
Injector	0.101 ± 0.004	0.090 ± 0.001	20
Arc 1	0.281 ± 0.013	0.253 ± 0.007	520
Arc 2	0.675 ± 0.284	0.451 ± 0.023	1020
Extraction	0.411 ± 0.039	0.871 ± 0.342	20

the energy recovered beam is of its transverse emittance prior to being sent to the dump.

The results of all the emittance measurements are discussed in the following section.

2.4.5 Results

The normalized transverse emittances measured at various locations in the machine for an injection energy of 56 MeV and 20 MeV are summarized in Table 2.1 and Table 2.2, respectively.

The most striking feature of the measurements is the exceedingly large horizontal and vertical emittance in arc 2 for the 56 MeV injector configuration. While transverse coupling can cause the projected emittances of one plane to increase at the expense of the other, the fact that both transverse planes grew by such a large amount suggests a faulty measurement, rather than a real physical process.

During this particular measurement several tens of centimeters of remnant dispersion were observed in arc 2. The source of the dispersion was never clearly

identified, although the phase delay chicane and/or steering errors may have contributed. The dispersion was never fully suppressed and this may have led to the spurious results in arc 2. Recall that the emittance measurement explicitly assumes zero dispersion. Moreover, measuring the emittance in arc 2 was difficult even with zero dispersion (as was the case for the 20 MeV setup), due to the close proximity of the wire scanner to the 2E02 quadrupole used for generating multiple optics. With the wire scanner only 1 m downstream of the scanning quadrupole, the optics could not be changed sufficiently for a good measurement (analogous to not sweeping through a minimum of the beam size for the single quadrupole scanning method). These two conditions working together may account for the spurious data.

Even when the arc 2 measurement is disregarded, the measurements show that the normalized emittance grows as it is transported through the machine. Possible sources of the emittance growth can be traced back to the SRF induced effects discussed in Section 2.2.3.

Simulations using the present RF feed configuration in CEBAF show that a single pass through the machine could cause the projected horizontal normalized emittance to grow by up to 1 mm-mrad due solely to the effects of the dipole mode driven head-tail steering. Fields also exist which cause growth of the vertical emittance, however the effect is small in comparison.

Simulations were also performed with DIMAD [44] in an effort to understand the role of the HOM coupler induced transverse coupling in the observed emittance growth. The simulation modeled the coupling by introducing a thin skew quadrupole element at the location of each cavity's HOM coupler. Results of the simulation showed the horizontal normalized emittance exhibiting growth of 0.5 mm-mrad but failed to explain the observed behavior of the vertical emittance in Table 2.1 and Table 2.2.

Ultimately, a simulation that incorporates the dipole steering of the FPC and

the coupling of the HOM coupler is required. Such an undertaking is complicated by the fact that only simple analytic models have been used to estimate the magnitude of the steering and coupling effects. For instance, a formula for the magnitude of the dipole steering exists but assumes that each cavity operates with an accelerating gradient of 5 MV/m, which is not the case in reality [33]. Estimates of the magnitude of the coupling due to a single cavity have been made [31], however it neglects the effects of the betatron phase advance which can play an important role for an extended linac like in CEBAF [45].

Extracting Twiss Parameters

In addition to measuring the emittance, the Twiss parameters prior to the scanning quadrupole can be determined. With knowledge of the emittance and of the fitting coefficients ($\beta_1\epsilon_g$), ($\alpha_1\epsilon_g$) and ($\gamma_1\epsilon_g$) the Twiss parameters are easily calculated and can be compared with the model optics. The linear optics code Optim was used to model the CEBAF-ER lattice. The results of the model optics and of the experimental measurements are displayed in Table 2.3. The agreement is very good, on the level of 5%, and further justifies the choice of data points used for fitting. The large errors associated with the extracted betas and alphas are the result of propagating the relatively large errors from the corresponding emittances.

Because a model optics does not exist for the machine configured with 20 MeV injection energy, the extracted Twiss parameters could not be compared to the model.

TABLE 2.3: Comparison of Twiss parameters from optics as modeled by Optim and from measurements for $E_{inj} = 56$ MeV.

Location	Optim	Measured
2L21 Quadrupole	$\beta_x = 32.3$ m $\alpha_x = -2.8$	$\beta_x = (33.5 \pm 9.6)$ m $\alpha_x = (-2.6 \pm 0.1)$
2L22 Quadrupole	$\beta_y = 39.5$ m $\alpha_y = -3.4$	$\beta_y = (37.6 \pm 13.5)$ m $\alpha_y = (-3.5 \pm 0.2)$

2.5 Measuring Beam Profiles of the Energy Recovered Beam

The standard CEBAF wire scanner measures the induced current on the wire due to secondary emission of electrons from the wire. These induced currents tend to be in the nanoampere range and this system is well suited to measuring the core size of the beam and typically has two orders of magnitude dynamic range. To improve the dynamic range of the wire scanner for beam profile measurements of the energy recovered beam, additional instrumentation was added to the wire scanner just upstream of the beam dump. This instrumentation relies on photomultiplier tubes (PMTs) to detect the scattered secondary electrons from the incident beam intercepting the wire. The intensity of the electron spray detected by the PMT is proportional to the charge that the wire intercepts and a beam profile with two to three orders of greater dynamic range can be achieved [46]. The beam currents for the energy recovery experiment are large (tens of μA) compared to those previously measured using this method in CEBAF's Hall-B (nA range) where photomultipliers are routinely used.

To qualitatively characterize beam preservation through the accelerator, the beam profile data were fit with a Gaussian distribution. The choice of the fitting function reflects the fact that a typical wire scan will show a narrow Gaussian distribution representing the core of the beam. Figure 2.16 and Fig. 2.17 display

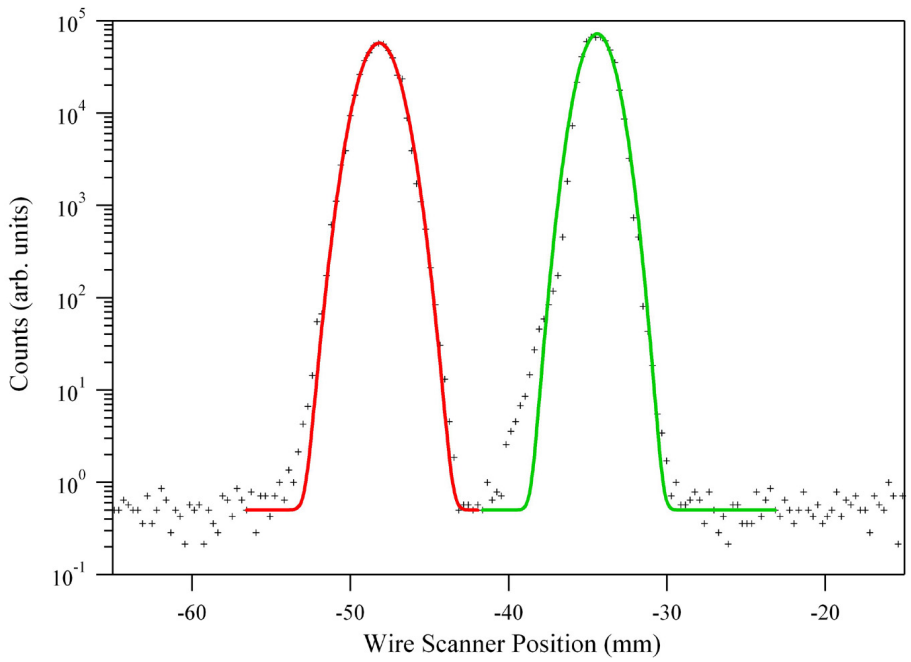

FIG. 2.16: Beam profiles of the 56 MeV energy recovered beam at the dump. The vertical (left) and horizontal (right) are each fit with a single Gaussian.

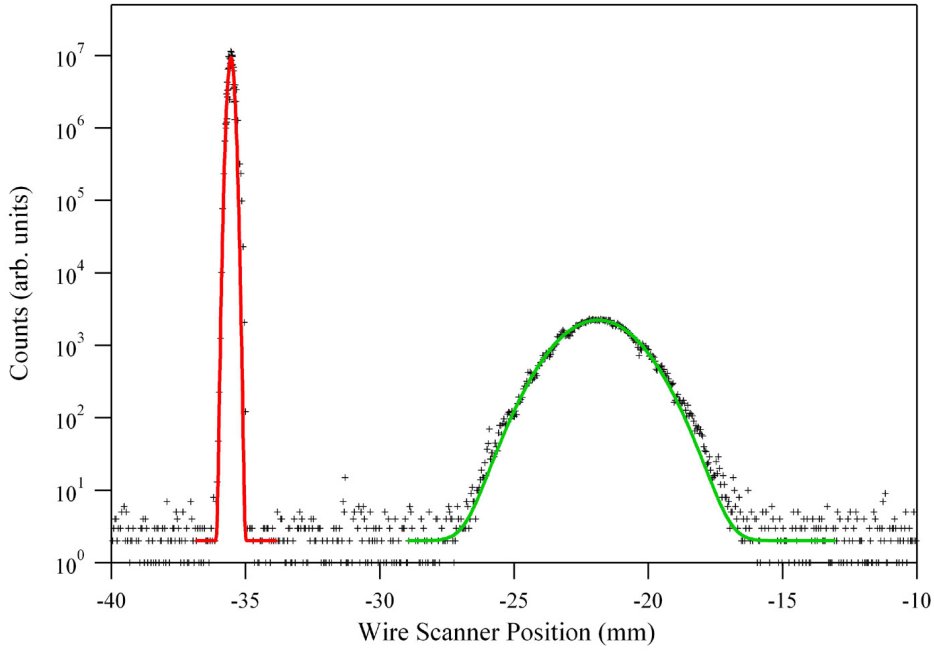

FIG. 2.17: Beam profiles of the 20 MeV energy recovered beam at the dump. The vertical (left) and horizontal (right) are each fit with a single Gaussian.

the results of the fits.

The vertical profile for both the 56 MeV and 20 MeV energy recovered beam are well represented by a single Gaussian over the complete (5 to 6 orders of magnitude) dynamic range. The horizontal profile for the 56 MeV beams shows a small additional contribution on the left side of the plot, most likely due to beam scraping, however there still exists a good Gaussian fit over 5 orders of magnitude. The broader width of the horizontal profile at 20 MeV is explained by the fact that the measurement was located in a region of dispersion (0.5 m) and the width is therefore scaled by a factor of $\Delta E/E$. This may account for the observed increase in horizontal scraping and beam loss when operating with a 20 MeV injection energy.

2.6 Measuring Energy Spread

The rms beam size squared is expressed as

$$\sigma^2 = \beta\epsilon_g + (\eta\delta)^2 \tag{2.18}$$

where η is the dispersion and δ $(= \Delta E/E)$ is the fractional energy spread. Emittance measurements were performed in regions of zero dispersion so that the only contribution to the beam size is from the beta function and the emittance. In the same manner, the energy spread can be measured in a dispersive region where $(\eta\delta)^2 >> \beta\epsilon_g$ and the dispersion is known.

The results of the energy spread measurements, which were performed only on the accelerating pass beam, are displayed in Table 2.4 and Table 2.5.

On first inspection, the energy spread data does not follow the expected scaling relation with energy. Rather than decreasing with increasing beam energy, the measured relative energy spreads in arc 2 are greater than in arc 1. However, by taking into account RF phasing errors the data becomes consistent [47].

TABLE 2.4: Fractional energy spread measured at various locations in the machine with the injector set to 56 MeV.

Location	$\Delta E/E$ (10^{-3})	Energy (MeV)
Injector	0.32 ± 0.01	56
Arc 1	0.0080 ± 0.0023	556
Arc 2	0.020 ± 0.0018	1056

TABLE 2.5: Fractional energy spread measured at various locations in the machine with the injector set to 20 MeV.

Location	$\Delta E/E$ (10^{-3})	Energy (MeV)
Injector	0.15 ± 0.01	20
Arc 1	0.0072 ± 0.0010	520
Arc 2	0.0100 ± 0.0014	1020

For example, with an injection energy of 20 MeV, the intrinsic fractional energy spread is 0.15×10^{-3}. With appropriate scaling, and for a perfectly phased linac, the arc 1 energy spread is expected to be [48]

$$\left(\frac{\Delta E}{E}\right)_{520} = \sqrt{\left[\left(\frac{\Delta E}{E}\right)_{20}\left(\frac{20}{520}\right)\right]^2 + \left(\frac{\delta\phi^4}{2}\right)} \tag{2.19}$$

where $\delta\phi$ is the rms bunch length in radians. Using the measured data, the contribution to the energy spread from the bunch length can be calculated. Plugging in values and solving for the bunch length yields 0.14° (rms). The expected energy spread in arc 2 can be calculated using Eq. (2.19) by modifying the energy scaling factor from (20/520) to (20/1020). The result is 0.0052×10^{-3} and is 74% smaller than the measured value. The effect of RF crest phasing errors can cause increases in the observed fractional energy spread and can account for this discrepancy. The effect is illustrated in Fig. 2.18 and described by

$$\Delta E = E\big[\cos(\phi_o + \delta\phi) - \cos(\phi_o - \delta\phi)\big] \tag{2.20}$$

where ϕ_o is the error in RF phase relative to on-crest acceleration. Equation (2.20)

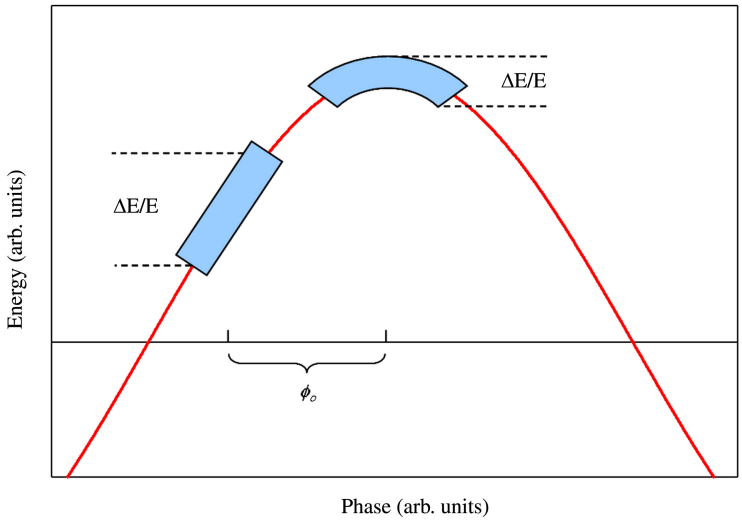

FIG. 2.18: Schematic illustrating the effect of an RF crest phasing error on the fractional energy spread.

can be rewritten more conveniently as

$$\left(\frac{\Delta E}{E}\right)_{phase} = 2 \sin \phi_o \sin \delta\phi \tag{2.21}$$

Assuming a 0.06° RF crest phasing error and adding this contribution to to the expected relative energy spread in arc 2 yields a value of 0.02×10^{-3} which agrees with the measured data.

The 56 MeV case can be analyzed in much the same manner. It turns out, however, that the relative energy spread measured in arc 1 is much less than the expected value (0.033×10^{-3}). Because this expected value is based on a perfectly phased linac, there are no mechanisms which can account for the discrepancy and this may represent a poor data point. The expected energy spread in arc 2 can be calculated with

$$\left(\frac{\Delta E}{E}\right)_{1056} = \sqrt{\left[\left(\frac{\Delta E}{E}\right)_{56}\left(\frac{56}{1056}\right)\right]^2 + \left(\frac{\delta\phi^4}{2}\right)} + \left(\frac{\Delta E}{E}\right)_{phase} \tag{2.22}$$

and using the bunch length derived in the 20 MeV calculation and assuming an RF phase error of 0.03° gives 0.01×10^{-3} which agrees with the measured data.

2.7 Response of the RF System

In addition to characterizing the beam properties, the RF system's response to energy recovery can be measured. A typical measurement is shown in Fig. 2.19 which illustrates the RF system gradient modulator drive signal during pulsed beam operation for cavity 7 in the 2L02 region in the south linac. This signal, locally called the GASK, is part of the low-level RF control system used to maintain the amplitude and phase of the cavity fields. Without energy recovery the signal is nonzero when a 250 μs long beam pulse enters the RF cavity, indicating that power is drawn. With energy recovery, the signal is zero once the initial transient passage of the leading edge of the pulse is over, thereby showing that no additional power draw is required by the cavity.

The macropulse draws power on the first pass through the cavity since the RF system does not see the effects of energy recovery until the beam arrives on the second pass 180° out of phase. The inset of Fig. 2.19 shows that power is drawn for a time of 4.3 μs which corresponds to the recirculation time for one pass through CEBAF.

As an aside, the GASK signals have a practical function at the FEL Upgrade Driver where they are routinely used during operations as a diagnostic to properly energy recover the machine. Changing the path length until the GASK signal is zero ensures the two beams are 180° out of phase.

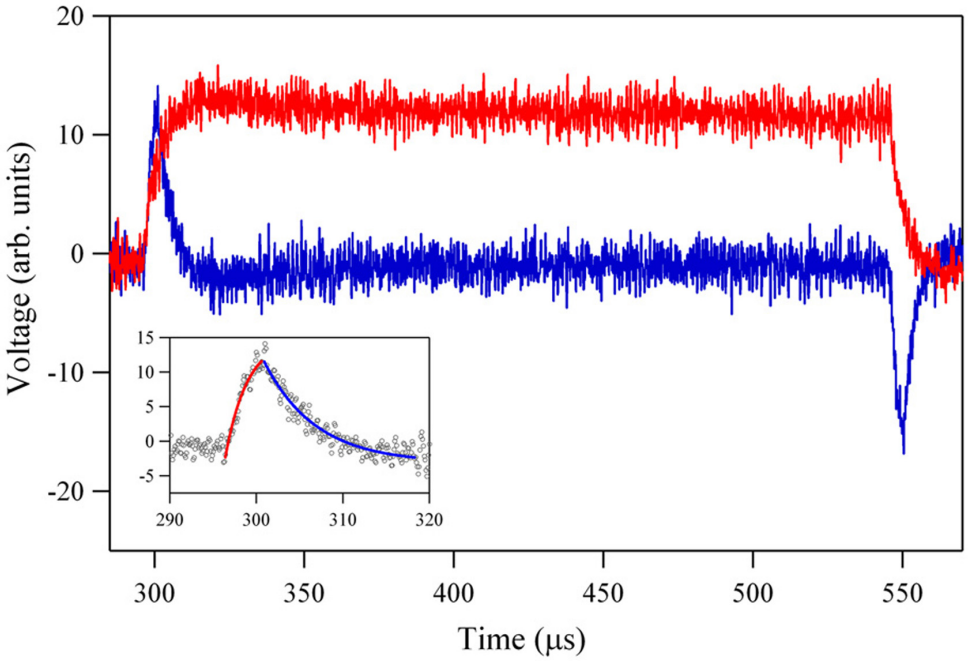

FIG. 2.19: The GASK signal measured with (blue) and without (red) energy recovery. With the initial passage of the leading edge of the pulse, power is drawn for 4.3 μs which corresponds to the recirculation time (inset).

2.8 Conclusions

First and foremost, the CEBAF-ER experiment demonstrated the feasibility of energy recovering a 1 GeV electron beam through a 1.3 km transport system and through an extended superconducting environment of 312 cavities. In doing so, sufficient operational control of two coupled beams of different energies (up to a factor of 51 different) in a common transport channel in the presence of steering and focusing errors was also demonstrated.

One of the important issues that the CEBAF-ER experiment addressed is that the beam quality could be preserved over a large dynamic range of energy. During the experiment, maximum-to-injector energy ratios (E_{max}/E_{inj}) of 19:1 and 51:1 were demonstrated by operating with two different injector energies. For the sake of comparison, note that in the IR FEL Demo this ratio was 5:1 and in the FEL

Upgrade the ratio is approximately 20:1.

With the injector set to provide 56 MeV into the linac, 80 μA of cw beam, accelerated to 1056 MeV and energy recovered at 56 MeV, was steered to the energy recovery dump. Electron source problems, and not issues related to the energy recovery process, limited operation to below the typical 100 μA average beam current. Changing the injection energy to 20 MeV, 1 μA of cw beam was energy recovered, after being accelerated to 1020 MeV. The low average current does not represent a fundamental limit, rather it reflects the lack of time available to optimize the machine for handling the increased beam losses observed at this lower injection energy.

An understanding of how the emittance evolves can be gained by making measurements at several locations in the machine. The results for the two machine configurations, $E_{inj} = 56$ MeV and $E_{inj} = 20$ MeV, are summarized in Fig. 2.20 and Fig. 2.21, respectively. The arc 2 emittance data in Fig. 2.20 has been removed for reasons discussed in Section 2.4.5. Qualitatively, the emittances for each machine configuration evolve in a similar manner. Moreover, it can be concluded that the process of energy recovery does not degrade the transverse emittance, since the emittance growth on the accelerating pass is consistent with the growth on the energy recovery (decelerating) pass.

Quantifying beam loss is vital for the next generation of ERLs which propose to operate with megawatt beam powers and where even small amounts of beam loss can severely damage machine components. While the beam loss in CEBAF-ER was not measured directly, an upper limit of 0.5 μA can be used due to the fact that a stable machine configuration with 80 μA of cw beam was established and did not cause machine trips due to the beam loss accounting system. As a result, the beam loss in CEBAF-ER is comparable to the beam loss in standard CEBAF operations [36]. A summary of beam loss in the FEL Demo, CEBAF and CEBAF with energy recovery is given in Table 2.6.

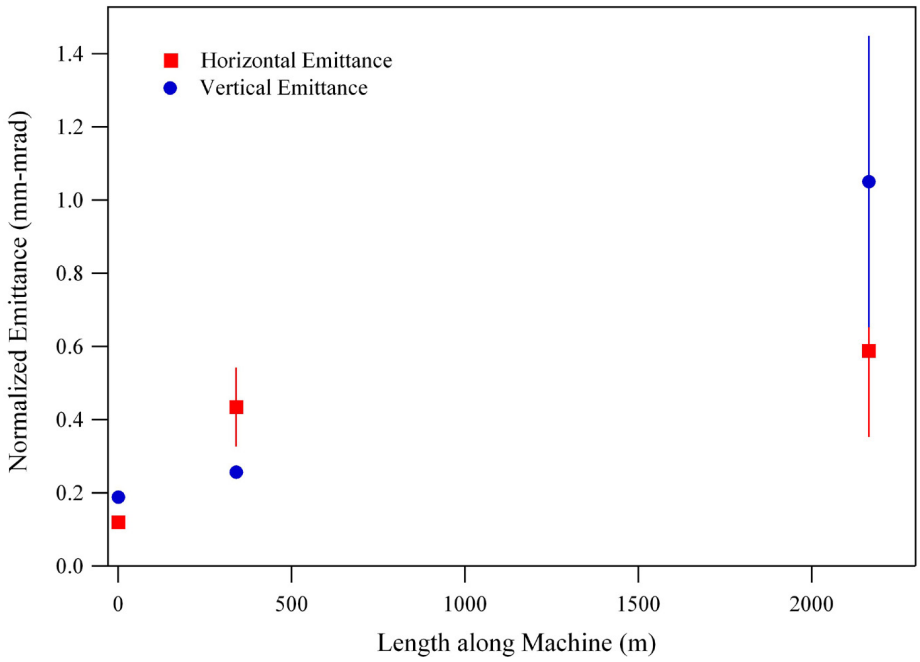

FIG. 2.20: The measured normalized transverse emittance at various locations in CEBAF for the $E_{inj} = 56$ MeV configuration.

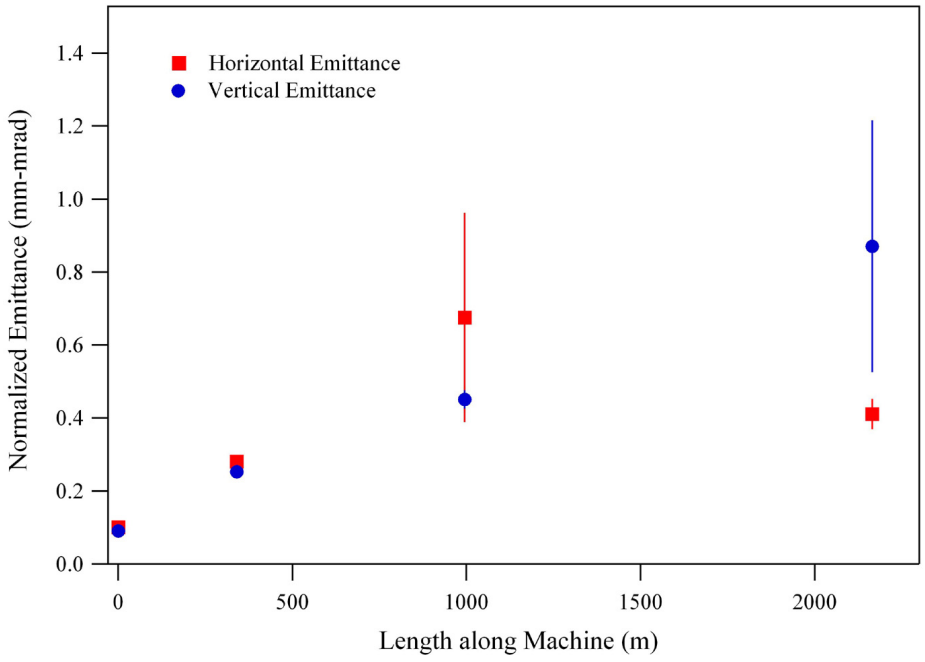

FIG. 2.21: The measured normalized transverse emittance at various locations in CEBAF for the $E_{inj} = 20$ MeV configuration.

TABLE 2.6: Comparison of beam loss in the FEL Demo Driver, CEBAF and CEBAF with energy recovery.

Machine	E_{inj} (MeV)	E_{max} (MeV)	E_{final} (MeV)	I_{ave} (μA)	I_{loss} (μA)
FEL Demo	10	48	10	5000	< 0.5
CEBAF	60	5400	5400	100	< 0.5
CEBAF-ER	56	1056	56	80	< 0.5

There were a number of challenges in performing the CEBAF-ER experiment. Despite these obstacles, however, the experiment was an important step in pushing the limits of ERL performance. Prior to CEBAF-ER, the highest energy beam to be energy recovered in an SRF environment was 48 MeV through a single cryomodule.

CHAPTER 3

The Jefferson Laboratory 10 kW FEL Upgrade Driver

3.1 Overview

The Jefferson Laboratory free electron laser Upgrade provides an ideal testbed for studying high current phenomena in ERLs. The FEL Upgrade Driver is an energy recovery based linear accelerator used to condition an electron beam for high average power lasing. Electrons are generated in a DC photocathode gun, accelerated to 7 MeV and injected into the linac where they are further accelerated up to 145 MeV through three cryomodules (each containing 8 superconducting niobium cavities). The beam is transported to an undulator where in excess of 10 kW of laser power is generated. Because the SRF linac supports cw beam, high average laser power can be achieved with a high bunch repetition rate and only modest single bunch charge. The spent electron beam is recirculated and phased in such a way that the beam is decelerated through the linac on the second pass. Upon exiting the linac, the 7 MeV energy recovered beam is extracted to a dump. A schematic of the Driver is

TABLE 3.1: Design system parameters of the 10 kW FEL Upgrade.

Parameter	Design Value
Beam energy at undulator	80-210 MeV
Average beam current	10 mA
Bunch charge	135 pC
Bunch repetition rate	up to 74.85 MHz
Normalized emittance (rms)	13 mm-mrad
Bunch length at undulator (rms)	200 fs
Peak Current	270 A
FEL extraction efficiency	1%
ΔE/E before undulator (rms)	0.5%
ΔE/E after undulator (full)	10%
CW FEL power	10 kW

displayed in Fig. 3.1. The primary system parameters (design values) are listed in Table 3.1.

Because the experimental measurements described in Chapters 5, 6 and 7 were performed with the Driver, this chapter presents the required conditions for lasing, from the standpoint of the electron beam, and how these conditions are satisfied in the FEL Driver.

Reduced to its primary objective, the Driver must generate a short bunch (high peak current) at the undulator and energy compress and energy recover the large longitudinal phase space of the spent electron beam following the undulator [49]. The injector is designed to generate a long bunch with low momentum spread. The objective of the Driver is to rotate the longitudinal phase space 90° to create a short bunch at the undulator. Following the undulator, the longitudinal phase space must be rotated back by 90° to energy compress the beam which has acquired a large momentum spread. These longitudinal phase space manipulations are achieved by accelerating the bunches off-crest through the linac to impart a phase-energy correlation. Rotation of the phase space to an upright ellipse at the undulator is accomplished with a proper choice of the momentum compaction (the

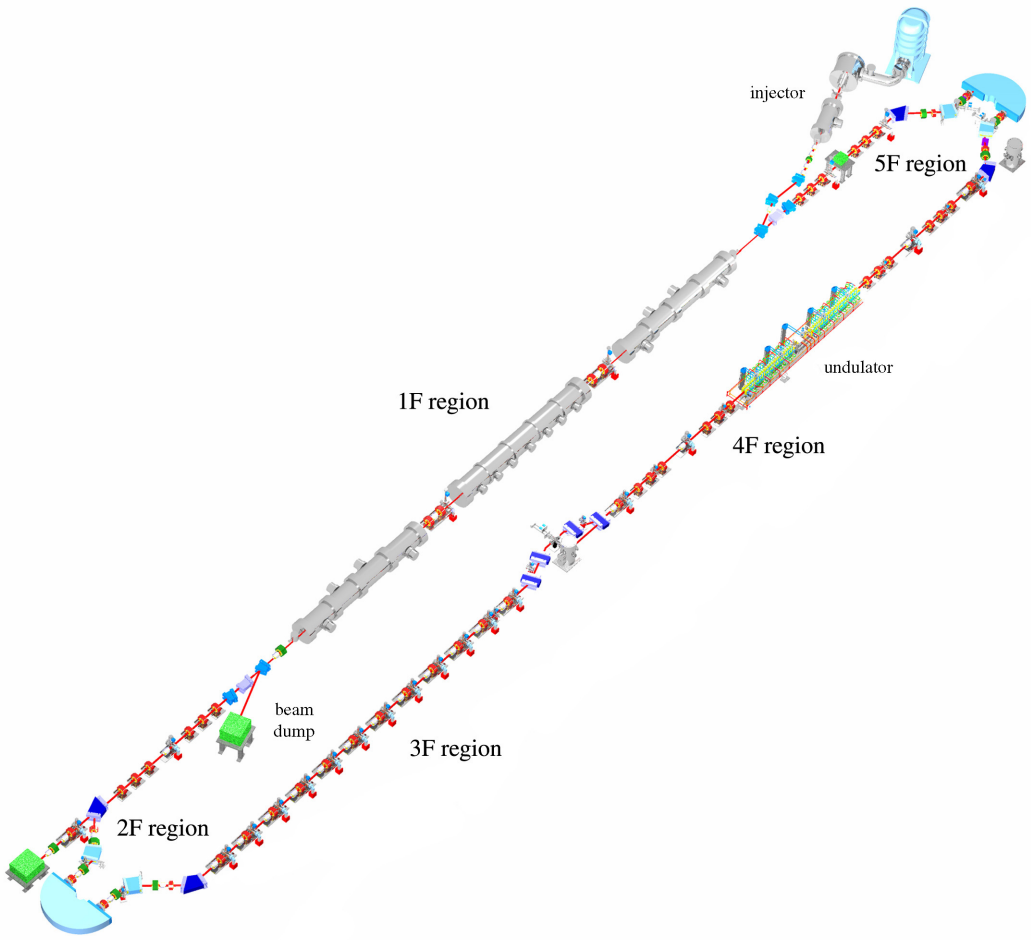

FIG. 3.1: Schematic of the 10 kW FEL Upgrade Driver.

M_{56} transfer matrix element) in the first 180° bend and in a downstream magnetic chicane. Similar longitudinal phase space manipulations are used to properly manage the beam after the undulator to the beam dump. Details of this process are described in Section 3.5.

The driver can be thought of as being comprised of an injector and injection line, a linac section and a recirculator. A brief description of each section follows.

3.2 Injector and Injection Line

The injector region consists of a DC photocathode gun, two solenoids, a buncher, quarter cryomodule (two 5-cell niobium cavities), a matching and a merger section [50]. A view of the region is given in Fig. 3.2.

The electron source is a DC photocathode gun which consists of a Gallium Arsenide (GaAs) cathode illuminated by a 527 nm laser with up to 6 W of power. A thin layer of Cesium on the surface of the cathode acts to decrease the work function. The photoelectrons are then quickly accelerated across a 350 kV voltage gap.

The first solenoidal lens focuses the rapidly diverging electron beam to a waist in the buncher. The buncher is a 1497 MHz copper cavity whose gradient is set to minimize the longitudinal emittance. The second solenoid matches the beam transversely into the quarter cryomodule (cryounit) where the bunch is accelerated from 350 keV to 7 MeV. Typically the charge per bunch is 135 pC but can be varied continuously up to this value by changing the attenuation of the drive laser beam.

Following the cryounit the beam travels to the matching section which consists of four quadrupoles and is used to generate upright phase spaces in both transverse planes. Nominal injection conditions are $\beta_x = \beta_y = 10$ m and $\alpha_x = \alpha_y = 0$. Longitudinally, the injector must produce a relatively long bunch length (2 ps rms) with a small momentum spread (0.1% rms) at the entrance to the linac. Accelerating a long bunch through the linac minimizes longitudinal HOM excitation and the attendant single bunch instabilities. Additionally, it reduces longitudinal emittance growth due to longitudinal space charge [51].

The merger section consists of a three bend achromatic geometry with each dipole providing a bending angle of 20°. The final dipole is common to the reinjection chicane which is used to merge the recirculated (high energy) beam with the injected

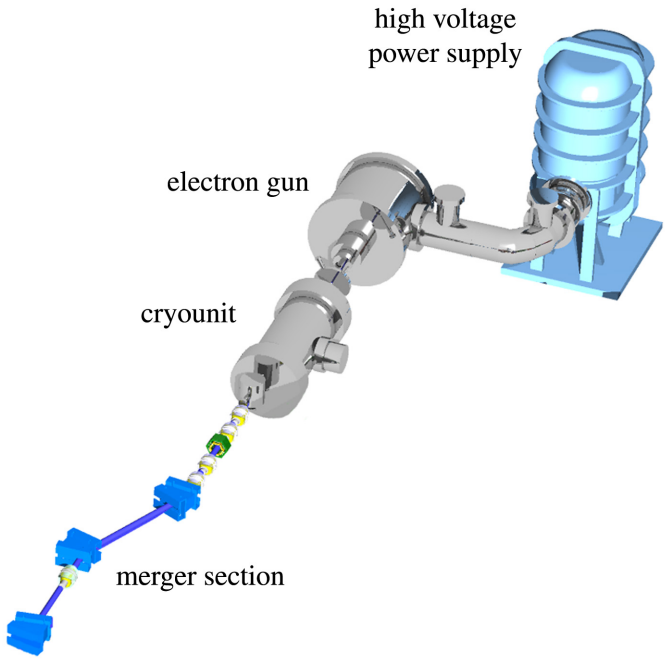

FIG. 3.2: Layout of the DC photocathode gun and injection line.

(low energy) beam.

3.3 Linear Accelerator

From the injector, the electron beam is accelerated from 7 MeV to 145 MeV by three cryomodules, each containing eight superconducting niobium cavities. The first cryomodule seen by the beam is denoted zone 2, the second zone 3 and the last zone 4. The RF cavities in zones 2 and 4 are the nominal 5-cell CEBAF cavity design, whereas the middle cryomodule, zone 3, contains a new high-gradient 7-cell cavity design. Quadrupole triplets are placed in the warm sections between cryomodules to allow for beam envelope control. Following zone 4 a dipole chicane separates and sends the energy recovered beam (7 MeV) to the beam dump, while the first pass beam begins traversing the recirculator.

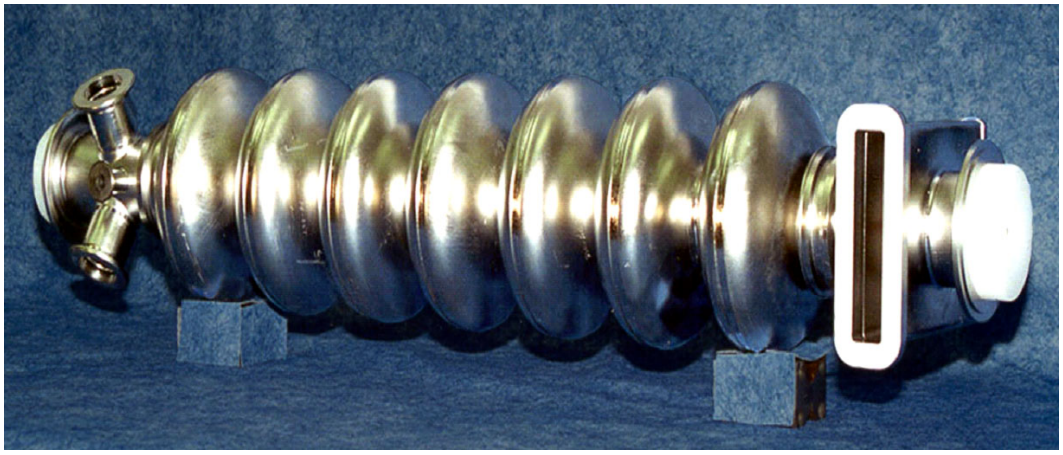

FIG. 3.3: A single 7-cell cavity with a coaxial higher-order mode coupler (left) and a waveguide fundamental power coupler (right).

Operationally, the beam is accelerated 10° off-crest (off-trough) through the linac for acceleration (energy recovery) to generate a phase-energy correlation required for longitudinal phase space matching. Among the unwanted effects of the beam and SRF cavity interactions are FPC-driven steering, RF focusing and insufficiently damped HOMs which lead to beam breakup.

The HOM coupler induced skew quadrupole driven coupling poses a problem as discussed in Section 2.2.3. The adverse effects are corrected on the first pass by skew quadrupole trims at the exit of zones 2 and 4. Zone 3 utilizes coaxial HOM couplers which do not produce a coupling kick. The 7-cell cavity design with HOM and FPC couplers is shown in Fig. 3.3. Because the induced coupling is due to an RF field and the off-trough deceleration is 180° out of phase with the quadrupole trims, the energy recovery pass suffers from twice the skew quadrupole kick. This, however, has not proved to be an operational impediment in the relatively short linacs in the ERLs to date.

The RF focusing of the low energy beams in the first and last cryomodules, of the injected and energy recovered beam, respectively, places a constraint on the

accelerating gradient at the front and back end of the linac. If the gradients are too high, the low energy beam is over focused and the transverse motion can become unstable [49].

Due to loaded Qs of dipole HOMs of order 10^6 in zone 3, beam breakup develops below the 10 mA design beam current. The threshold current of stability depends largely on the machine optics and a threshold as low as 400 μA has been observed. Conversely, using optics designed to suppress BBU, average currents of 9 mA have been achieved with no indication of beam breakup.

3.4 Recirculator

The recirculator refers to the transport line starting immediately downstream of the linac and extending to the reinjection chicane. The recirculator must condition the beam phase space appropriately for the FEL and for energy recovery. With regard to the longitudinal phase space, the former requires a short bunch while the latter requires proper management of the large momentum spread.

Following zone 4, a six quadrupole telescope is used to match the transverse beam envelopes to the first recirculation arc. The telescope uses six quadrupoles so in addition to the four parameters required for betatron matching, $(\beta_x, \alpha_x, \beta_y, \alpha_y)$, the betatron phase advances can be adjusted as well.

3.4.1 Recirculation Endloops

Each of the two recirculation loops are based on the Bates-style endloop [52]. In addition to providing low loss transmission of the beam, the endloops aid in the required longitudinal phase space matching. Each endloop is comprised of two pairs of dipoles installed symmetrically around a 180° dipole magnet as illustrated in Fig. 3.4. The dipoles bend the beam by θ $-\theta$ 180° $-\theta$ θ, where $\theta \simeq 43°$, and the

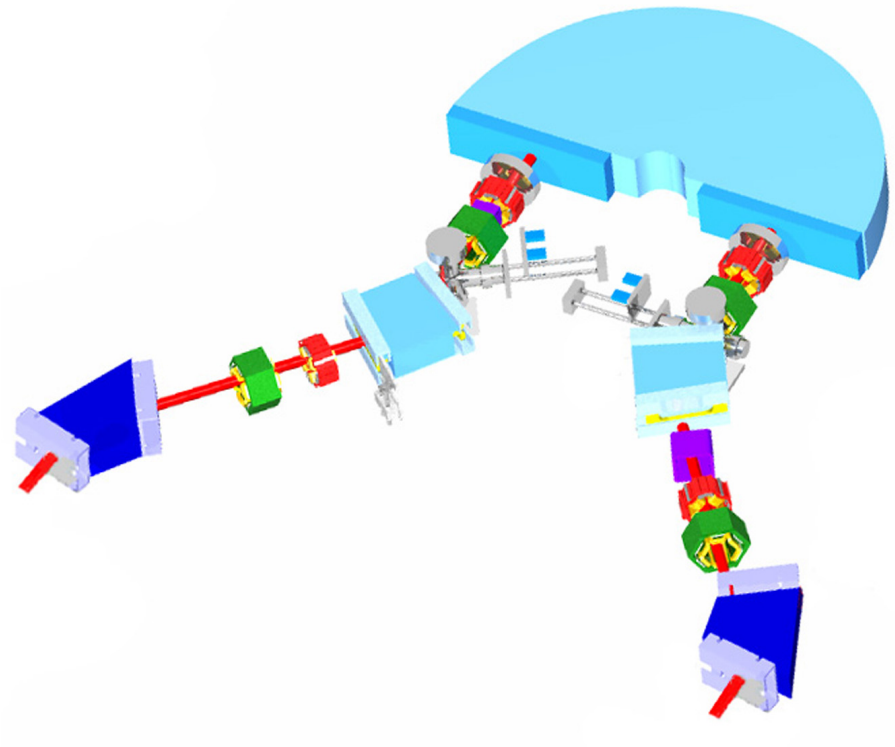

FIG. 3.4: View of the second (as seen by the beam) Bates style endloop in the FEL Upgrade Driver. The dipoles are represented in blue, the quadrupoles in red and the sextupoles in green.

endloop as a whole is achromatic.

The endloops are achromatic in the sense that the outgoing orbit is independent of the incoming momentum [53]. This means that the M_{16}, M_{26}, M_{36} and M_{46} matrix elements are zero. A simple example is a magnetic chicane comprised of four dipoles and illustrated in Fig. 3.5. An off-momentum beam, one with a lower momentum than the reference beam for example, will follow a different orbit and make a longer excursion through the system. However, by symmetry, the off-momentum beam is brought parallel to the reference trajectory at the symmetry point and will exit with the same trajectory as the on-momentum, reference beam. The Bates-style endloop is simply a modification of the four dipole chicane, wherein a 180° dipole is inserted at the symmetry point as illustrated in Fig. 3.6 [54]. The underlying

reason for making the endloops achromatic is to support a large momentum spread, particularly in the second endloop following the undulator.

The endloop has a momentum compaction, M_{56}, of +0.2 m. Note that for storage rings, the momentum compaction is defined as

$$\alpha_c \equiv \frac{\Delta L/L}{\Delta p/p} \tag{3.1}$$

whereas in the context of this dissertation, the momentum compaction refers to the M_{56} transfer matrix element which maps a change in momentum to a change in path length. Together with the momentum compaction of the downstream optical cavity chicane, the long bunch from the injector is rotated by 90° to a short bunch at the undulator. Trim quadrupoles and sextupoles located immediately upstream (downstream) of the 180° dipole's entrance (exit) provide tunable linear (M_{56}) and quadratic (T_{566}) compactions from the linac to the undulator.

In addition to providing longitudinal phase space matching to the undulator, the endloops are used to vary the path length of the electron beam. In earlier demonstrations of energy recovery, such as the injection line of CEBAF and at Stanford's SCA, the required path length differential was achieved by physically moving a portion of the recirculator. In the FEL Driver, correction coils embedded in the 180° dipoles are used for path length management [55]. For a small deflection, θ, from the coils at the entrance of the magnet, the path length becomes $(\pi + 2\theta)\rho$ where ρ is the bending radius of the dipole. This is shown schematically in Fig. 3.7. Consequently a path length differential of $2\theta\rho$ is created. To generate a path length differential of $\lambda_{RF}/2$ in a single 180° magnet (in practice both bends are used) with $\rho = 1$ m, requires a deflection of 0.05 radians.

For complete energy recovery, the path length of the machine must be $(n + \frac{1}{2})\lambda_{RF}$, where n is an integer and λ_{RF} is the wavelength of the accelerating RF frequency.

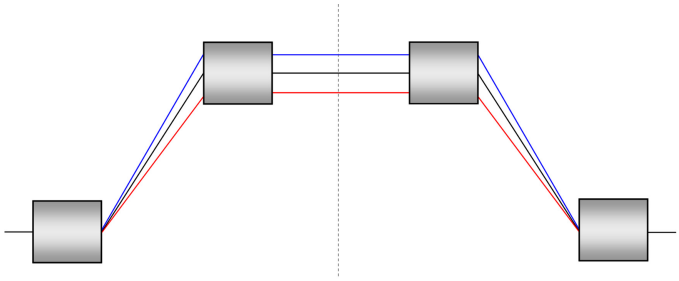

FIG. 3.5: An achromatic system comprised of four dipoles. The reference trajectory is represented by the black line and off-momentum trajectories are represented in blue (lower momentum) and red (higher momentum).

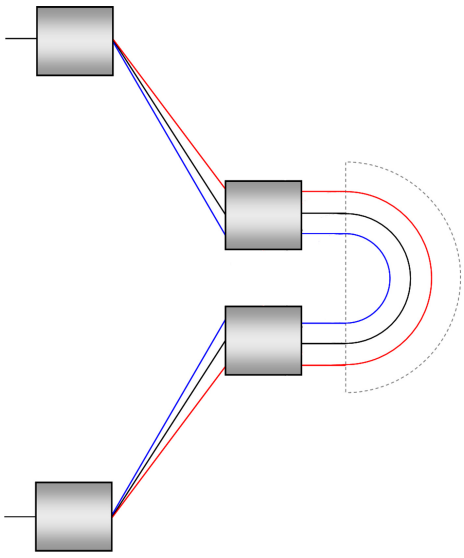

FIG. 3.6: Understanding the layout of the Bates endloop in terms of the achromat in Fig. 3.5.

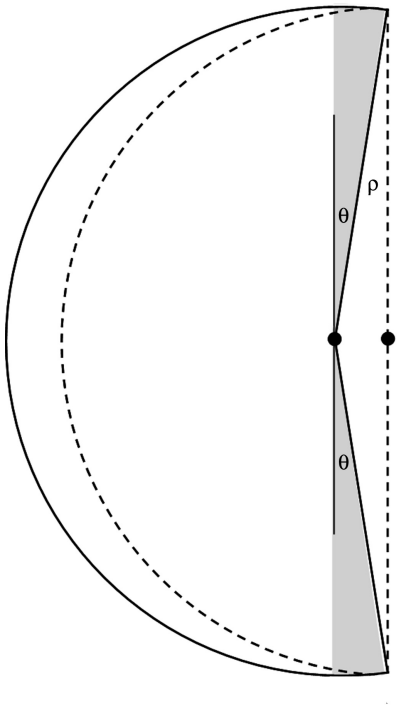

FIG. 3.7: Illustration of path length management using correctors embedded in the 180° dipole magnet.

Under this condition, the electron beam will be decelerated on the second pass through the linac. However, due to the ease with which the path length can be adjusted, a recirculation path length of $(n + \frac{1}{4})\lambda_{RF}$ can be generated as well. In this instance, the second pass beam travels through the linac at the zero crossing of the accelerating field and neither gains nor loses energy. The beam then makes a third pass through the machine and gains the appropriate path length differential, $(\frac{1}{4} + \frac{1}{4})\lambda_{RF}$, for energy recovery. This scheme of 3-pass beam operation was first demonstrated at Bates [7] and later at Jefferson Laboratory's IR FEL Demo [56] and also in the FEL Upgrade [57].

3.4.2 Backleg Region

The backleg region consists of six 90° FODO cells. In addition to matching the beam to the undulator, the FODO lattice provides the additional freedom to vary the betatron phase advances [58]. This feature was implemented to allow control of BBU through modification of the recirculation phase advance and is discussed in detail in Section 6.2. The optical cavity chicane provides -0.5 m of momentum compaction, so that from the linac to undulator, the compaction is $(+0.2 - 0.5)$ -0.3 m. Following the optical cavity chicane, a six quadrupole telescope is used to match the transverse beam envelopes to the undulator.

Note that during experimental studies of BBU, the performance of the Driver itself, without lasing, was studied.

3.4.3 Energy Recovery Transport

Following the undulator, a six quadrupole telescope is used to match the transverse beam envelopes to the second recirculation arc. The endloop is the same as the first, except that in addition to trim quadrupoles and sextupoles, there is a family of octupoles to provide tunable momentum compactions through third order.

Following the undulator the electron bunch remains short, however there is a significant momentum spread induced by the lasing process. The transport following the undulator is designed to cleanly transport a beam with up to 10% full relative momentum spread and provide adequate energy compression so as to prevent adiabatic antidamping from generating a prohibitively large momentum spread.

3.5 Longitudinal Dynamics

This section describes details of the off-crest acceleration/magnetic compression scheme that is used for bunch length compression at the undulator and energy compression at the energy recovered beam dump.

3.5.1 Analogy to Transverse Dynamics

To gain a better understanding of longitudinal phase space manipulations, it is helpful to make an analogy to transverse dynamics, which can be more intuitive. Consider the effect of a drift and then of a thin focusing element on the transverse (e.g. horizontal) phase space. The transformation of a particle with an initial displacement (zero angle) due to a drift is given by

$$\begin{pmatrix} x_f \\ x_f^{'} \end{pmatrix} = \begin{pmatrix} 1 & M_{12} \\ 0 & 1 \end{pmatrix} \begin{pmatrix} \pm x_i \\ 0 \end{pmatrix} = \begin{pmatrix} \pm x_i \\ 0 \end{pmatrix} \tag{3.2}$$

while the transformation of a particle with an initial angle (zero displacement) is given by

$$\begin{pmatrix} x_f \\ x_f^{'} \end{pmatrix} = \begin{pmatrix} 1 & M_{12} \\ 0 & 1 \end{pmatrix} \begin{pmatrix} 0 \\ \pm x_i^{'} \end{pmatrix} = \begin{pmatrix} \pm M_{12} x_i^{'} \\ \pm x_i^{'} \end{pmatrix} \tag{3.3}$$

The effect on the phase space is depicted graphically in Fig. 3.8.

The transformation of a particle with an initial displacement (zero angle) due to a thin focusing element is given by

$$\begin{pmatrix} x_f \\ x_f^{'} \end{pmatrix} = \begin{pmatrix} 1 & 0 \\ M_{21} & 1 \end{pmatrix} \begin{pmatrix} \pm x_i \\ 0 \end{pmatrix} = \begin{pmatrix} \pm x_i \\ \pm M_{21} x_i \end{pmatrix} \tag{3.4}$$

while the transformation of a particle with an initial angle (zero displacement) is given by

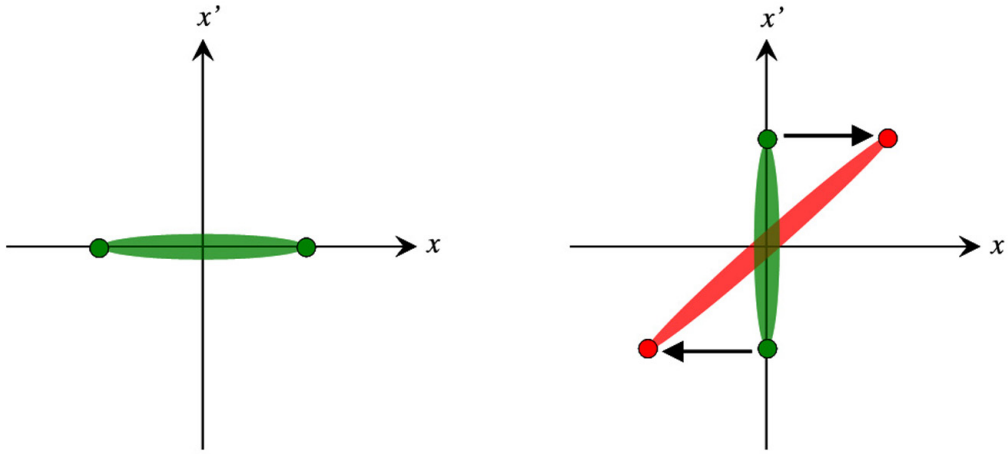

FIG. 3.8: The effect of a drift length on a displaced bunch with no initial angle (left) and on a bunch with an initial angle with zero displacement (right).

$$\begin{pmatrix} x_f \\ x_f' \end{pmatrix} = \begin{pmatrix} 1 & 0 \\ M_{21} & 1 \end{pmatrix} \begin{pmatrix} 0 \\ \pm x_i' \end{pmatrix} = \begin{pmatrix} 0 \\ \pm x_i' \end{pmatrix} \tag{3.5}$$

The effect on the phase space is depicted graphically in Fig. 3.9.

At the front end of the linac in the FEL, the bunch length is long and has a small momentum spread which is analogous to an initially displaced bunch in transverse phase space. From Eq. (3.4), inducing a correlation between the phase space variables requires a lens for focusing. In practice this is achieved by running the bunch off-crest of the accelerating RF waveform. That is, the effect of the linac on the longitudinal phase space is analogous to the effect of a focusing element in transverse phase space. In order to rotate the phase space for bunch length compression, the analog of a drift in the transverse phase space, Eq. (3.3), is required. This rotation in longitudinal phase space is achieved with a bend with nonzero momentum compaction, M_{56}.

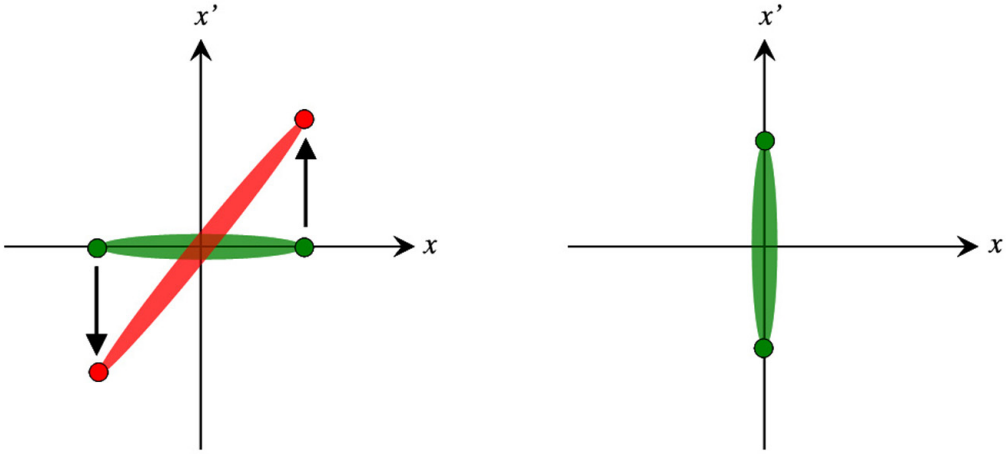

FIG. 3.9: The effect of a thin focusing element on a displaced bunch with no initial angle (left) and on a bunch with an initial angle but with zero displacement (right).

3.5.2 Deriving Proper Momentum Compactions

What follows is a brief derivation of the proper first and second order momentum compactions, M_{56} and T_{566}, respectively, so as to achieve the desired longitudinal phase space manipulations at the Upgrade Driver [59, 60].

Consider a bunch of length, ℓ_{inj} and energy, E_{inj} generated from the injector. The effect of accelerating the bunch off-crest results in a bunch length, energy spread and centroid energy at the end of the linac (denoted by a subscript l) of

$$\ell_l = \ell_{inj} \tag{3.6}$$

$$\Delta E_l = \Delta E_{inj} + \Delta E_{RF} \tag{3.7}$$

$$E_l(z=0) = E_{inj} + E_{linac}\cos\phi_o \equiv E_{max} \tag{3.8}$$

where $\Delta E_{RF} = E_{linac}\left[\cos\left(\phi_o - k_{RF}\ell_{inj}\right) - \cos\phi_o\right]$, $k_{RF} = 2\pi/\lambda_{RF}$, and ϕ_o is the off-crest acceleration phase. Assume that the energy spread from the injector is negligible, $\Delta E_{inj} = 0$. Following the linac, the beam traverses the recirculation arc.

The bunch length, energy spread and centroid energy at the end of the arc (denoted by the subscript a) can be written in terms of parameters at the end of the linac as

$$\ell_a = \ell_l + M_{56}\left(\frac{\Delta E}{E}\right)_l + T_{566}\left(\frac{\Delta E}{E}\right)_l^2 \tag{3.9}$$

$$\Delta E_a = \Delta E_l \tag{3.10}$$

$$E_a(z=0) = E_l(z=0) \tag{3.11}$$

By combining Eqs. (3.6), (3.7), (3.8) with Eqs. (3.9), (3.10), (3.11) the bunch length, energy spread and centroid energy at the undulator (denoted by the subscript u) can be written in terms of bunch parameters from the injector

$$\ell_u = \ell_{inj} + M_{56}\left(\frac{\Delta E_{RF}}{E_{max}}\right) + T_{566}\left(\frac{\Delta E_{RF}}{E_{max}}\right)^2 \tag{3.12}$$

$$\Delta E_u = \Delta E_{RF} \tag{3.13}$$

$$E_u(z=0) = E_{max} \tag{3.14}$$

Recall that the goal is to take the long bunch with low momentum spread and with an appropriate choice of optics, rotate the phase space to produce a short bunch at the undulator. That is, M_{56} and T_{566} are chosen to minimize the bunch length ℓ_u. For small values of ℓ the expression for ΔE_{RF} can be expanded to second order in ℓ_{inj} to yield

$$\Delta E_{RF} \simeq E_{linac} k_{RF} \ell_{inj}\left(\sin\phi_o - \frac{k_{RF}\ell_{inj}}{2}\cos\phi_o\right) \tag{3.15}$$

Plugging Eq. (3.15) into Eq. (3.12) and collecting like powers of ℓ_{inj} results in

$$\begin{aligned}\ell_u = \ell_{inj}&\left[1 + M_{56}k_{RF}\left(\frac{E_{linac}}{E_{max}}\right)\sin\phi_o\right] \\ &+ \ell_{inj}^2\left[-M_{56}\frac{k_{RF}^2}{2}\left(\frac{E_{linac}}{E_{max}}\right)\cos\phi_o + T_{566}k_{RF}^2\left(\frac{E_{linac}}{E_{max}}\right)^2\sin^2\phi_o\right]\end{aligned} \tag{3.16}$$

Under the constraint that each order vanishes, the desired M_{56} and T_{566} are found to be

$$M_{56} = -\frac{\lambda_{RF}}{2\pi}\left(\frac{E_{max}}{E_{linac}}\right)\frac{1}{\sin\phi_o} \tag{3.17}$$

$$\begin{aligned} T_{566} &= -\frac{\lambda_{RF}}{4\pi}\left(\frac{E_{max}}{E_{linac}}\right)^2\frac{\cos\phi_o}{\sin^3\phi_o} \\ &= -\left[\frac{\pi}{\lambda_{RF}}\frac{\cos\phi_o}{\sin\phi_o}\right]M_{56}^2 \end{aligned} \tag{3.18}$$

For a bunch operating at 10° off-crest, $E_{max} = 145$ MeV and $E_{linac} = 135$ MeV, the required M_{56} is -0.2 m and T_{566} is -3.5 m. In practice the first endloop utilizes trim quadrupoles to generate an M_{56} of $+0.3$ m (as opposed to the inherent $+0.2$ m of the endloop) [61]. This compaction, in addition to that of the optical magnetic chicane (-0.5 m) create the necessary conditions outlined above. In the FEL Upgrade typical rms bunch lengths obtained at the undulator are 200 fs in accord with design requirements, although bunch lengths as short as 120 fs have been achieved [62].

A similar analysis is used to find the conditions to transform a short bunch with a large momentum spread after the undulator to a long bunch with small momentum spread using the momentum compactions in the second recirculation arc.

CHAPTER 4

Theory and Simulation of Multipass BBU

The term "beam breakup", as used in this dissertation, refers to a type of regenerative instability that can develop in recirculating linacs. In energy recovering linacs (a specific type of recirculating linac), the maximum current can be limited by the multipass, multibunch beam breakup which occurs when the electron beam interacts with the HOMs of an RF cavity on the accelerating pass and again on the energy recovering pass. The feedback loop that is generated between the beam and the RF cavity is what distinguishes regenerative-type beam instabilities from the so-called cumulative instabilities. In the latter, interactions between several cavities act to amplify the off-axis beam displacements, but there is no closure of a feedback loop between the beam and the cavity that provided the initial kick.

The BBU instability is of particular concern in the design and operation of high average current energy recovery accelerators utilizing SRF technology, where dipole modes with very high quality factors, if not sufficiently damped, can cause BBU at currents well below the design operating current. In fact, this particular

form of beam breakup not only occurs transversely, but can also develop longitudinally through the beam's interactions with longitudinal HOMs [63]. The threshold currents for longitudinal BBU, however, are an order of magnitude larger than the thresholds for transverse BBU [64]. Therefore, only transverse BBU is considered throughout the remainder of this work.

Consider the time and frequency domain behavior of beam breakup depicted in Fig. 4.1. The bottom plot shows the beam displacement as a function of time. This represents the usual output for a particle tracking BBU simulation program, and when the displacement is neither growing nor damping, is used to define the threshold current. In this example the threshold current has clearly been exceeded as the beam motion is beginning to grow exponentially. The system simulated consists of a single cavity with two HOMs and a single recirculation. To see how the picture of beam breakup evolves in the frequency domain, Fast-Fourier Transformations (FFTs) were performed on several "slices" of the time-domain data. The FFT plots reveal that initially the frequency of both HOMs are present in the beam but as time progresses the amplitude of one mode gradually decreases until the breakup develops. At this point only a single mode remains, which deflects the beam displacement with its own frequency.

The purpose of this chapter is to introduce a model of BBU and to derive the threshold current for stability. Two different approaches to deriving the threshold current are given in Section 4.2 and Section 4.4. With a basic understanding of how BBU develops, a brief survey of the three BBU simulation codes developed at Jefferson Laboratory is given in Section 4.3 and Section 4.5. Section 4.6 describes experiments to measure the properties of dipole HOMs. From these measurements it is shown in Section 4.7 that the threshold current formula is applicable to the FEL Upgrade Driver. Finally, the results of simulations performed for the FEL Upgrade are presented in Section 4.8.

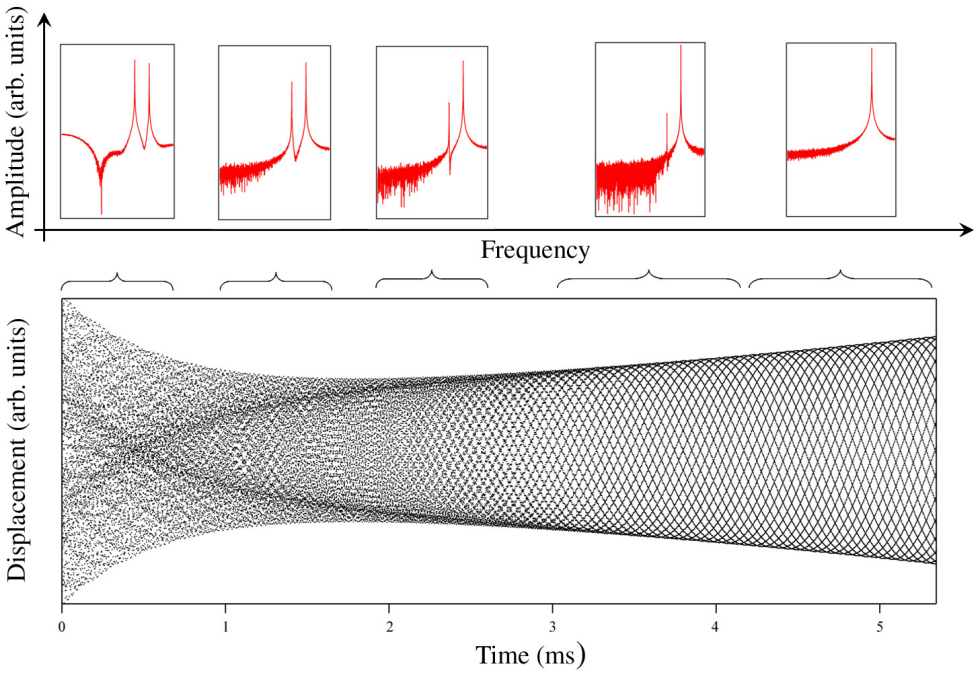

FIG. 4.1: The evolution of BBU in the time domain (bottom plot) and frequency domain (top plots). The bottom plot shows the beam displacement as a function of time for the case where the beam current exceeds the threshold current for stability. The upper plots show FFTs of the indicated time slices of the beam displacement. The left and right peaks correspond to frequencies of 2110 MHz and 2100 MHz, respectively. (Note that the horizontal and vertical scales are the same for all plots.)

4.1 The Pillbox Cavity

Although the cavities used in particle accelerators have geometries much more complicated than the simple pillbox, the advantage of the pillbox cavity is that the electric and magnetic fields can be solved analytically. These solutions offer important insights about the properties of the modes. For accelerator applications, the modes of primary interest are the transverse magnetic (TM) modes. In particular the TM_{010} mode is used for acceleration and the TM_{110} modes are those which facilitate BBU. Details of the derivation of the electric and magnetic fields of TM modes is presented in Appendix A.

4.1.1 TM_{mn0} Modes

The two components of interest, the longitudinal component of the electric field and the azimuthal component of the magnetic field, for the TM_{mn0} modes, are given by

$$E_z(\rho,\phi,z) = E_0 J_m\left(\frac{x_{mn}\rho}{R}\right)\cos(m\phi) \tag{4.1}$$

$$H_\phi(\rho,\phi,z) = iE_0\left(\frac{\epsilon_0\omega_{mn0}R}{x_{mn}}\right)J'_m\left(\frac{x_{mn}\rho}{R}\right)\cos(m\phi) \tag{4.2}$$

where $J_m(x_{mn}\rho/R)$ are Bessel functions of order m and where $x_{mn} \equiv \gamma_{mn}R$ is the n^{th} root of the Bessel function and R is the radius of the cavity (see Fig. A.1 for reference).

The TM_{010}, or monopole, mode is given by

$$E_z(\rho,\phi,z) = E_0 J_0\left(\frac{x_{01}\rho}{R}\right) \tag{4.3}$$

$$H_\phi(\rho,\phi,z) = iE_0\left(\frac{\epsilon_0\omega_{010}R}{x_{01}}\right)J'_0\left(\frac{x_{01}\rho}{R}\right) \tag{4.4}$$

and is used to accelerate charged particles due to the fact that the electric field is strongest on-axis, $\rho = 0$.

The TM_{110} modes are given by

$$E_z(\rho, \phi, z) = E_0 J_1\left(\frac{x_{11}\rho}{R}\right)\cos(\phi) \tag{4.5}$$

$$H_\phi(\rho, \phi, z) = iE_0\left(\frac{\epsilon_0\omega_{110}R}{x_{11}}\right)J_1'\left(\frac{x_{11}\rho}{R}\right)\cos(\phi) \tag{4.6}$$

The electric field vanishes on-axis, but for small off-axis displacements grows linearly. These modes are typically referred to as dipole HOMs due to the behavior of the magnetic field. A plot of the electric and magnetic fields in $\rho-\phi$ space is shown in Fig. 4.2.

With these field configurations in mind, the mechanism which facilitates BBU can be understood. The magnetic field deflects a particle on the first pass (even if it travels on-axis) and is transformed into a displacement, the magnitude of which depends on the machine optics, through the cavity on the second pass. As the particle travels off-axis through the cavity, energy can be exchanged with the electric field depending on the phase of the beam relative to the field. Under certain conditions the beam can couple energy to the HOM which in turn more strongly deflects trailing particles traveling through the cavity. Hence a feedback loop is generated between the recirculated beam and the cavity dipole HOM fields which can become unstable if the average beam current exceeds the threshold current.

4.2 Derivation of the BBU Threshold Current

In this section, the threshold current is derived by equating the energy dissipated by the cavity to the energy deposited by the beam into the HOM [65]. In Section 4.4 an alternate derivation is outlined which uses the concept of the wake

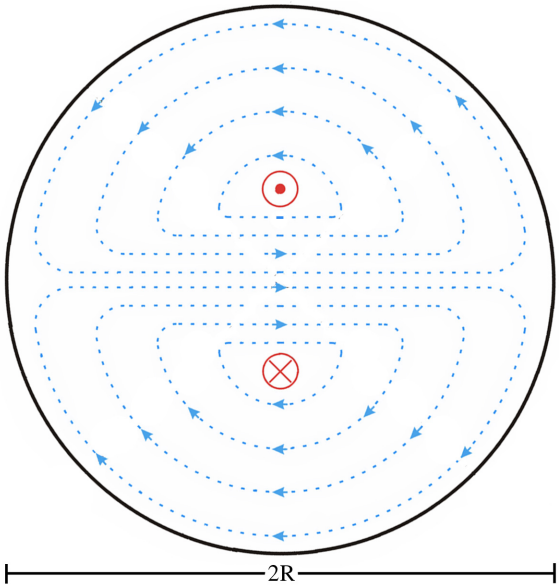

FIG. 4.2: Electric field (red) and magnetic field (blue) in the $\rho-\phi$ plane for a TM_{110} mode in a pillbox cavity.

function to describe the interaction between the HOM and beam.

Consider a two-pass energy recovering linac with a single RF cavity which contains a single dipole HOM. While it is true that dipole HOMs occur in orthogonal pairs, for reasons that will be discussed in Section 4.7, one polarization can be safely neglected for the derivation.

The change in the stored energy of a dipole HOM due to the passage of a bunch of charge q is given by

$$\Delta U = -qV_a \frac{r}{a} \cos\phi \tag{4.7}$$

where V_a is the accelerating HOM voltage at the beam pipe radius a induced by all previous bunches, r is the off-axis displacement of the bunch and ϕ is the phase of the bunch relative to the maximum HOM electric field.

In previous analytic treatments of BBU, the off-axis displacement had always been assumed to be collinear with an HOM polarized at either 0° or 90°. Now

consider an HOM polarized at an arbitrary angle, α, with respect to the x-axis. The unit vector describing the HOM polarization is $\hat{e}_{HOM} = (\sin\alpha, \cos\alpha)$ and the bunch displacement is given by

$$r = \vec{r} \cdot \hat{e}_{HOM} = x\cos\alpha + y\sin\alpha \tag{4.8}$$

On the first pass through the cavity the bunch deposits an energy to the HOM given by inserting Eq. (4.8) into Eq. (4.7)

$$\Delta U_1 = -q\frac{V_a}{a}(x_1\cos\alpha + y_1\sin\alpha)\cos\phi \tag{4.9}$$

The bunch's contribution to the energy of the HOM on the second pass through the cavity can be written in a similar manner

$$\Delta U_2 = -q\frac{V_a}{a}(x_2\cos\alpha + y_2\sin\alpha)\cos(\phi + \omega T_r) \tag{4.10}$$

where x_2 and y_2 denote the second pass displacements, ω is the HOM angular frequency and T_r is the recirculation time of the machine. The additional phase term includes the effects of the beam recirculation. Note that this derivation assumes that the variation of the HOM voltage on the time scale of the recirculation time is negligible.

The horizontal displacement on the second pass can be rewritten in terms of the first pass coordinates and the HOM imparted angular kick as

$$x_2 = M_{11}x_1 + M_{12}x_1^{'} + M_{13}y_1 + M_{14}y_1^{'} - \frac{qV_a}{\omega a p_b}(M_{12}\cos\alpha + M_{14}\sin\alpha)\sin\phi \tag{4.11}$$

and likewise for the vertical plane

$$y_2 = M_{31}x_1 + M_{32}x_1^{'} + M_{33}y_1 + M_{34}y_1^{'} - \frac{qV_a}{\omega a p_b}(M_{32}\cos\alpha + M_{34}\sin\alpha)\sin\phi \tag{4.12}$$

where the full 4×4 transfer matrix has been used to take into account coupled transverse motion and represents another feature of this derivation which hitherto had been neglected in analytic treatments of BBU. The HOM angular kick is expressed as $V_\perp/(c/e)p_b$ where p_b is the momentum of the beam bunch at the cavity and with

$$V_\perp = -\frac{c}{\omega}\frac{V_a}{a}\sin\phi \tag{4.13}$$

The average power deposited by the beam in the HOM is expressed as

$$\dot{U}_{beam} = \langle \Delta U_1 + \Delta U_2 \rangle \cdot f_b \tag{4.14}$$

where f_b is the bunch repetition frequency. While the beam deposits energy in the HOM, power is also dissipated on the cavity walls and leaks through the couplers. The total power dissipated is given by

$$P_{tot} = \frac{V_a^2}{a^2\left(\frac{\omega}{c}\right)^2\left(\frac{R_d}{Q_o}\right)Q_L} \tag{4.15}$$

where (R_d/Q_o) is in Ohms and Q_L is the loaded quality factor of the mode. The complete energy balance equation is given by

$$\dot{U} = \dot{U}_{beam} - P_{tot} = \langle \Delta U_1 + \Delta U_2 \rangle \cdot f_b - P_{tot} \tag{4.16}$$

Averaging with respect to the phase, ϕ, ultimately yields

$$\begin{aligned} \dot{U} &= I_o\frac{qV_a^2}{\omega a^2 p_b}M^*\langle \sin\phi\cos(\phi+\omega T_r)\rangle - \frac{V_a^2}{a^2(\omega/c)^2(R_d/Q_o)Q_L} && (4.17)\\ &= -I_o\frac{qV_a^2}{\omega a^2 p_b}M^*\frac{\sin(\omega T_r)}{2} - \frac{V_a^2}{a^2(\omega/c)^2(R_d/Q_o)Q_L} && (4.18) \end{aligned}$$

where

$$M^* \equiv M_{12}\cos^2\alpha + (M_{14} + M_{32})\cos\alpha\sin\alpha + M_{34}\sin^2\alpha \tag{4.19}$$

The threshold current is defined as the condition for which the power dissipated by the cavity is exactly compensated by the power deposited by the beam and occurs when $\dot{U} = 0$. Applying this condition to Eq. (4.18) yields

$$I_{th}\frac{qM^*}{2\omega p_b}\sin(\omega T_r) + \frac{1}{k^2(R_d/Q_o)Q_L} = 0 \tag{4.20}$$

and the threshold current for instability is given by

$$I_{th} = -\frac{2V_b}{k(R_d/Q_o)Q_L M^* \sin(\omega T_r)} \tag{4.21}$$

where $V_b = p_b(c/q)$ is the beam voltage and M^* is defined in Eq. (4.19). Despite the simplicity of Eq. (4.21), it is important for gaining insights into the parametric dependence of the threshold current. The formula depends on parameters that characterize the electron beam, the machine optics and properties of the HOM.

The threshold is directly proportional to the beam energy. That is, at higher energies, the beam is more rigid and will be deflected less for a given HOM angular kick. This implies that the front end of the linac, where the injected beam is only a few MeV, can be particularly susceptible to BBU.

The threshold also depends on the details of the machine lattice. Specifically it is inversely proportional to the matrix elements that transform an HOM-induced kick on the first pass to a displacement on the second pass. Large values of these matrix elements (M_{12} or M_{34} with decoupled optics, for example) will lead to large off-axis displacements in the cavity and, given the correct phase $\sin(\omega T_r)$, the beam will deposit energy proportional to the displacement into the HOM. In fact, a poorly designed optics can contribute to a low threshold current just as surely as insufficiently damped HOMs.

The threshold is inversely proportional to the HOM impedance and is also sensitive to the polarization of the mode. The ratio (R_d/Q_o) is a quantity that depends purely on the geometry of the cavity structure. The goal in designing RF cavities for high current applications is to provide strong HOM damping and thereby decrease the Q_L of HOMs. For a physically viable solution, the threshold current must be positive, which requires that the quantity $M^* \sin(\omega T_r)$ be less than zero. The regions for which the formula is valid are discussed more fully in Section 4.2.1.

As a brief aside, note that there can sometimes arise confusion when it comes to defining the ratio (R/Q) for dipole HOMs [66]. Codes such as MAFIA track particles a distance, a, off-axis through the cavity and use the accelerating voltage to compute (R_d/Q_o) as

$$\frac{R_d}{Q_o} = \frac{V_a^2}{\omega U} \tag{4.22}$$

with units of Ω/cm^2. This can be misleading because it implies that (R_d/Q_o) is a function of the off-axis displacement. The convention throughout this dissertation uses the definition

$$\frac{R_d}{Q_o} = \frac{V_\perp^2}{\omega U} \tag{4.23}$$

where $V_\perp$ is the transverse deflecting voltage and (R_d/Q_o) is in units of Ohms. The transverse voltage is proportional to the magnetic field, which for a TM_{110} mode, is constant for small values of the off-axis displacement. Converting between the two definitions is achieved using the relation

$$V_a = (ka)V_\perp \tag{4.24}$$

where k $(= \omega/c)$ is the wavenumber.

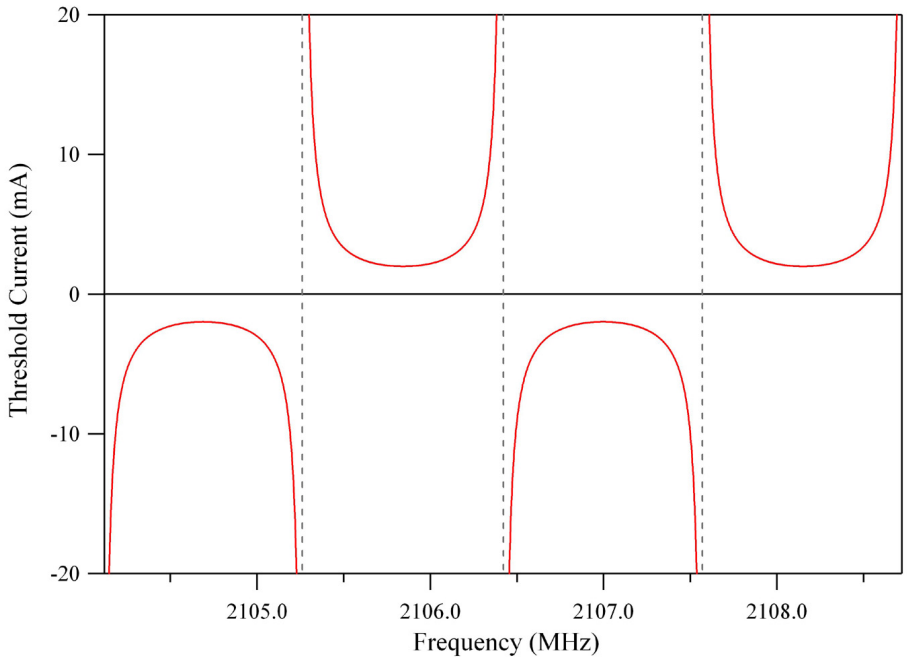

FIG. 4.3: A plot of the threshold current versus HOM frequency as described by Eq. (4.21). For positive threshold currents the formula is valid while for negative values, numerical methods must be used to determine the value of the threshold.

4.2.1 Discussion

Equation (4.21) is a good approximation only under the condition that the quantity $M^* \sin(\omega T_r)$ is less than zero. If $M^* \sin(\omega T_r)$ is positive, Eq. (4.21) yields a negative threshold current which implies absolute beam stability. A plot of the threshold current as a function of HOM frequency is given in Fig. 4.3 where the regions of instability (where the model is valid) and stability (where the model fails) are clearly distinguished. However, the beam can still go unstable at extremely high values of the beam current even if $M^* \sin(\omega T_r) > 0$ [67]. This discrepancy is caused by the assumption that the voltage induced by the beam on the second pass is a small perturbation to the HOM voltage, which fails for beams with a large charge per bunch. The dependence of the threshold for positive values of $M^* \sin(\omega T_r)$ was predicted analytically and observed in simulations by others [14, 68, 69, 65].

4.3 BBU Simulation Codes: Particle Tracking

In the previous section an analytic expression for the threshold current of stability for a cavity containing a single HOM was derived. While this is helpful for studying simple cases and understanding the parametric dependence of the threshold current, investigating BBU in an accelerator with several cavities and many HOMs per cavity and/or with coupled transverse optics requires computer simulation codes.

4.3.1 Generic Algorithm

The two particle tracking codes developed at Jefferson Laboratory are TDBBU (Two Dimensional Beam Breakup) discussed in Section 4.3.2 and ERLBBU (Energy Recovering Linac Beam Breakup) discussed in Section 4.3.3. The basic algorithm that is common to all particle tracking BBU codes is described by the following steps (for the sake of simplicity assume that only a single cavity with a single vertically polarized HOM is being simulated):

1. The initially empty machine is filled with $(P_L/h)+1$ bunches (truncated to the nearest integer), where P_L is the recirculation path length in terms of RF wavelengths and h is the beam repetition subharmonic. For the typical 74.85 MHz repetition rate used in the FEL Upgrade and with the 1497 MHz CEBAF cavities, $h = 20$.

2. An injected bunch propagates through the entire linac for the first time. Beam bunches up to a specified time are given an initial displacement and/or an initial angle to excite the HOM. During its passage, the bunch excites the HOM voltage according to

$$V_{\mathbb{R}} = \frac{\omega^2}{2c}\frac{I_o}{f_{RF}/h}(R_d/Q_o)\, y_{c,1} \tag{4.25}$$

where $V_{\mathbb{R}}$ is the real component of the HOM voltage and $y_{c,1}$ is the first pass displacement of the bunch through the cavity. The real component of the voltage corresponds to the electric field and is the means by which the beam bunch couples to the HOM.

3. The bunch is deflected by the HOM excited by the passage of previous bunches according to

$$\Delta y'_{c,1} = \frac{V_{\mathbb{I}}}{V_b} \tag{4.26}$$

where $V_{\mathbb{I}}$ is the imaginary component of the voltage and corresponds to the magnetic field. The location of the kick, depending on the simulation code and the manner in which the input file is configured, can occur immediately before or after the location of the accelerating cavity where the energy gain is implemented. After its passage, the bunch coordinates are stored in an array. The array contains all bunches present in the linac on the first pass and in the recirculation pass.

4. Before the arrival of a recirculated bunch, the HOM voltage decays according to

$$\begin{pmatrix} V_{\mathbb{R}} \\ V_{\mathbb{I}} \end{pmatrix}_{t+dt} = e^{-\frac{\omega dt}{2Q_L}} \begin{pmatrix} \cos(\omega\, dt) & -\sin(\omega\, dt) \\ \sin(\omega\, dt) & \cos(\omega\, dt) \end{pmatrix} \begin{pmatrix} V_{\mathbb{R}} \\ V_{\mathbb{I}} \end{pmatrix}_{t} \tag{4.27}$$

where dt is the time interval between an injected bunch into the linac and a recirculated bunch.

5. The first pass beam is propagated from the cavity through the recirculator and back to the cavity according to a user-input transfer matrix.

6. The second pass beam bunch then induces a voltage in the cavity according to Eq. (4.25) where $y_{c,1}$ is replaced by the second pass displacement.

7. The bunch coordinates and the HOM voltages (real and imaginary) are written to a data file for off-line analysis.

8. The cavity voltage is allowed to decay according to Eq. (4.27) where now dt represents the time interval between the recirculated bunch and the next injected bunch.

Steps 2 through 8 are repeated until the simulation time exceeds the specified run time. The simulations also utilize a binary search algorithm to automatically search for the threshold current.

4.3.2 TDBBU

The first particle tracking BBU code developed was written in FORTRAN and called TDBBU [70, 71]. The code can handle transverse coupled motion as well as arbitrary mode polarizations. However, until the derivation of the two-dimensional threshold current formula, Eq. (4.21), the effect of mode polarization was not investigated in any detail. The code was used extensively at Jefferson Laboratory to study BBU in the CEBAF accelerator and in the IR FEL Demo.

4.3.3 ERLBBU

The most recent code at Jefferson Laboratory was written in C++ in 2005 and is called ERLBBU [65]. In addition to being able to handle coupled transverse optics and arbitrary mode polarizations, it runs an order of magnitude or more faster than either TDBBU or MATBBU (discussed in Section 4.5.1). ERLBBU was

benchmarked against both existing codes and was the primary code used to study the effects of BBU in the FEL Upgrade Driver.

4.4 Alternate Derivation of the BBU Threshold Current

As electron bunches travel through the accelerator, they generate electromagnetic fields which interact with their surrounding environment (e.g. the vacuum chamber and RF cavities) and are called wakefields.

After passing through an RF cavity the transverse momentum of a trailing test charge is affected by the fields generated by the source particle. Consider a wakefield generated by an exciting charge, q_e, traveling with coordinates $\vec{r} = (x', y', z')$ which, in turn, applies a force to the test charge, q_t, following at a distance $c\tau$ behind the source. Restricting the beam motion to the x direction, the wake force is

$$\frac{c}{q_t}\frac{dp_x}{dz} = E_x(\vec{r}, z/c + \tau; d) - cB_y(\vec{r}, z/c + \tau; d) \tag{4.28}$$

The wake function is defined as

$$W_1(\tau) \equiv \left(\frac{c}{q_e q_t d}\right) \Delta p_x(\tau, d) \tag{4.29}$$

Solving for the change in transverse momentum in Eq. (4.28) and plugging into Eq. (4.29) yields

$$W_1(\tau) = \frac{1}{q_e d}\int_{-\infty}^{\infty} \left[E_x(\vec{r}, z/c + \tau; d) - cB_y(\vec{r}, z/c + \tau; d)\right] dz \tag{4.30}$$

For several cases, analytic solutions of the wake function can be derived. The net effect on the beam due to wakefields is described by the wake potential and is determined by the convolution of the wake function with the charge distribution

which excites it. The BBU instability is generated by dipole HOMs which couple to the beam through the dipole moment of the current. Thus the net effect on the beam, imparted by the transverse deflecting voltage, is given by the integral [67]

$$V(t) = \int_{-\infty}^{t} W_1(t-t')I(t'-T_r)r_2(t')dt' \tag{4.31}$$

where $W_1(t)$ is the delta functional dipole wake function and $I(t)r_2(t)$ is the dipole moment of the beam bunch when it passes the cavity at time t. Equation (4.31) represents the starting point for an alternate derivation of the BBU threshold current using a wake function formalism.

For a single dipole higher-order mode with angular frequency ω and loaded quality factor Q_L, the long-range wake function can be expressed analytically as

$$W_1(t-t') = \left(\frac{R_d}{Q_o}\right)\frac{\omega k}{2}\, e^{-\frac{\omega}{2Q_L}(t-t')}\sin(\omega(t-t')) \tag{4.32}$$

where k is the wavenumber. The bunch displacement at the cavity on the second pass can be written in terms of the voltage kick due to the accumulated wake excited by all preceding bunches and in terms of the appropriate matrix elements describing a single recirculation from the cavity back to itself as

$$r_2(t') = \frac{V(t'-T_r)}{V_b}(M_{12}\cos^2\alpha + (M_{14}+M_{32})\sin\alpha\cos\alpha + M_{34}\sin^2\alpha) \tag{4.33}$$

where α is the mode polarization and $V_b = p_b(c/q)$ is the beam momentum at the cavity. The beam bunches are approximated by delta functions

$$I(t'-T_r) = I_o t_o \sum_n \delta(t'-T_r-nt_o) \tag{4.34}$$

where t_o is the bunching period. Plugging in Eqs. (4.32), (4.33) and (4.34) into Eq. (4.31) leads to an integral equation. Assuming a normal mode solution of the form

$$V(t) = V_o e^{-i\Omega t} \tag{4.35}$$

and integrating over the delta function yields

$$e^{-i\Omega t} = \frac{K I_o e^{-\frac{\omega}{2Q_L}(t-T_r)}}{2i} \sum_{n=-\infty}^{\ell} \left\{ e^{i\omega(t-T_r)} e^{n\left(\frac{\omega}{2Q_L} - i(\Omega+\omega)\right)t_o} - e^{-i\omega(t-T_r)} e^{n\left(\frac{\omega}{2Q_L} - i(\Omega-\omega)\right)t_o} \right\} \tag{4.36}$$

where

$$K \equiv \left(\frac{t_o \omega k (R_d/Q_o) M^*}{2V_b} \right) \tag{4.37}$$

and M^* is given by Eq. (4.19). The upper limit of the summation, ℓ, is given by

$$\ell = \frac{t - T_r}{t_o} \tag{4.38}$$

Equation (4.36) takes the form of a geometrical series

$$\sum_{n=-\infty}^{\ell} e^{nz_\pm} = \frac{e^{(\ell+1)z_\pm}}{e^{z_\pm} - 1} \tag{4.39}$$

with

$$z_\pm = \left(\frac{\omega}{2Q_L} - i(\Omega \pm \omega) \right) \tag{4.40}$$

Explicitly summing the terms, and after a fair amount of algebra, the sum can be written in the compact form

$$\frac{1}{I_o} = K e^{i\Omega T_r} \left(\frac{\xi \sin(\omega t_o)}{1 - 2\xi \cos(\omega t_o) + \xi^2} \right) \tag{4.41}$$

where

$$\xi \equiv e^{\frac{\omega t_o}{2Q_L}} e^{-i\Omega t_o} \tag{4.42}$$

Equation (4.41) is a dispersion relation between I_o and Ω which must, in general, be solved numerically [14, 72]. Consider a perturbative solution by treating the case when $K \ll 1$. The frequency can be approximated to first-order in K by [67]

$$\Omega = a + bK \tag{4.43}$$

Plugging Eq. (4.43) into Eq. (4.41) and expanding exponentials to first order in K yields a and b. The constants are given by

$$a = -\frac{i\omega}{2Q_L} \mp \omega \tag{4.44}$$

$$b = \mp \frac{1}{2t_o} e^{\frac{\omega T_r}{2Q_L}} e^{\mp i\omega T_r} \tag{4.45}$$

It follows that Ω is given by

$$\Omega = \mp\omega - \frac{i\omega}{2Q_L} \mp \left(\frac{I_o}{2t_o} e^{\frac{\omega T_r}{2Q_L}} e^{\mp i\omega T_r} \right) K \tag{4.46}$$

The instability develops when the imaginary part of Ω goes to zero. That is,

$$\mathbb{I}\mathrm{m}(\Omega) = -\frac{\omega}{2Q_L} \left[1 - \frac{I_o}{I_{th}} \right] \tag{4.47}$$

where

$$I_{th} = -\frac{2V_b}{k(R_d/Q_o)Q_L M^* \sin(\omega T_r) e^{\frac{\omega T_r}{2Q_L}}} \tag{4.48}$$

For the assumptions used in the derivation, namely that the change in the HOM voltage is negligible on the time scale of a single recirculation, the exponential in the denominator of Eq. (4.48) can be neglected and the result is in perfect agreement with Eq. (4.21) derived in Section 4.2.

Since the remainder of this dissertation deals specifically with the properties of dipole HOMs, the subscripts will be dropped from the ratio (R_d/Q_o) and will be quoted simply as (R/Q).

4.5 BBU Simulation Codes: Eigenvalue Solutions

While most existing BBU simulation codes are based on the particle tracking algorithm discussed in Section 4.3, a notable exception is the code MATBBU (Matrix Beam Breakup).

4.5.1 MATBBU

The simulation code MATBBU developed at Jefferson Laboratory was used to predict the threshold currents in the IR FEL Demo as well as the FEL Upgrade Driver [73, 68]. Unlike its predecessor TDBBU, MATBBU solves for the threshold current analytically, making use of the dispersion relation that exists between the beam current and frequency, Eq. (4.41) [26]. Numerically, solutions can be found by determining the current I_o as a function of real Ω while scanning in frequency [72]. At sufficiently high current the beam motion becomes unstable which is marked by the complex frequency having a positive imaginary part. The point at which this frequency intersects the real axis of the complex current plane gives the threshold current [69]. By sweeping the frequency, MATBBU can locate these instabilities, specifying the frequency and current at which they occur. This process is illustrated in Fig. 4.4 which shows the results of scanning the frequency in the complex current plane. The lowest current to intersect the real current axis defines the threshold current and is shown in the inset figure.

Because of its unique approach to predicting the threshold current, MATBBU is able to determine the threshold current corresponding to many individual modes.

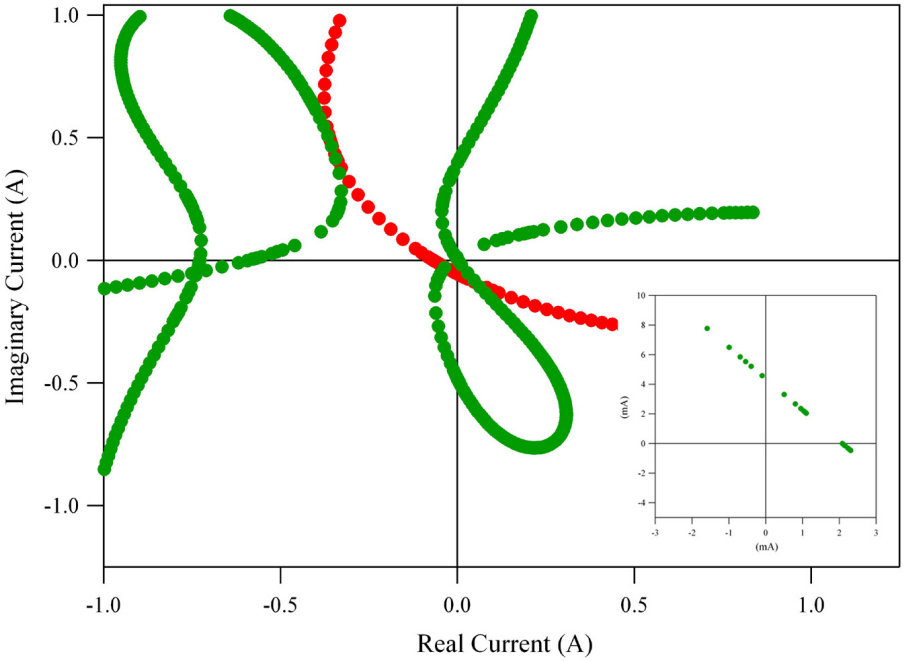

FIG. 4.4: Output from MATBBU showing the results of scanning the frequency in the complex current plane for the horizontal (red) and vertical (green) planes. The inset figure shows the region around the origin where the lowest current to intersect the real current occurs at 2.1 mA.

This capability is especially useful for gaining insight into how good (or poor) the HOM spectra are. For example, it can determine if there exist a myriad of HOMs which lead to low threshold currents or if it is due to a single, particularly bad HOM.

4.6 Measuring HOM Parameters

In order to adequately benchmark the BBU simulation codes, it is imperative that as many of the input parameters as possible be measured directly. The data required by the simulations can be divided into categories that describe; (1) the beam parameters (2) the machine optics and (3) the HOM parameters. The beam parameters, such as average current and energy, are well known from the accelerator diagnostics. Characterizing the machine optics is discussed in more detail in

Section 5.5. In the following two sections, measurements of the HOM frequency, Q_L and polarization, which are used to characterize the HOMs, are discussed in detail.

4.6.1 RF Measurements of the Zone 3 Cryomodule

In February 2004, the zone 3 cryomodule was moved into the FEL vault for installation and commissioning. Initially, the cryomodule sat parallel to its final destination on the beamline so it could be commissioned in parallel with standard FEL operations. When the cryomodule was cooled to 2 K, and before the final waveguides were installed, measurements of the HOM parameters were performed. For each of the eight cavities, the frequencies and loaded quality factors of the TM_{010} fundamental passband and TE_{111} and TM_{110} dipole mode passbands were measured. The details of the setup for measuring the HOM parameters are shown pictorially in Fig 4.5.

A network analyzer (NWA) was used to manually measure the S_{21} scattering transmission parameter (see Appendix B). This involves using port 1 of the NWA to excite the cavity through the fundamental power coupler. The FPC is connected to a WR-650 waveguide-to-coaxial adapter (frequently called a top hat). The top hat is used to provide the proper impedance match from the waveguide to a 50 Ω coaxial cable. Port 2 of the NWA is connected to the cavity's HOM1 port while the field probe and HOM2 ports are terminated in 50 Ω loads. This completes the S_{21} measurement.

A manual search and measurement of each HOM is necessary. The frequency of individual HOMs are measured with an accuracy of up to 1 kHz. The loaded quality factor of each mode is found from the center frequency divided by the bandwidth between the -3 dB points. A typical HOM resonance curve with markers at the -3 dB points is shown in Fig. 4.6. In some instances, the interference of neighboring

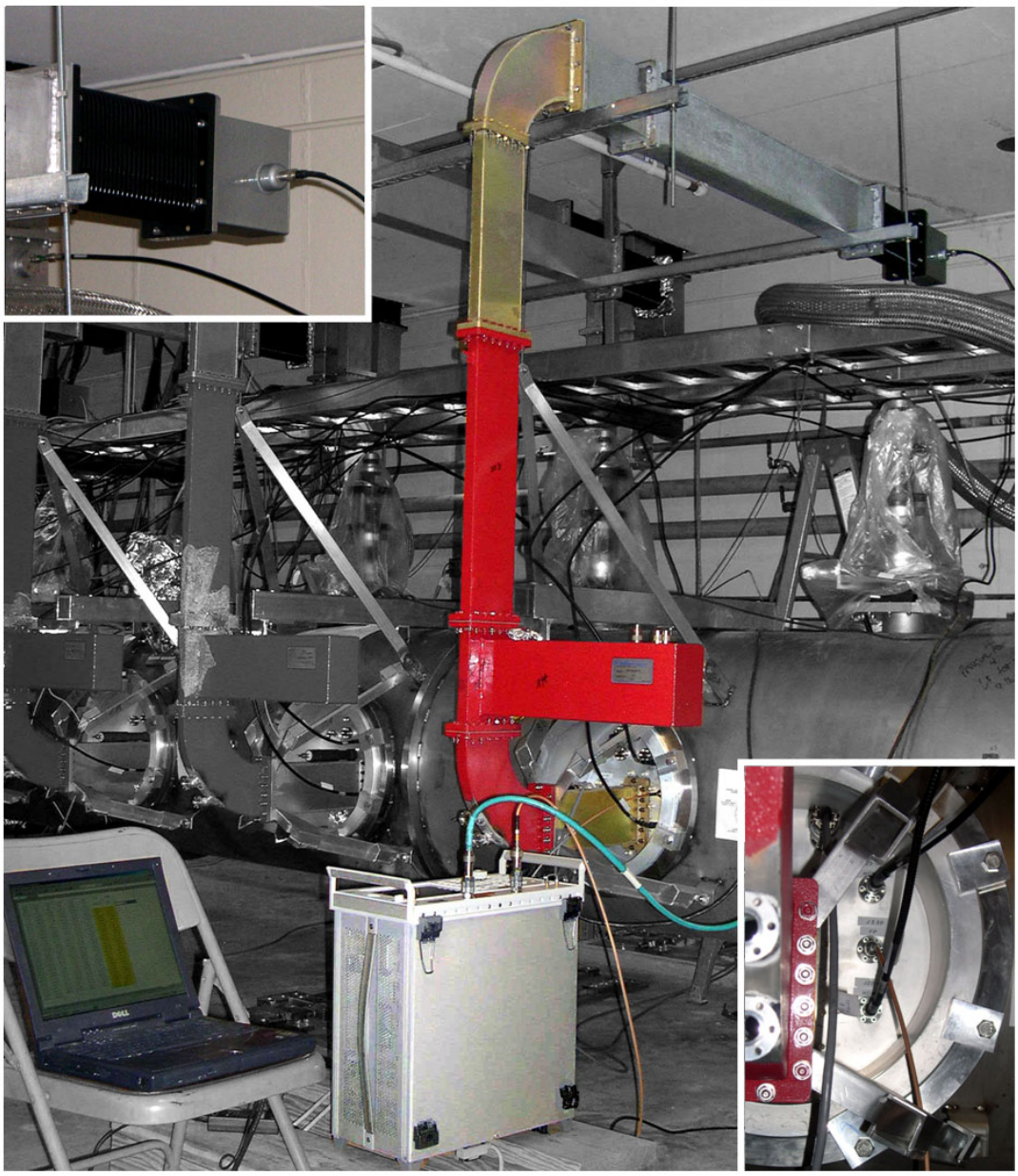

FIG. 4.5: Setup for measuring cavity HOMs of zone 3 in the FEL vault. The upper left inset shows the top hat and the lower right inset shows the connections to HOM ports.

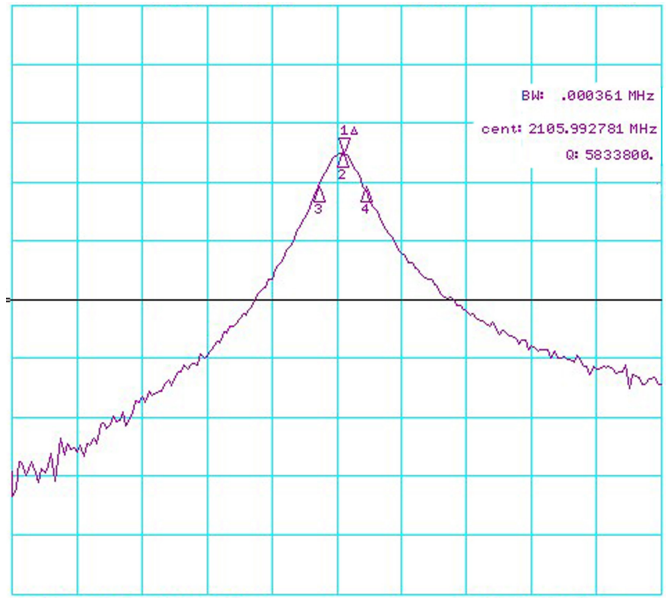

FIG. 4.6: A screenshot of a typical HOM resonance curve. Markers are placed at the center frequency and at the -3 dB points to extract the Q_L.

modes created difficulty because only a partial bandwidth could be measured. In such cases the $\pm 45°$ points of the phase spectrum were used to calculate the bandwidth. A summary of the measured data is presented in graphical form and given in Appendix C.

4.6.2 Beam-based HOM Polarization Measurements

In light of Eq. (4.21), an important parameter in characterizing HOMs is the polarization of the modes. Prior to experimentally measuring these values, BBU simulations were performed with dipole HOM pairs assigned orientations of $0°$ and $90°$ and then repeated with orientations of $90°$ and $0°$ degrees, with the threshold taken as the lowest of the two cases. Essentially only worst case scenarios were simulated. In principle, bead pull measurements can be used to extract mode polarizations. However, the small geometric perturbations from cavity to cavity introduced during the fabrication process leads to a unique HOM spectrum for each cavity.

Consequently, depending on the extent of the perturbations, the same mode can be oriented differently from one cavity to the next. Therefore, it becomes necessary to use beam-based methods to accurately measure HOM polarizations.

The measurement required that only the first pass beam be transported through the linac. To prevent the second pass (energy recovered) beam from propagating through the linac, the beam was directed to an insertable dump in the recirculator. Because it is a low power dump it could only tolerate tune-up beam (250 μs long macropulses with a 4.678 MHz bunch repetition rate every 2 Hz).

Initial attempts to measure the polarizations used a NWA to excite a specific HOM frequency through the cavity HOM coupler. Using a downstream BPM, the resulting displacement in the vertical and horizontal planes due to the angular kick imparted to the beam by the dipole HOM could be monitored and used to calculate the polarization. In principle this is a straightforward measurement, but was never successful because cw beam is required to adequately couple to the HOM.

The experimental setup that finally enabled the polarizations to be measured was based on the idea that, rather than excite the HOM externally and measure its effect on the beam, one should use the electron beam to excite the HOM and measure the response of the HOM itself. When the beam passes through a cavity, it can excite cavity HOMs. The voltage of dipole HOMs induced by a beam pulse depends on a number of beam and HOM parameters such as the bunch repetition rate, pulse length and the HOM frequency. However, most importantly for our measurement is the fact that the voltage of dipole HOMs depends linearly on the beam displacement in the cavity.

The beam was displaced in each plane independently using either an upstream vertical corrector or a horizontal corrector. The corrector was changed by $\pm$150 G-cm, in increments of 50 G-cm, from its nominal setpoint while the response of the HOM of interest was measured by a network analyzer, zero-spanned at the frequency

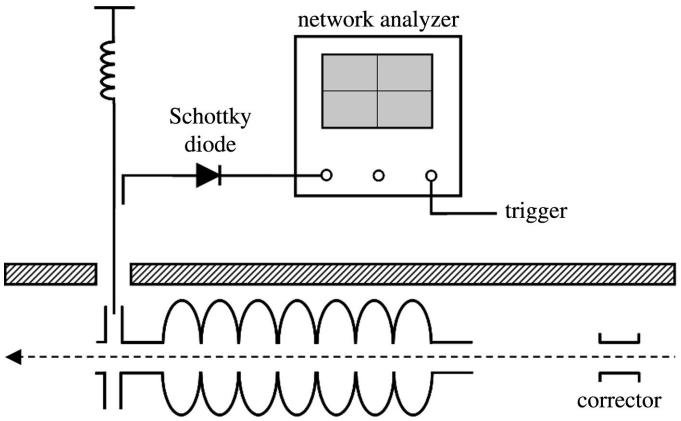

FIG. 4.7: Schematic of the experimental setup used to measure dipole HOM polarizations.

of a chosen HOM. A schematic of the setup is given in Fig. 4.7. To ensure that only the voltage of the chosen HOM was measured, the intermediate frequency (IF) bandwidth of the NWA was limited to 30 kHz. Note that only the input of the NWA was used to measure the signal while the output was terminated. Therefore, a spectrum analyzer could be used for this measurement as well. This process was repeated for eight of the most dangerous HOMs in zone 3, taking care to measure each pair of the dipole modes.

Assume that initially the electron beam travels along the axis of the cavity and does not excite the dipole HOM. The position of the beam can be described by the vector

$$\vec{r} = (x_o, y_o) \tag{4.49}$$

while the polarization of the HOM of interest is described by the unit vector

$$\hat{e}_{HOM} = (\cos\alpha, \sin\alpha) \tag{4.50}$$

where α is the measured angle with respect to the horizontal plane. The induced voltage for a dipole HOM is proportional to the displacement of the electron bunch.

The projection of the beam displacement on the HOM is given by the dot product of Eq. (4.49) with Eq. (4.50)

$$V \propto \vec{r} \cdot \hat{e}_{HOM} = x_o \cos\alpha + y_o \sin\alpha \tag{4.51}$$

As described above, the method of measuring the polarization requires varying the horizontal displacement of the electron beam while measuring the response of the induced HOM voltage

$$\Delta V_x \propto \Delta x \cos\alpha + y_o \sin\alpha \tag{4.52}$$

and then varying the vertical beam displacement while measuring the response

$$\Delta V_y \propto x_o \cos\alpha + \Delta y \sin\alpha \tag{4.53}$$

Because the beam is initially on-axis, (x_o, y_o), and cannot couple to the dipole HOM, by taking the ratio of Eq. (4.53) with Eq. (4.52), the polarization can be calculated using the following relation

$$\alpha = \tan^{-1}\left(\frac{\Delta V_y}{\Delta V_x}\right) \tag{4.54}$$

where ΔV_y and ΔV_x are extracted from fits of the measured data.

An example of measured data is displayed in Fig. 4.8 which shows the results for a mode in cavity 7 with a frequency of 2106.007 MHz. From just an inspection of the HOM response, it is clear that this mode is polarized nearly vertically. A more thorough analysis where ΔV_y and ΔV_x were extracted and Eq. (4.54) used, yielded a polarization of $(88 \pm 2)^\circ$. A summary of the measurements for all the HOMs is given in Table 4.1. Within each dipole HOM, the two polarizations are separated in frequency by a few hundred kHz, making it possible to excite each independently. In addition, one polarization typically has a loaded Q an order of magnitude larger

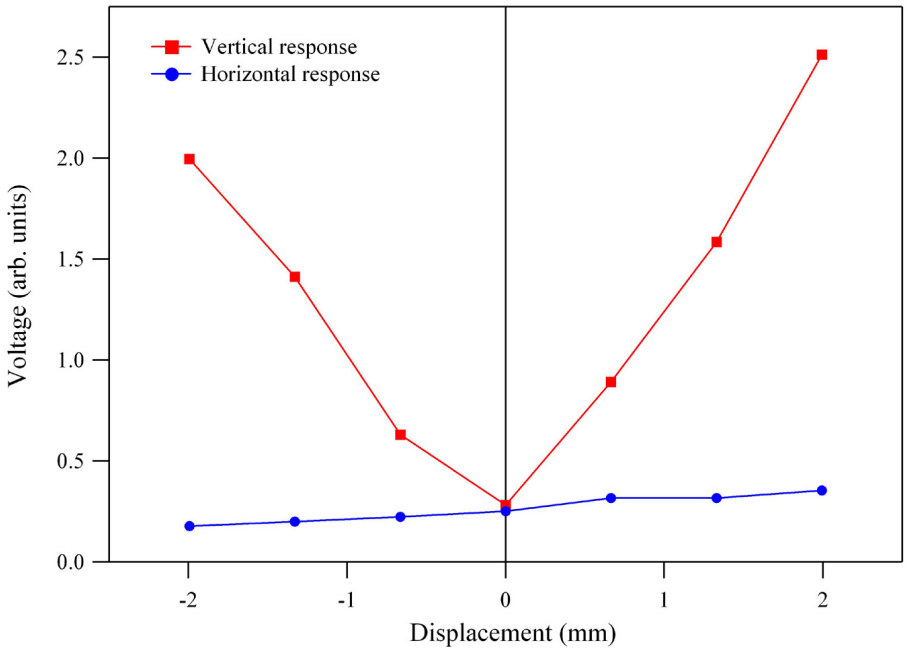

FIG. 4.8: Measured response of the 2106 MHz HOM due to vertical (red) and horizontal (blue) displacements through cavity 7.

than its partner. It was found that these high Q modes are oriented approximately vertically, thereby making BBU less of threat in the horizontal plane (see Table 4.1).

Comparison with Simulation Results

The results of the polarization measurements, specifically the orientation of the 2106 MHz mode, was confirmed through computer simulations. Using the code Omega3P, the Advanced Computations Department at SLAC performed simulations of the Jefferson Laboratory 7-cell cavity. Among the information extracted from the simulations was the polarization of the 2106 MHz mode. The results of the simulated electric field contours for the mode are displayed in Fig. 4.9 which shows that the dipole HOM is split into horizontally and vertically polarized modes [74]. Because the vertically polarized mode has a higher Q_L, it takes longer to decay and interacts more strongly with the second pass beam, which in turn may lead to BBU.

TABLE 4.1: Experimental measurements of HOM polarizations of dangerous dipole modes in zone 3.

Cavity	Mode	Frequency (MHz)	Q_L (10^6)	Orientation (degrees)
8	TM_{110} $3\pi/7$	2102.591	2.61	84 ± 11
		2103.009	0.21	8 ± 13
	TM_{110} $4\pi/7$	2113.346	3.10	80 ± 2
		2114.154	0.35	11 ± 2
7	TM_{110} $3\pi/7$	2105.999	6.11	88 ± 2
		2106.697	0.33	4 ± 1
	TM_{110} $4\pi/7$	2116.583	6.66	86 ± 10
		2117.225	0.49	4 ± 1
4	TM_{110} $3\pi/7$	2102.537	0.27	25 ± 1
		2102.642	0.63	63 ± 1
	TM_{110} $4\pi/7$	2113.991	0.37	33 ± 1
		2114.151	5.21	87 ± 6
3	TM_{110} $3\pi/7$	2104.201	2.49	38 ± 1
		2104.408	0.29	14 ± 1
	TM_{110} $4\pi/7$	2115.386	2.88	75 ± 1
		2115.683	0.39	18 ± 2

4.7 Validity of Single Mode Threshold Current Formula

The analytical results of Sections 4.2 and 4.4 are very powerful provided they are applied properly. While Eq. (4.21) holds for coupled transverse optics, consider for the moment only decoupled optics ($M_{14} = M_{32} = 0$). The first criterion that must be satisfied is an assumption made in deriving the threshold current formula, namely, that the HOM voltage decay is negligible on the scale of the recirculation time. Furthermore, in any real world accelerator there will be more than one dipole HOM present in the linac, even if the linac consists of only a single cavity. So then, the second criterion for applying Eq. (4.21) to individual modes is that the modes are separated in frequency by at least $\omega/2Q_L$. Modes which are separated less than

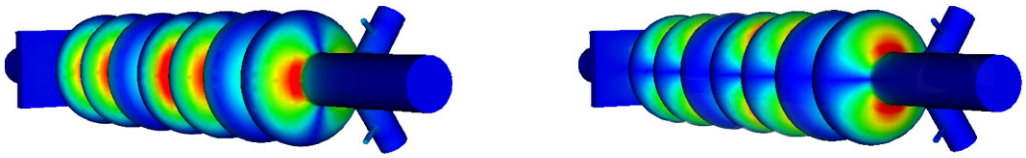

FIG. 4.9: Simulated electric field contours of the 2106 MHz dipole HOM in the 7-cell cavity. The lower Q_L mode causes a horizontal kick (left) while the higher Q_L mode imparts a vertical kick (right). These results are consistent with the experimentally measured mode polarizations.

this will interfere in such a way that the threshold is not determined simply by the threshold current due to the worst individual HOM.

To see this more clearly, consider a single dipole HOM with two polarizations (0° and 90°) where each polarization has the same Q_L and (R/Q). Using the simulation code ERLBBU and by varying the frequency of one of the modes, the effects of frequency separation on the threshold current can be seen. The simulation was repeated for several different values of Q_L. The results are summarized in Fig. 4.10. When $\Delta f > \omega/2Q_L$ the polarizations can be treated independently and the threshold current is given by the lower threshold of the two polarizations. On the other hand, when $\Delta f < \omega/2Q_L$ the coupling between the polarizations plays a significant role and the threshold is not simply the smaller of the threshold current due to each mode treated independently.

Despite its simplicity, the single mode analytic model is applicable for the FEL Upgrade Driver. There are three primary reasons which are based on the results of the RF measurements used to characterize the HOMs. The first is that the bandwidths (f/Q_L) of the dangerous modes, which all lie around 2100 MHz and have loaded Qs of a few 10^6, are several hundred Hz whereas separation between polarizations is $(0.5 - 1.0)$ MHz. Thus, the separation between polarizations is sufficiently large that they can be treated independently. Second, the loaded Qs are an order

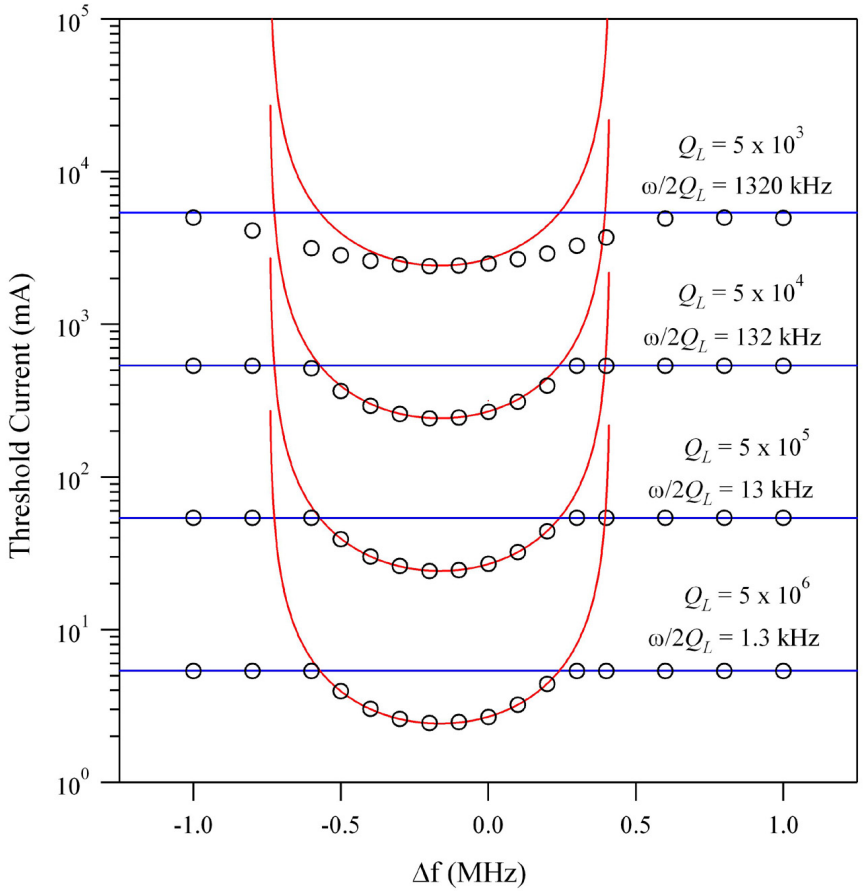

FIG. 4.10: A plot showing the effect of frequency separation between two polarizations of a single dipole HOM on the threshold current. The blue line represents the threshold current for the fixed frequency mode while the red line represents the threshold current for the mode whose frequency is being varied. Both plots were generated using Eq. (4.21). The results of simulations are denoted by open circles.

of magnitude different between polarizations of a given dipole HOM. Consequently only the dominant polarization - which from measurements was determined to be along the vertical axis - needs to be considered. And third, the same modes from cavity to cavity are separated by 100s of kHz up to several MHz. Therefore, because modes are separated in frequency well in excess of $\omega/2Q_L$, they do not destructively interfere and the threshold current is due to the worst individual HOM.

These arguments, however, do not hold true for cases involving transversely coupled optics as will be discussed in Section 6.4.3.

4.8 Results of BBU Simulations

Modeling BBU requires information to fully characterize the HOMs of interest and also an accurate description of the machine optics. An HOM is characterized by its frequency, loaded quality factor, polarization, and R/Q. The first three were measured directly from the cold cryomodule while the R/Q was obtained from MAFIA models [75]. Machine optics describing an 88 MeV beam energy configuration were generated from "all-save" values of the magnet strengths and RF cavity gradients. A feature of each of the three BBU simulation codes is the ability to explicitly define transfer matrices for each accelerating cavity. In this way cavity RF focusing can be included, which is known to have an appreciable effect, particularly at the front end of the linac where the energy of the injected beam is 7 MeV.

4.8.1 FEL Upgrade Without Zone 3

Initial commissioning of the FEL Upgrade Driver proceeded with only zone 2 and zone 4 installed on the beamline. Microwave measurements to characterize the dipole HOMs in each cryomodule - similar to the methods described in Section 4.6.1 - had already been performed [76]. The only difference was the manner in which HOM polarizations were measured. Because the zone 2 and 4 cryomodules are based on the 5-cell cavity design and utilize waveguide HOM couplers, the polarization was measured by noting which mode was perturbed by inserting a probe in the vertical and then the horizontal waveguide.

Simulating the measured modes from the two cryomodules for an 88 MeV machine configuration results in a threshold current of 43.1 mA. The mode responsible for the instability is vertically polarized and located in cavity 6 of zone 2 with a frequency of 1891.120 MHz, an R/Q of 22.1 Ω and a loaded Q of 2.1×10^5. Thus, beam breakup is not a problem for the designed operating current of 10 mA with

these cryomodules. Modes from these two zones which pose the biggest threat for beam breakup have frequencies around 1900 MHz and loaded Qs of a few 10^5. The onset of BBU at currents below 10 mA was precipitated by the installation of the zone 3 cryomodule and is discussed in the following section.

4.8.2 FEL Upgrade With Zone 3

Simulations incorporating the measured modes from zone 3 and for the same 88 MeV setup used in simulations of Section 4.8.1 predict a threshold current of 2.1 mA. The drastic decrease in the threshold current is due to the fact that HOMs in the 7-cell cavities are insufficiently damped, the most dangerous having loaded Qs on the order of 10^6 and are an order of magnitude larger than those in the 5-cell cavities. The simulations were performed with all three of the BBU simulation codes developed at Jefferson Laboratory (TDBBU, MATBBU, ERLBBU) and all predict a threshold current of 2.1 mA. The mode responsible for the instability is vertically polarized and located in cavity 7 of zone 3 with a frequency of 2106.007 MHz, an R/Q of 29.9 Ω and a loaded Q of 6.11×10^6.

The discussion in Section 4.7 explained that the FEL Upgrade Driver is in a regime such that the threshold current of the machine is determined by the threshold current of the worst individual mode. This condition was confirmed through simulations. Initially, a total of 432 individually measured dipole HOMs were simulated. Upon identifying the 2106 MHz mode as the dominant HOM, simulations were repeated using only this mode. In both instances, the predicted threshold current was 2.1 mA.

Simulations performed with MATBBU not only predict the threshold current due to the worst HOM but also the threshold currents due to other HOMs as well. Table 4.8.2 gives the results of the three lowest threshold currents and the corre-

TABLE 4.2: The three lowest threshold currents in the FEL Upgrade as predicted from MATBBU simulations.

Threshold Current (mA)	Frequency (MHz)	Location
2.1	2106.007	zone 3 cavity 7
10.4	2115.201	zone 3 cavity 6
28.1	1937.698	zone 3 cavity 7

sponding HOM frequencies which cause them. Interestingly, with the machine optics used in the simulation, only a single HOM leads to beam breakup below the nominal 10 mA operating current of the FEL Upgrade Driver.

With the predicted threshold current much less than the 10 mA operating current of the Driver, an opportunity exists to benchmark the simulation codes with experimental data. The importance of this task cannot be overemphasized. With the increasing number of proposed ERL-based accelerator applications (see Fig. 2.1), it is crucial that BBU simulation codes can be used with absolute confidence with respect to their results. Because BBU represents such a hard limit on machine performance, effectively setting an upper limit on the average current, a clear and careful understanding of the instability's impact on the machine is required. Benchmarking the codes also serves a more fundamental purpose in that it validates the analytic model of BBU. The topic of benchmarking the codes is the subject of Chapter 5.

CHAPTER 5

Experimental Measurements of Multipass BBU

In May of 2004 BBU was observed in the FEL Upgrade Driver and represents the first time the instability has been observed in an energy recovering linac. Prior to 2004, BBU had been observed in the microtron at Illinois and the recirculating linac at Stanford, both in 1977.

Consequently, the FEL Upgrade Driver has become an ideal testbed for gaining a quantitative understanding of beam breakup, which in turn, has allowed BBU simulation codes to be benchmarked with experimental data, and is the subject of this chapter. The Driver has also proved to be valuable for testing the efficacy of a number of BBU suppression techniques which are discussed in Chapter 6 and Chapter 7.

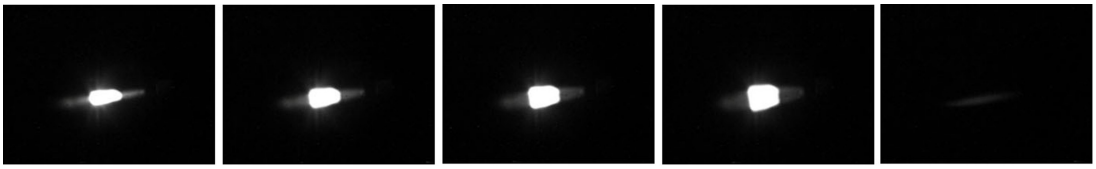

FIG. 5.1: Successive frames in time (progressing from left to right) from a movie of the synchrotron light monitor in the second endloop at the onset of BBU.

5.1 Overview

While the remainder of this chapter is dedicated to describing the details of the quantitative measurements, Fig. 5.1 illustrates a qualitative characterization of BBU. Figure 5.1 shows a series of frames from a recording of a synchrotron light monitor located in the second recirculation arc of the FEL Driver. During the recording, the average beam current was being slowly increased until beam breakup developed. The instability clearly manifests itself as vertical growth which continues until beam losses become large enough to trip the machine off. The time elapsed from the first to the last frame of Fig. 5.1 is approximately 0.25 s.

From the point of view of a machine operator in the control room, the only indication that the operating current is approaching the threshold current are observations of the SLM image growing as depicted in Fig. 5.1. Additional characteristics of the presence of BBU - from an operator's perspective - are single, hard machine trips at one particular beam loss monitor (BLM) location. In most instances, these BLM trips occurred in the 5F region of the Driver where the recirculated beam is re-injected through the linac and the beam envelopes are largest.

Clearly a more quantitative method is needed to confirm that a machine trip is due to BBU. Additional measurements are required to ascertain which cavity contains the dangerous HOM and to determine the frequency of the mode. Furthermore, adequately benchmarking BBU codes requires accurately measuring the

threshold current - preferably with several different methods for consistency. All these measurements require the ability to measure one of the signatures of BBU, namely the HOM power.

5.2 HOM Power

Measuring the HOM power proved to be ideal in regards to studying BBU and was achieved using Schottky diodes [77]. Several attempts to measure the response of BPM striplines, to see the exponentially growing displacement due to the instability, were unsuccessful. Ultimately, the HOM power is easier to monitor and provides a signal that is robust enough to make a number of independent measurements as discussed in Sections 5.4.3 and 5.4.4.

The key element in all these measurements is the fact that the cavities in the zone 3 cryomodule, unlike previous CEBAF 5-cell cavities, use DESY-like coaxial HOM couplers [75]. Cables connected to the HOM ports are loaded on 50 Ω resistors. In order to monitor the HOM power a small portion of the signal from each HOM port is directed to a Schottky diode by a -20 dB directional coupler. The output of each diode is connected to a separate oscilloscope channel. This allows the HOM power to be individually monitored from each of the 8 cavities. The Schottky diode assembly is shown in Fig. 5.2.

5.2.1 Schottky Diodes

A Schottky diode acts as a rectifier, converting an AC waveform to a DC waveform. Schottky diodes have the added advantage over conventional PN junction diodes in that they work well at high frequency. The diodes used for BBU studies were manufactured by Herotek (model DZM124NB) and work across a frequency range from 10 MHz to 12.4 GHz [78].

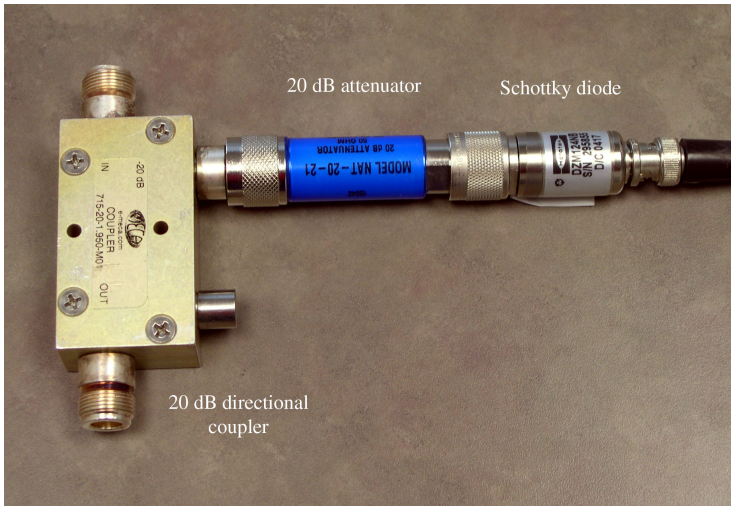

FIG. 5.2: The Schottky diode assembly showing the directional coupler, attenuator and Schottky diode.

Each of the 16 Schottky diodes were calibrated by measuring the output voltage as a function of incident power using an RF signal generator at a frequency of 2000 MHz (the HOM signals of primary interest are around 2100 MHz, however the signal generator did not extend that far in frequency). The resulting data was fit with a polynomial up to second order in the voltage.

5.2.2 Observations of BBU

A thorough experimental investigation of BBU commenced in early 2005. The nominal machine setup for the extent of the study was an 88 MeV configuration with decoupled transverse optics. The injector was set to provide 7.3 MeV electrons into the linac where the accelerating gradients were set such that zone 2, zone 3 and zone 4 provided 28.7 MeV, 15.1 MeV and 36.3 MeV of energy gain, respectively.

Operating in cw mode, the average beam current was slowly increased until exponential growth of the HOM power was observed from cavity 7, which occurred simultaneously with a machine trip caused by excessive beam losses. These trips

occurred at approximately 2 mA of average beam current. The process of slowly ramping up the current was repeated several times to ensure that the instability developed at the same current each time. With the FEL Upgrade Driver in a configuration to readily observe beam breakup, the mode causing the instability was identified (Section 5.3) and measurements of the threshold current were conducted (Section 5.4) to benchmark BBU simulation codes.

5.3 HOM Voltage

Upon identifying cavity 7 as containing the unstable mode, the next measurement was identifying the frequency of the mode. To do this, the signals from the HOM coupler are split further after the -20 dB directional coupler, with one part connected to a Schottky diode to measure the power while the other part is sent directly to an oscilloscope to measure the voltage. A schematic of this setup is shown in Fig. 5.3. If the oscilloscope is fast enough and the signal sufficiently sampled, the frequency of the offending mode can be extracted by Fourier analysis. A screen shot of the oscilloscope screen showing the HOM power and voltage during BBU is given in Fig. 5.4. Taking the FFT of the voltage signal reveals that the mode frequency is 2106.007 MHz (see Fig. 5.5).

The results of the measurements show that with nominal, decoupled optics for an 88 MeV machine configuration, the most dangerous mode is at a frequency of 2106.007 MHz and located in cavity 7. This is in agreement with simulation results presented in Section 4.8.2. The 2106 MHz mode was considered one of the prime candidates for causing BBU because it has the second highest impedance, $(R/Q)Q_L$, of the 224 modes measured in zone 3. In fact, the highest impedance mode is also in cavity 7, at a frequency of 2116 MHz. However subsequent measurements, described in Section 5.4.3, confirmed that this HOM was not a threat for causing BBU because

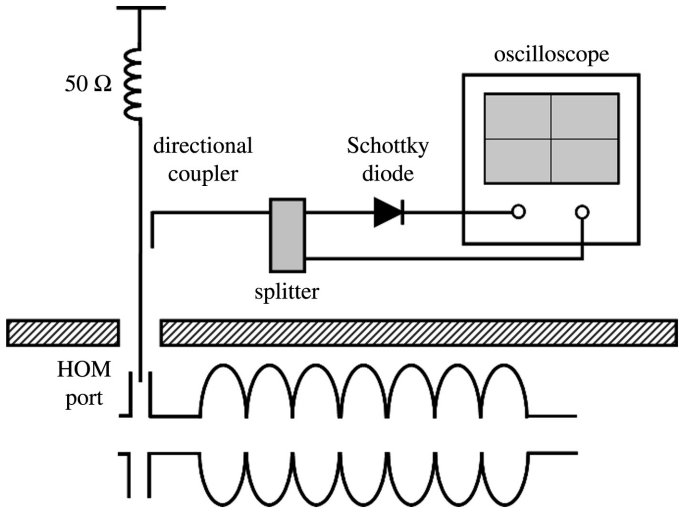

FIG. 5.3: Schematic of the experimental setup for simultaneously measuring the HOM power and voltage from a particular cavity.

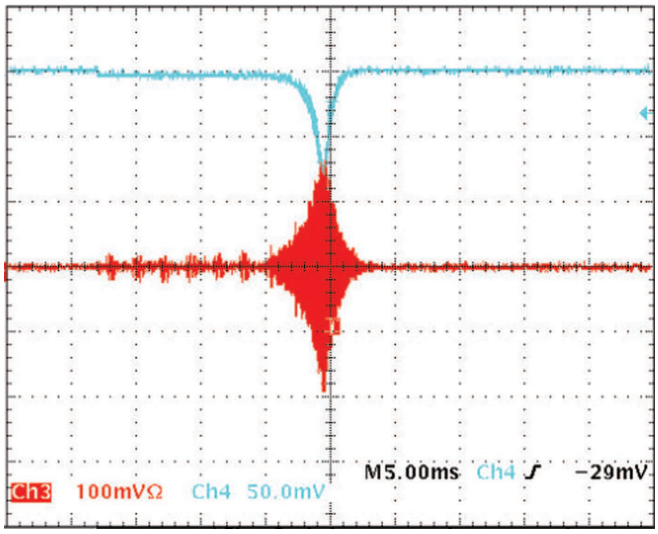

FIG. 5.4: A screen shot of an oscilloscope showing the HOM voltage (red) and power (blue) of the 2106.007 MHz HOM in cavity 7 of zone 3 during BBU.

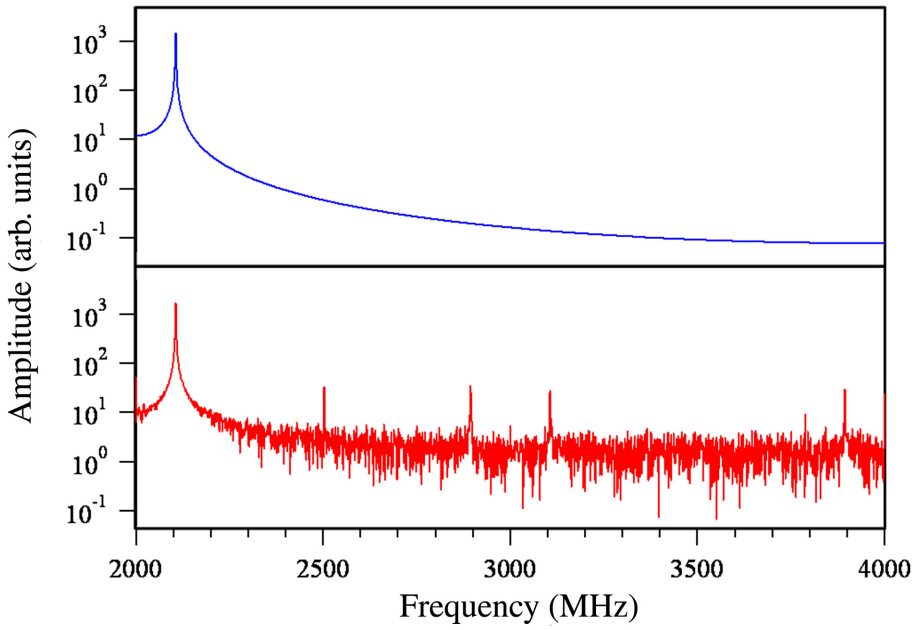

FIG. 5.5: FFT of a pure 2106.007 MHz signal (top) and FFT of the HOM voltage from cavity 7 during BBU (bottom).

$M^* \sin(\omega T_r) > 0$ for the mode.

For thoroughness, note that the experimental results presented thus far represent work done in early 2005 and constitutes the most thorough investigation of BBU. However, initial (and incomplete) BBU studies were also performed in mid-2004. During that period, using the aforementioned methods, BBU was found to occur due to the 2114.156 MHz mode located in cavity 4 of zone 3 [28]. Measurements made in 2005 show that this mode is stabilized with the present configuration making it clear that the beam optics had changed in the interim.

5.3.1 Stable Modes Being Driven Unstable

During the onset of beam breakup due to 2106 MHz, the Schottky diodes connected to cavities 3 and 8 also detected a growth of the HOM power. Measuring the

voltages from these cavities and taking the FFT of the signals yielded the frequencies 1786.206 MHz and 1881.481 MHz for cavities 3 and 8, respectively. According to the results of earlier HOM measurements, these two modes have relatively low impedances and simulations predict that the threshold current due to these modes is at least an order of magnitude higher than that of the 2106 MHz mode in cavity 7. From analyzing the data, it was discovered that the Schottky diode signals from cavities 3 and 8 had nearly the same growth rate as the signal from cavity 7. This suggested that the other modes are being driven by the 2106 MHz mode after it goes unstable.

At the onset of BBU, the transverse beam displacement is deflected at the frequency of 2106.007 MHz. This frequency is aliased to sideband frequencies which, for a bunch repetition frequency of 37.425 MHz, appear at $\pm$10.207 MHz around the beam harmonics. As the instability grows the sidebands become sufficiently strong to the point that they are able to resonantly excite modes which lie at the sideband frequencies. To within several kilohertz (the error in the measurement of the frequencies), the 1786.206 MHz mode corresponds to the lower sideband frequency of the 48^{th} beam harmonic (48 $\times$ 37.425 MHz - 10.207 MHz) while the 1881.481 MHz mode corresponds to the upper sideband frequency of the 50^{th} beam harmonic (50 $\times$ 37.425 MHz + 10.207 MHz). This effect is illustrated in Fig. 5.6. Note that the 1786 MHz and 1881 MHz modes themselves are not unstable, but rather they are driven unstable by the 2106 MHz mode. This phenomenon of sidebands driving otherwise stable HOMs unstable was verified through simulations.

Verification by Simulations

Consider a bunch repetition frequency of 1497 MHz so that the sidebands produced when the 2106 MHz mode becomes unstable do not lie at the frequencies of 1786.206 MHz and 1881.481 MHz. Also consider a bunch frequency of 37.425 MHz

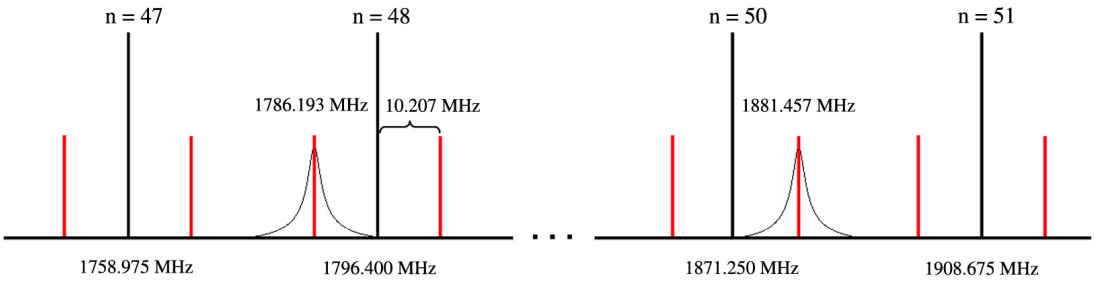

FIG. 5.6: Illustration to show the effect of sideband frequencies driving otherwise stable modes unstable.

for which, as previously mentioned, the sidebands produced by the 2106 MHz mode lie exactly at 1786.206 MHz and 1881.481 MHz.

Figure 5.7 shows a plot of the HOM voltage squared of four modes in zone 3. The simulation was performed with an average beam current that exceeds the threshold current. Therefore the voltage corresponding to the 2106 MHz mode grows rapidly. The other modes plotted correspond to 1786 MHz, 1881 MHz and 2114 MHz (which is pseudo-stable because $M^* \sin(\omega T_r) > 0$). While they exhibit growth, the magnitude of their voltages are 14, 12 and 9 orders of magnitude, respectively, less than that of the 2106 MHz mode after 15 ms.

Figure 5.8 shows the results of repeating the simulation while changing only the bunch frequency from 1497 MHz to 37.425 MHz. Modes that correspond to the sideband frequencies generated by the 2106 MHz mode are now resonantly driven. After 15 ms, the magnitude of the voltages for the 1786 MHz and 1881 MHz modes are now only 5 and 3 orders of magnitude, respectively, less than that of the 2106 MHz mode while the magnitude of the voltage for the 2114 MHz mode remains nearly 9 orders of magnitude less than that of 2106 MHz. Thus only HOM frequencies that correspond to these sideband frequencies are affected.

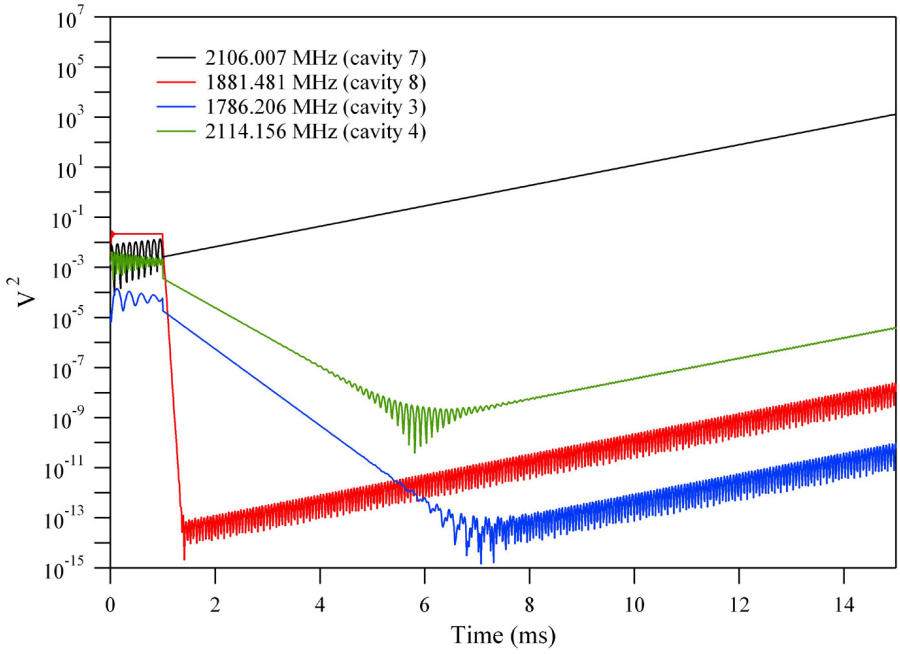

FIG. 5.7: The output from simulations of the HOM voltage squared for 4 modes. The bunch repetition frequency is 1497 MHz and the sidebands generated by 2106 MHz do not drive the other modes.

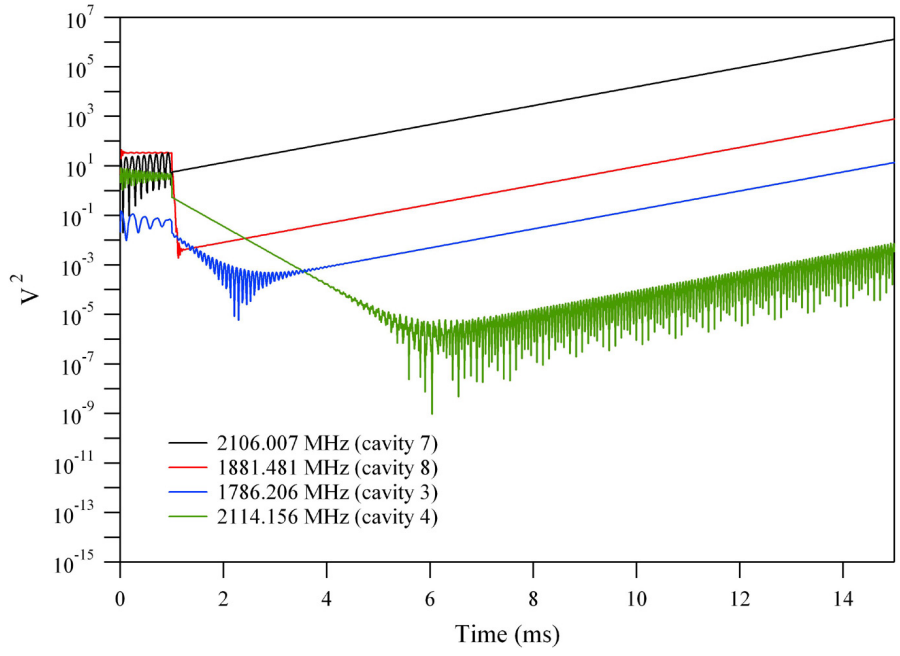

FIG. 5.8: The output from simulations of the HOM voltage squared for 4 modes. The bunch repetition frequency is 37.425 MHz and the sidebands generated by 2106 MHz resonantly drive the 1881 MHz and 1786 MHz modes.

5.4 Measuring the Threshold Current

Given a description of the machine optics and HOM parameters (frequency, Q_L, (R/Q) and polarization) BBU simulation codes calculate a threshold current for beam stability. Hence the easiest way to benchmark the codes is to compare this threshold current with experimental measurements. Three different methods were utilized to measure the threshold current for a particular machine configuration.

The first, if the threshold current was sufficiently small, was by direct observation. That is, simply noting the average current from a beam current monitor at which a BBU-induced machine trip occurs. The remaining two methods make use of an important aspect of BBU, namely, how the HOM voltage behaves above and below the threshold current [65].

5.4.1 Evolution of the HOM Voltage

The evolution of the HOM voltage can be derived in the following manner; using Eqs. (4.23) and (4.24), rewrite the stored energy in terms of the accelerating voltage as

$$U = \frac{V_a^2}{\omega a^2 \left(\frac{\omega}{c}\right)^2 \left(\frac{R}{Q}\right)} \tag{5.1}$$

Writing Eq. (4.18) in terms of Eq. (5.1) yields,

$$\frac{dU}{dt} = -U\left(1 - \frac{I_o}{I_{th}}\right)\left(\frac{\omega}{Q_L}\right) \tag{5.2}$$

and rearranging terms gives

$$\frac{dU}{U} = -\left(1 - \frac{I_o}{I_{th}}\right)\left(\frac{\omega}{Q_L}\right) dt \tag{5.3}$$

which can easily be solved for the stored energy

$$U(t) = U_o \exp\left(-\frac{\omega t}{Q_L}\frac{I_{th} - I_o}{I_{th}}\right) \tag{5.4}$$

It follows that the voltage, which is proportional to the square root of the stored energy, is given by

$$V(t) = V_o \exp\left(-\frac{\omega t}{2Q_L}\frac{I_{th} - I_o}{I_{th}}\right) \tag{5.5}$$

From Eq. (5.5) one can extract an exceedingly useful quantity, defined as the effective quality factor

$$Q_{\text{eff}} = \left(\frac{I_{th}}{I_{th} - I_o}\right) Q_L \tag{5.6}$$

This simple relation states that by measuring the effective Q as a function of the average beam current, in principle, the threshold is easily extracted. With zero beam current, the effective Q is the Q_L of the HOM. When $I_o = I_{th}$, the effective Q becomes infinite and the HOM voltage does not decay. If the beam current exceeds the threshold, the amplitude of the voltage oscillations grow exponentially, and is measured by the Schottky diodes (see Fig. 5.4). Note that Eq. (5.6) is valid both above and below the threshold current.

The beam-transfer function (BTF) measurement is the second method used to measure the threshold current and amounts to using a network analyzer to make an S_{21} measurement of a particular mode as a function of average beam current. By measuring the effective Q, that is, the quality factor of the combined HOM-beam system measured from the -3 dB points of the frequency curve, as a function of current, Eq. (5.6) can be used to extract the threshold current.

The third and final measure of the threshold is achieved by measuring the growth rate of the HOM power. The growth rate is described by the time constant

for the HOM-beam system and is derived using Eq. (5.6) and the fact that $\tau = Q/\omega$, giving

$$\tau_{\text{eff}} = \left(\frac{I_{th}}{I_{th} - I_o} \right) \tau_o \tag{5.7}$$

where τ_o is the natural decay time of the HOM. Similar to the BTF measurement, Eq. (5.7) can be used to extract the threshold current after measuring the effective time constant as a function of average beam current.

The method of measuring the growth rate and the BTF measurement combine to create a complementary set of measurements. Whereas measuring the growth rate is a time-domain measurement made above the threshold current using pulsed beam, the BTF measurement is inherently a frequency-domain measurement made below the threshold current with cw beam.

5.4.2 Direct Observation

Figure 5.9 shows a plot of the beam current monitor signal from the beam dump during the time in which the current was slowly increased until the threshold was reached. At this point the machine trips off due to excessive beam losses and the current goes to zero. The current just prior to the machine tripping represents the threshold current and is 2.3 mA. The machine trip was simultaneously observed with an exponential growth in the HOM power to ensure that the instability, and not other beam loss mechanisms such as poor transmission, was the cause.

5.4.3 Beam Transfer Function

The BTF technique is an exceedingly useful measurement because it allows one to determine the BBU threshold for individual HOMs while doing the measurement below the threshold current. In earlier BBU experiments at the Jefferson Laboratory

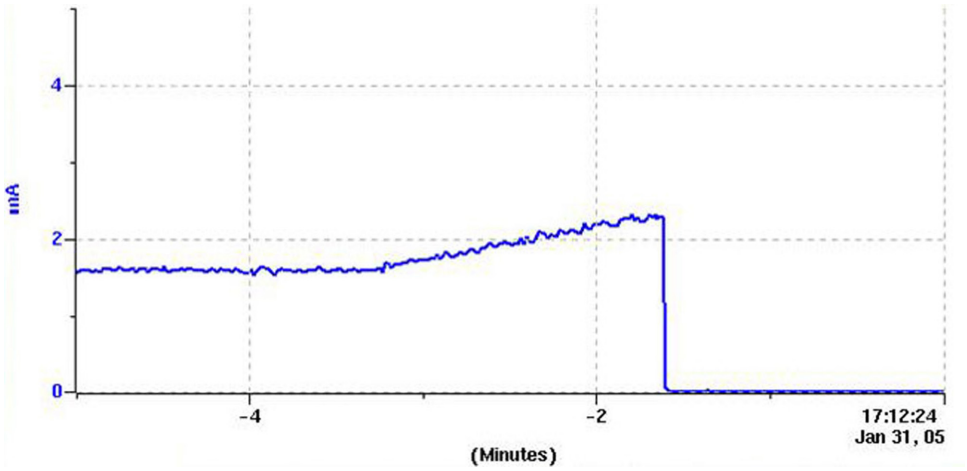

FIG. 5.9: Signal from a beam current monitor at the time of a BBU induced machine trip.

IR FEL Demo (the predecessor to the FEL Upgrade) described in [79], beam oscillations were excited at the injector using a stripline kicker. The cavity response was measured at the frequency of the kicker signal through the cavity probe. The frequency of the signal was swept to measure the transfer function. Dangerous HOMs appeared as resonance peaks in the response signal during the frequency scan. A linear fit of the logarithm of the height of these peaks versus the logarithm of the beam current was used to determine the threshold. However, by measuring the Q of the resonance curve and invoking Eq. (5.6), the analysis is simplified a great deal since $1/Q_{\rm eff}$ is a linear function of the beam current.

Initial BTF measurements using the scheme described above modulated the beam at a frequency of 2106 MHz with a stripline kicker and measured the Q of the mode as a function of average beam current. Plotting $1/Q_{\rm eff}$ versus the current results in the expected linear relationship. At the threshold current the quantity $1/Q_{\rm eff}$ becomes zero. Therefore, the point at which the linear fit intersects the current axis defines the threshold current. For the 2106 MHz mode, this point occurs at (2.3 ± 0.1) mA in agreement with direct observation.

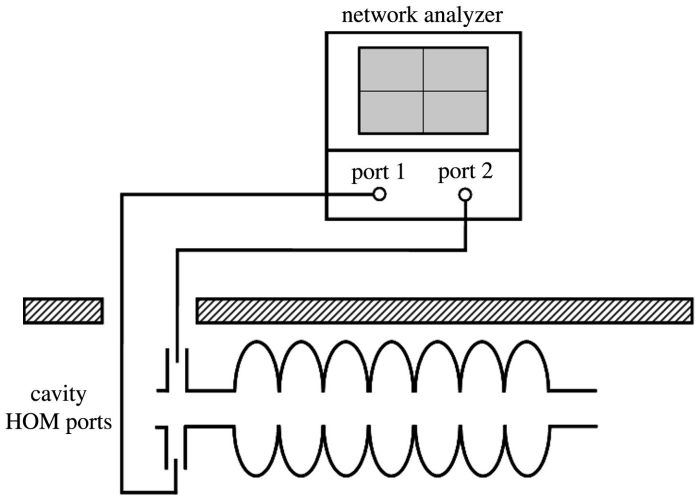

FIG. 5.10: Schematic of the experimental setup used for the cavity-based beam transfer function measurement.

Because of the accessibility to the HOM ports of the cavities in zone 3, the BTF measurement was simplified substantially by exciting the beam directly through an HOM port of the cavity. The response signal was measured from the other HOM port of the same cavity. A schematic of the setup is shown in Fig. 5.10. This technique had a significantly higher signal-to-noise ratio than the method used previously and eliminated the need for a kicker and a high-power amplifier. And as mentioned, since the quality factor of the HOM resonance was measured as a function of the beam current rather than the height of resonance peaks, analysis of the data was greatly simplified.

With the new cavity-based setup, the BTF of the 2106 MHz mode was repeated. For this mode $M^* \sin(\omega T_r) < 0$, and the height of the resonance peak grows and the quality factor increases with the beam current. The resonance curve data for different values of beam current are shown in Fig. 5.11. The quantity $1/Q_{\rm eff}$ is a linear function of the beam current and has a negative slope as displayed in Fig. 5.12. Finding the intersection with the horizontal axis, the data yields a threshold current of (2.4 ± 0.1) mA which is in excellent agreement with the results of the kicker-based

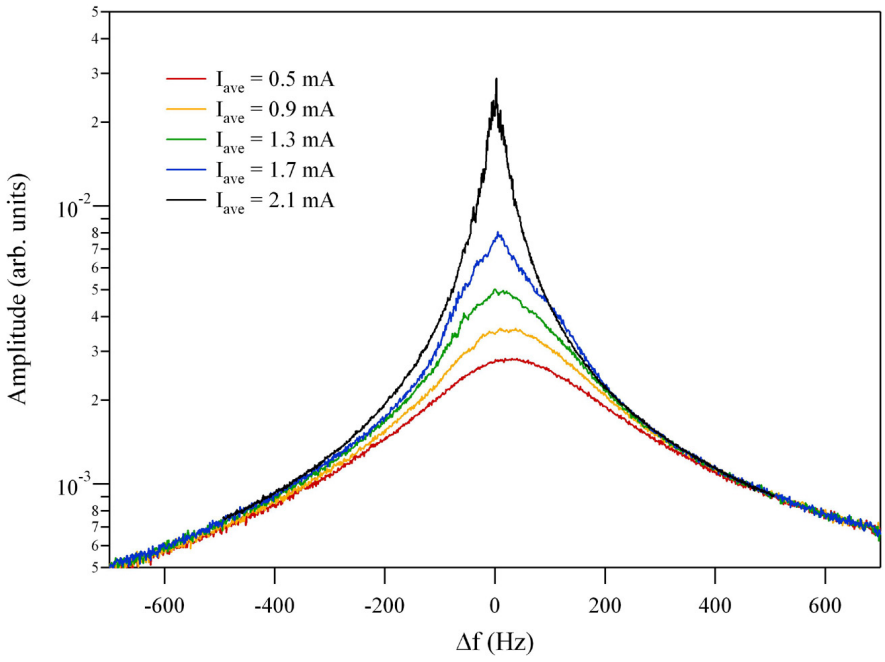

FIG. 5.11: The resonance curve for the 2106 MHz HOM as a function of average beam current with nominal, decoupled optics. Note that the effective Q of the curve increases as the current increases. This indicates the system is unstable.

BTF measurement.

The BTF technique is also useful in establishing whether a mode is in the pseudo-stable regime or is unstable by determining the sign of the term $M^* \sin(\omega T_r)$ which appears in the denominator of Eq. (4.21). Recall that the formula is applicable only if this term is less than zero. If it is greater than zero, the approximations made in deriving Eq. (4.21) are no longer valid. Studies with BBU simulations show that for cases where $M^* \sin(\omega T_r) > 0$, the instability can still develop, but does so at currents of several Amperes [65]. This is referred to as the pseudo-stable regime, since for all practical purposes a threshold current on the order of an Ampere for the 10 mA FEL Upgrade means the system will be stable. (Note that the situation is different when $\omega T_r / 2Q_L$ is no longer $\ll 1$, as is the case in some large scale ERLs being planned [69]).

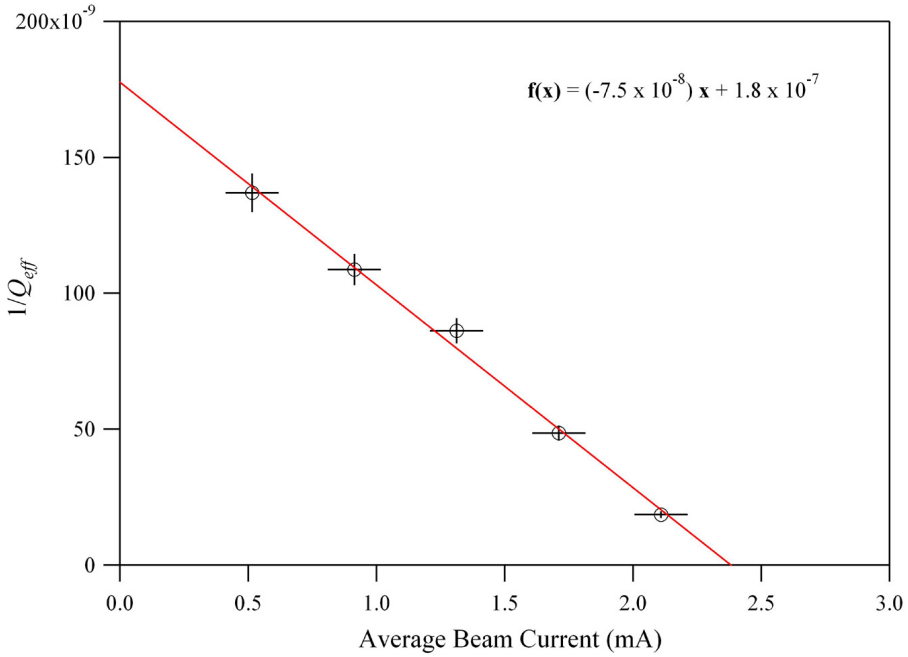

FIG. 5.12: A plot of $1/Q_{\text{eff}}$ versus the average beam current from the data in Fig. 5.11. The intersection of the least squares fit (functional form given on the plot) with the horizontal axis determines the threshold current to be 2.4 mA.

If $M^* \sin(\omega T_r) > 0$, the slope of $1/Q_{\text{eff}}$ changes its sign and becomes positive. In this case, the height of the resonance peak decreases and the quality factor becomes smaller as the beam current increases. This is illustrated in Fig. 5.13 which shows the results of the BTF measurement for the 2114 MHz mode located in cavity 4. The line $1/Q_{\text{eff}}$ crosses the horizontal axis at a negative beam current. Figure 5.14 shows that the fit of the experimental data has a positive slope and crosses the horizontal axis at -8.3 mA, thus indicating the mode is stabilized with this particular optics configuration. (The slight frequency shift (few Hz) of the resonance curve peak - most evident in Fig. 5.13 - results from changes in the mechanical tuner which are initiated by the low level RF system to maintain cavity gradient and phase as the current increases.)

Because the 2116 MHz mode in cavity 7 has the highest impedance of the

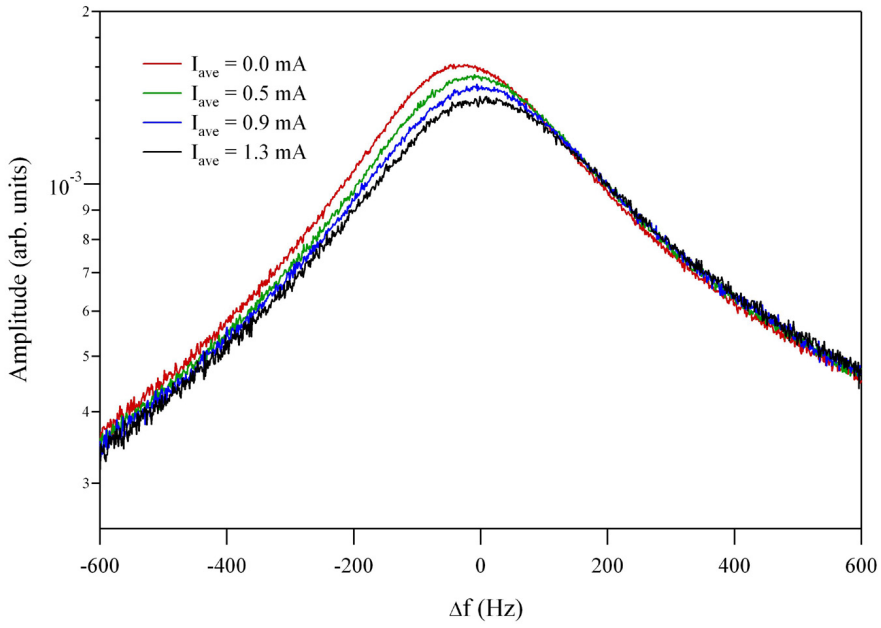

FIG. 5.13: The resonance curve for the 2114 MHz HOM as a function of average beam current with nominal, decoupled optics. Note that the effective Q of the curve decreases as the current increases. This indicates the mode is pseudo-stable.

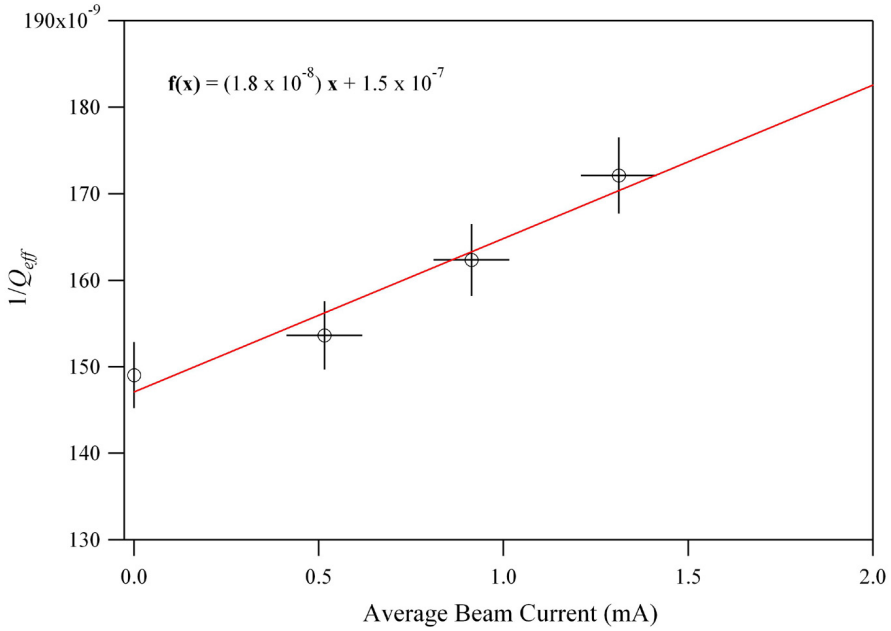

FIG. 5.14: A plot of $1/Q_{\text{eff}}$ versus the average beam current from the data in Fig. 5.13. The least squares fit is used to determine that the mode is pseudo-stable.

measured HOMs in zone 3, a BTF measurement was performed to determine if the mode posed a threat for causing BBU. The results of the measurement show that the mode is stabilized. The reason why 2106 MHz is unstable and 2116 MHz is pseudo-stable can be readily explained from Eq. (4.21). Since the machine optics are decoupled, $M_{32} = M_{14} = 0$. From the measurements discussed in Section 4.6.2, both modes are vertically polarized, $\alpha = 90°$, and M^* reduces to M_{34}. From the 88 MeV machine lattice, the sign of M_{34} from cavity 7 back to itself is negative (for this discussion the magnitude is not important). It follows that for the recirculation time of the FEL Driver, 433.199 ns, that $M_{34}\sin(\omega_{2106}T_r) < 0$ and 2106.007 MHz is unstable, whereas $M_{34}\sin(\omega_{2116}T_r) > 0$ and 2116.585 MHz is in the pseudo-stable regime.

As a historical aside, note that a technique similar to the BTF measurement was used to determine the threshold current at the Stanford SCA during the earliest experimental work on BBU [10, 80]. An external source was used to excite the HOM and the response measured from a different port. Measuring the power radiated without beam and in the presence of beam in the cavity, the threshold current could be calculated [81].

5.4.4 Growth Rate Measurements

With the flexibility in the beam bunching structures allowed by the Driver's injector, it is possible, in addition to observing BBU in cw mode operation, to observe and measure BBU developing within a sufficiently long macropulse in pulsed mode operation. The evolution of the HOM voltage at currents above or below the threshold current is described by Eq. (5.7). This voltage behavior is illustrated in Fig. 5.15 where the cavity voltage as measured through a Schottky diode is plotted against time for two 9 ms long macropulses of differing currents. The exponential

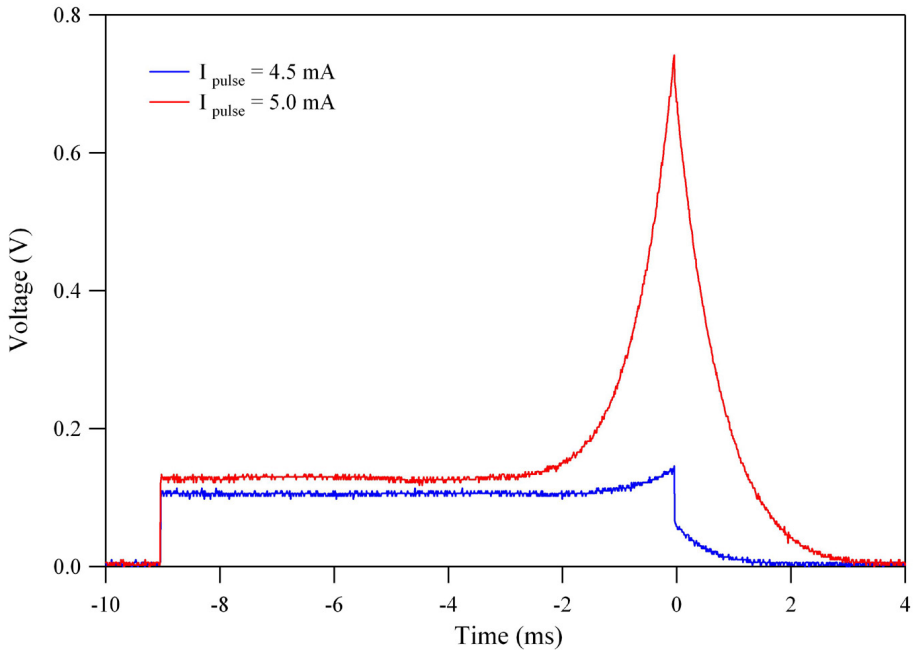

FIG. 5.15: The HOM voltage measured from an unstable cavity for 9 ms long macropulses with 4.5 mA of average current (blue) and 5.0 mA of average current (red).

growth represents the effective time constant of the HOM-beam system. With the end of the macropulse, the exponential decay represents the natural damping time of the HOM causing the instability. The relationship between the two time constants is dependent on the average macropulse current at the time of the measurement and the threshold current.

The data in Fig. 5.16 illustrate the effect of keeping the macropulse current constant and changing the macropulse length.

Note that in Figs. 5.15 and 5.16 a "pedestal" appears on the HOM voltage plots. This is most likely generated by the beam directly inducing a voltage on the HOM coupler probes, which extend several millimeters into the beam tube. Essentially they are acting like button pickups commonly found in BPMs.

Growth rate measurements were performed by measuring the HOM power from cavity 7 while operating the beam in pulsed mode. The macropulse length was

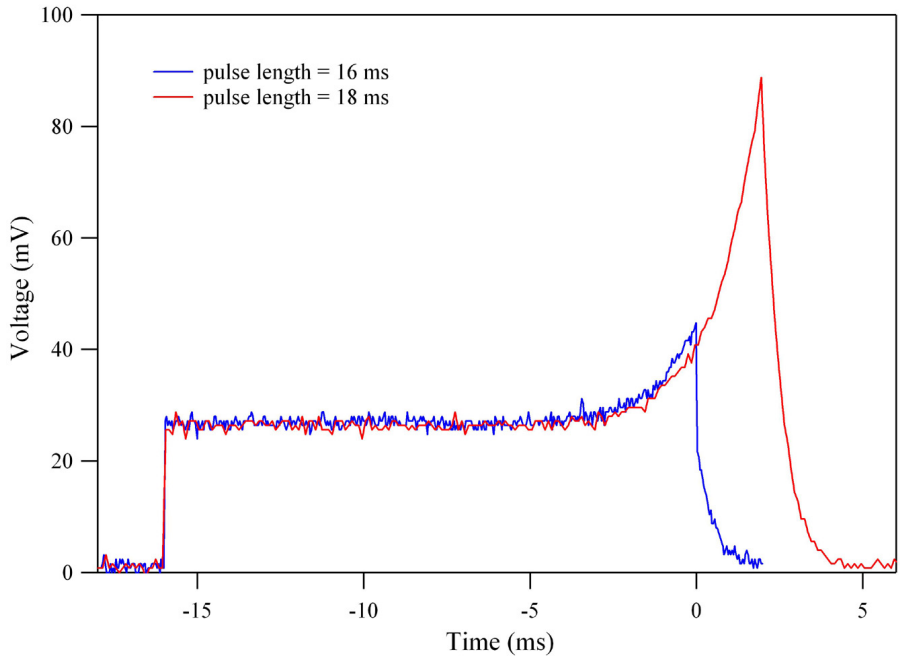

FIG. 5.16: HOM voltage measured from an unstable cavity for 16 ms (blue) and 18 ms (red) long macropulses with an average current of 3.5 mA.

chosen to be sufficiently long and the current to be sufficiently large such that BBU would develop within the macropulse. By fitting the rise (τ_{eff}) and decay (τ_o) time of the instability, Eq. (5.7) can be used to solve for the threshold current explicitly

$$I_{th} = \left(\frac{\tau_{\text{eff}}}{\tau_{\text{eff}} - \tau_o} \right) I_o \tag{5.8}$$

These measurements were performed with macropulse currents of 3.0 mA, 3.5 mA and 4.1 mA and yielded threshold currents of (2.3 ± 0.2) mA, (2.3 ± 0.1) mA and (2.3 ± 0.1) mA, respectively. Additionally the Q_L of the 2106 MHz mode, extracted from the fit of the decay time, agrees to within 7% of previous RF measurements. Figure 5.17 shows the rise and decay times of the instability for all three macropulse currents plotted on the same graph (note the vertical logarithmic scale). This nicely illustrates both the exponential growth of HOM power during BBU and also how the instability growth time depends on current. Note that the decay times

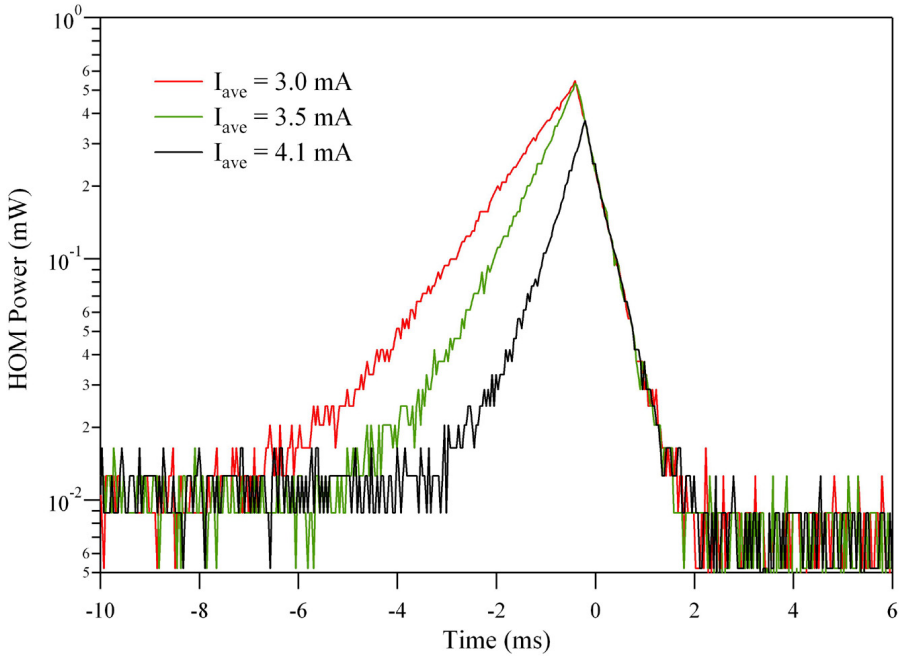

FIG. 5.17: A plot of the HOM power of the 2106 MHz mode as a function of time for three different values of macropulse current (note the logarithmic scale of the vertical axis).

are identical, as they should be, since this represents the natural decay time of the 2106 MHz mode that caused the instability.

An alternate way of extracting the threshold current is to plot the three values of $1/\tau_{\text{eff}}$ against the macropulse current and fit the data with a line in the same way as the BTF measurements. Finding the intersection of the extrapolated linear fit and the current axis indicates that the threshold current is (2.2 ± 0.2) mA as shown in Fig. 5.18.

5.5 Characterizing the Beam Optics

To benchmark the BBU codes, it is important that the beam optics used in the simulations accurately describe the optics of the machine that the measurements were performed on. In principle, standard difference orbit measurements are used

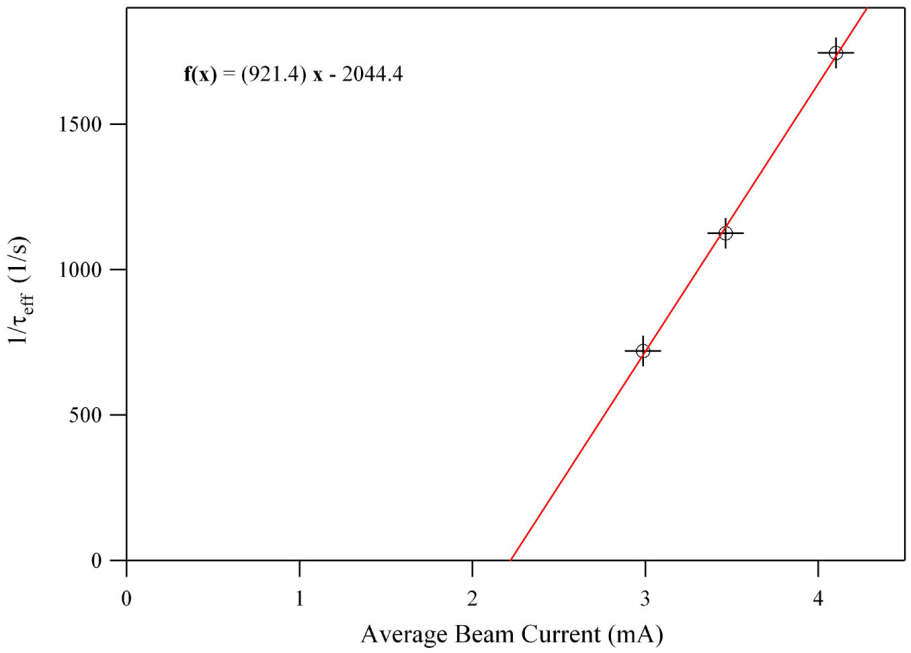

FIG. 5.18: A plot of the three values of $1/\tau_{\text{eff}}$ corresponding to each macropulse current from Fig. 5.17 versus the macropulse current. The threshold current is 2.2 mA and is extracted in the same manner as the BTF measurements.

to experimentally characterize the optics. Correctors immediately downstream of zone 4 are used to provide a known angular kick (horizontal and vertical) while downstream BPMs record the beam position. This is repeated with several corrector pairs. In preparation for these BBU studies, a program to automate the process of collecting the difference orbits was developed. The data is loaded into a machine model and the quadrupole strengths are varied to make the positional data and the positions predicted by the model match. These then are the actual quadrupole strengths in the machine.

In principle this process is straightforward. However, for an ERL without beam position monitors with the capability to resolve two co-propagating beams through the linac, the ability to determine the betatron phase advance (horizontal and vertical) is limited. Furthermore, in the Upgrade Driver the placement of several BPMs

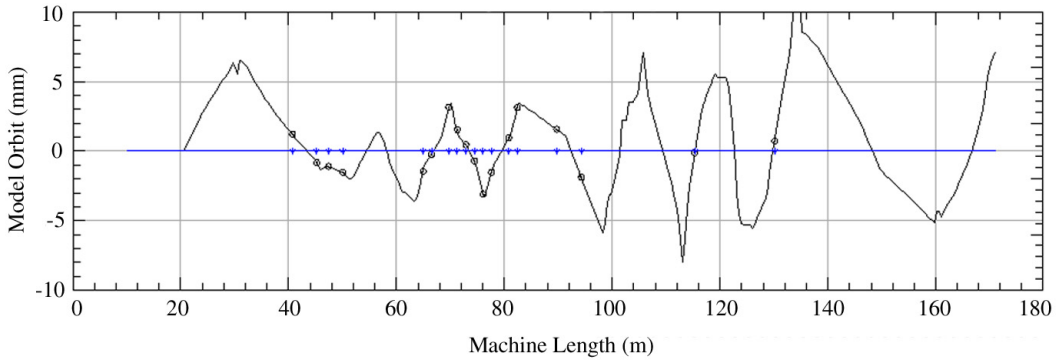

FIG. 5.19: The model optics in response to a horizontal kick immediately following zone 4 (line) and the expected displacements at the BPMs used in the difference orbits (open circles). The latter half of the machine is characterized by only two points, at locations 4F12 and 5F05. Since the optics is transversely decoupled, the vertical response at the BPM locations is zero (blue markers).

in the recirculator is such that they yield no useful data. That is, the betatron phase advance between the correctors used to kick the beam and the BPMs at 4F12 and 5F05 is nearly an integer multiple of π so that the BPMs do not register a displacement - regardless of the strength of the corrector kicks.

The lack of sufficient difference orbit data is illustrated in Fig. 5.19. This plot was generated in the program TAO, developed at Cornell University, which was used to analyze the data [82]. The response to a horizontal kick immediately following zone 4, as predicted by the model optics, is plotted along with the expected displacements at the BPMs used in the difference orbits. While there is adequate BPM data in the first half of the machine, the latter half is characterized by only two points, at 4F12 and 5F05. The net result is that the data is sufficient to resolve only the optics through the first half of the machine. Although less than satisfactory, given the manner in which the machine was instrumented at the time and using the automated difference orbit software, this represents the best that can be done to experimentally characterize the optics.

It should be noted that a brute force method - utilizing beam viewers to measure

the beam's response in regions where the BPMs are ineffective - can be used to reconstruct the machine optics. However, by the time the problem of the insufficient difference orbit data was revealed, the machine configuration had changed to such an extent that characterizing the optics in this manner would be meaningless with regard to the BBU studies.

Fortunately for each machine configuration a record, or "all-save", exists of the quadrupole and dipole strengths, the accelerating gradient for each cavity, the linac phasing, and the injection energy. This represents all the information required to reconstruct the optics in the BBU simulations. While not determined experimentally, this represents a good starting point. The results of simulations based on the all-save data to describe the beam optics are displayed in Table 5.1 and discussed in Section 5.6.

5.6 Summary

A comparison between the predictions from simulations, experimental measurements and analytic calculation of the threshold current is displayed in Table 5.1.

The simulations were performed with the three BBU codes developed at Jefferson Laboratory; TDBBU, MATBBU and ERLBBU as well as a code developed at Cornell University called BI [83]. For consistency all the codes were run with the HOM kicks placed before each accelerating cavity. As expected, the predictions from all four codes agree.

A variety of experimental techniques were utilized to measure the threshold current and they all show excellent agreement amongst themselves. The BTF measurement used cw beam operating at currents below the threshold current, while the growth rate measurements employed pulsed beam operating at currents above the threshold. Thus under a variety of beam conditions (cw and pulsed) and operating

TABLE 5.1: Comparison of simulation predictions, experimental results and the analytic calculation of the threshold current.

	Method	Threshold Current (mA)
Simulation	TDBBU	2.1
	MATBBU	2.1
	ERLBBU	2.1
	BI	2.1
Experimental	Direct Observation	2.3 ± 0.2
	Kicker-based BTF	2.3 ± 0.1
	Cavity-based BTF	2.4 ± 0.1
	Growth Rates	2.3 ± 0.2
	(method 1)	2.3 ± 0.1
		2.3 ± 0.1
	(method 2)	2.2 ± 0.2
Analytic	Analytic Formula	2.1

in different current regimes (above and below the threshold) and working in both the time and frequency domain, there is complete agreement in determining the threshold current.

To emphasize the value of the single mode threshold current derived in Section 4.2, Table 5.1 includes the threshold current as determined by plugging values for the 2106 MHz mode in Eq. (4.21). The analytic formula agrees very well with both simulations and experimental data.

The results summarized in Table 5.1 represent the first time BBU simulation codes have been benchmarked with experimental data. The measured data and the simulation predictions agree to within 10%. As a consequence of benchmarking the codes, the validity of the analytic model used to describe BBU, and the threshold current formula in particular, have been confirmed.

CHAPTER 6

BBU Suppression: Beam Optical Control

6.1 Overview

With the average current limited in the FEL Upgrade Driver to approximately 2 mA, attention is now turned towards implementing suppression techniques. Insights into how the threshold current can be increased are gained by considering the parametric dependence of the threshold as expressed in Eq. (4.21). There exist four primary means by which to increase the threshold current. First, since the threshold is directly proportional to the beam energy, the injection energy must be increased, or the cryomodule with the unstable mode can be placed in the back end of the linac where the energy is higher. Secondly, the ratio (R/Q) which is a property of the cavity's geometry must be lowered. These first two methods are not technically feasible given that the cavities are already fabricated and the cryomodule is installed on the beamline. Thirdly, the properties of the mode itself can be modified by lowering the loaded Q and/or modifying the frequency such that the phase term leads

to a condition where $M^* \sin(\omega T_r) < 0$ and the system is pseudo-stable. Fourth, the machine lattice can be changed, which amounts to modifying the quantity M^* defined in Eq. (4.19). The use of beam optical suppression techniques is the topic of this chapter and methods for modifying the properties of the mode are covered more fully in Chapter 7.

Methods to manipulate the transverse beam optics in order to suppress BBU were first presented in 1980 [84]. The strategy of beam optical control techniques is to modify the machine lattice in such a way that the beam cannot couple as effectively to the dangerous dipole mode. This can be achieved with point-to-point focusing, reflecting the betatron planes about an axis that is at 45° between the vertical and horizontal axes and a 90° rotation. While the ability of point-to-point focusing to increase the threshold current was demonstrated at the SCA [11] and at MUSL-2 [27], the latter two methods, which require introducing strong betatron coupling into the system, had never before been tested experimentally. In 2005, the ability to raise the threshold current by each of these methods was successfully demonstrated in the FEL Driver, and these methods are described in the following sections.

6.2 Point-to-Point Focusing

Because it does not involve complicated transverse coupling schemes, point-to-point focusing was the first beam optical suppression technique employed to combat the effects of BBU in the SCA and at MUSL-2. With a judicious change in the betatron phase advance, point-to-point focusing can be achieved (M_{12} or $M_{34} = 0$) at the location of the cavity containing a dangerous mode so that an HOM-induced kick on the first pass results in a zero displacement on the second pass. In this way the beam cannot transfer energy to the mode by coupling to the electric field

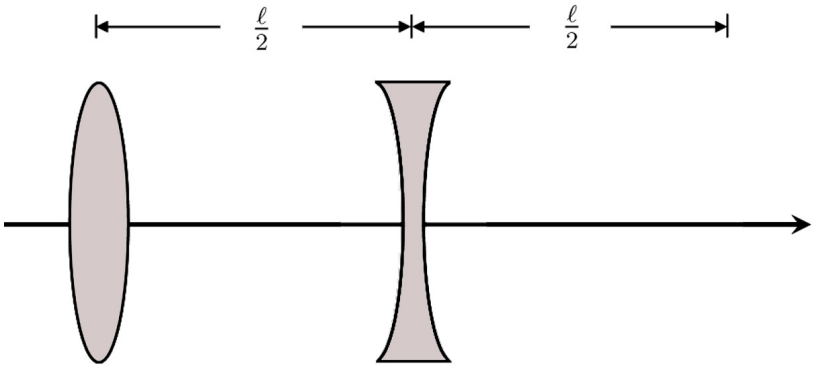

FIG. 6.1: Schematic of a FODO cell of length ℓ.

because it has no on-axis component. In the FEL Driver, point-to-point focusing is achieved by utilizing the properties of the FODO channel in the 3F region of the recirculator.

6.2.1 Implementing Point-to-Point Focusing

Consider the transfer matrix for a FODO cell of length ℓ depicted in Fig. 6.1

$$\begin{pmatrix} 1 & \frac{\ell}{2} \\ 0 & 1 \end{pmatrix} \begin{pmatrix} 1 & 0 \\ \frac{1}{f} & 1 \end{pmatrix} \begin{pmatrix} 1 & \frac{\ell}{2} \\ 0 & 1 \end{pmatrix} \begin{pmatrix} 1 & 0 \\ -\frac{1}{f} & 1 \end{pmatrix} \tag{6.1}$$

Carrying out the matrix multiplication in Eq. (6.1) and equating it with the most general form of a unit matrix using the Twiss parametrization gives [38]

$$\begin{pmatrix} 1 - \frac{\ell}{2f} - \frac{\ell^2}{4f^2} & \ell\left(1 + \frac{\ell}{4f}\right) \\ -\frac{\ell}{2f^2} & 1 + \frac{\ell}{2f} \end{pmatrix} = \begin{pmatrix} \cos\Delta\psi + \alpha\sin\Delta\psi & \beta\sin\Delta\psi \\ -\gamma\sin\Delta\psi & \cos\Delta\psi - \alpha\sin\Delta\psi \end{pmatrix} \tag{6.2}$$

Equating the trace of each matrix leads to

$$1 - \frac{\ell^2}{8f^2} = \cos\Delta\psi = 1 - 2\sin^2\frac{\Delta\psi}{2} \tag{6.3}$$

from which the phase advance across the cell can be computed via

$$\sin\frac{\Delta\psi}{2} = \pm\frac{\ell}{4f} \tag{6.4}$$

The beta functions at the focusing and defocusing quadrupoles can be obtained in a similar manner, giving

$$\beta_F = \frac{\ell(1+\sin\frac{\Delta\psi}{2})}{\sin\Delta\psi} \tag{6.5}$$

$$\beta_D = \frac{\ell(1-\sin\frac{\Delta\psi}{2})}{\sin\Delta\psi} \tag{6.6}$$

where the subscripts F and D denote the location of the focusing and defocusing quadrupole, respectively. For a FODO cell in the 3F region of the FEL Upgrade Driver, $\ell = 3.11$ m, $1/f = 0.91$ m^{-1} and Eq. (6.4) gives $\Delta\psi = \pm 90$ degrees. Plugging the appropriate values into Eqs. (6.5) and (6.6) results in a beta function of 5.3 m at the focusing quadrupole and 0.9 m at the defocusing quadrupole.

The goal in achieving point-to-point focusing is to generate a sufficient change in the betatron phase advance while minimally affecting the beam envelopes. To that end, consider a set of focusing perturbations at locations k each with focal length f_k. At a downstream observation point, denoted by o, the perturbations will generate deviations in the beta function and betatron phase advance according to

$$\left(\frac{\delta\beta}{\beta_o}\right)_n = \mp\sum_{k=1}^{N}\frac{\beta_k^n}{f_k}\sin(2\Delta\psi) \tag{6.7}$$

$$\delta\psi_n = \pm\frac{1}{2\pi}\sum_{k=1}^{N}\frac{\beta_k^n}{f_k}\sin^2\Delta\psi \tag{6.8}$$

where $\delta\beta$ is the deviation in the beta function, $\delta\psi$ is the deviation in the phase advance and where n denotes the horizontal (upper sign) or vertical (lower sign)

plane [85]. Equations (6.7) and (6.8) indicate that for a periodic FODO channel with 90° phase advance per cell, if focusing perturbations are applied uniformly over an integral number of betatron wavelengths, the betatron phases can be varied independently of the beam envelopes [86]. Furthermore, because the beta functions are large in the focusing plane of the quadrupoles, changing the strengths of vertically focusing quadrupoles produces a significant shift in vertical phase advance but only a modest shift in the horizontal (the reverse is true if changes are applied to the horizontally focusing quadrupoles).

6.2.2 Measured Effect on the Threshold Current

The dangerous 2106 MHz HOM is vertically polarized and a change in the vertical phase advance is required. This change is achieved by changing the strengths of four vertically focusing quadrupoles (3F01, 3F03, 3F05, 3F07) from their nominal setpoint in steps of 100 G from −200 G to +300 G.

For each change in the quadrupole strengths the threshold current was measured either by direct observation (if the threshold current was sufficiently small) or by the BTF measurement. The effect of changing the phase advance is illustrated in Fig. 6.2 where the threshold current is plotted against the change in quadrupole strength. The results are quite dramatic; the threshold went from being less than 1 mA (−200 G) to the mode being stabilized (+300 G). In fact, with the mode stabilized, a high average current run was attempted. The machine was eventually limited to 6 mA (due to dangerously high pressure spikes in the injector) with no indications of BBU.

The threshold current in Fig. 6.2 exhibits a dependence which is explained by the fact that the M_{34} element of the recirculation matrix is proportional to $\sin \Delta\psi$ where $\Delta\psi$ is the betatron phase advance for a single recirculation from the cavity

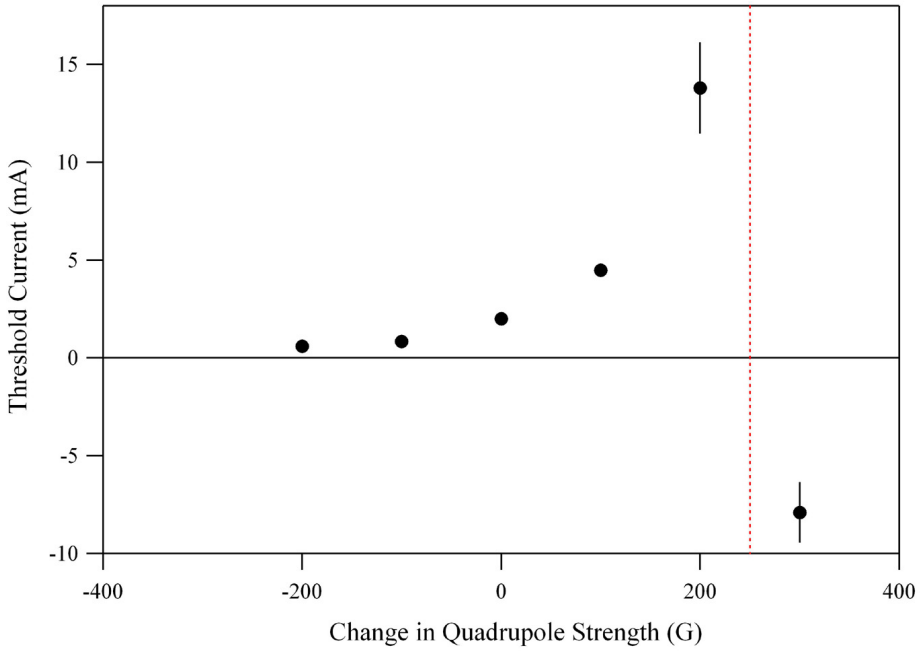

FIG. 6.2: A plot of the threshold current versus the change in quadrupole strength showing the effect of point-to-point focusing. At approximately 250 G the change in phase advance makes the M_{34} element of the recirculation matrix from the cavity back to itself equal to zero before changing sign and leading to a negative threshold current.

back to itself. For a quadrupole strength of approximately 250 G the phase advance from cavity 7 back to itself is equal to $n\pi$, where n is an integer. Therefore M_{34} can be expressed as

$$M_{34} \propto \sin(\Delta\psi) = \sin(n\pi + \delta) = (-1)^n \delta \tag{6.9}$$

where δ is the variation of the phase advance from $n\pi$. It follows that for small variations, δ is proportional to the change of the quadrupole strength. For a change in the quadrupole strength of +300, the BTF measurements yielded a negative threshold. This indicates that M_{34} changed its sign and the product $M^* \sin(\omega T_r)$ is positive.

6.2.3 Discussion

The method of point-to-point focusing proved to be a straightforward and effective method to suppress BBU much of the time. This is due to the fact that there is only a single dangerous mode that prohibits operation with 10 mA of beam current (see Table 4.2). One of the attractive features of this method is that the beam optics remain decoupled transversely and that the beam envelopes are minimally effected.

There are, however, some limitations to this method. For an extended linac containing many dangerous modes, it may not be advantageous to modify the phase advance. While one mode may be stabilized, in all likelihood the resulting change in phase advance will have harmful effects on other modes which were previously not a threat for BBU. Although this was never investigated in earnest, there is evidence to suggest that this situation occurred in the FEL when the threshold current became as low as 400 μA. Adequate suppression was generated for the HOMs in cavity 7, but the resulting change in phase advance caused an order of magnitude increase in the M_{34} element of the recirculation matrix from cavity 1 back to itself, from which BBU was facilitated at an even lower threshold current. Therefore care should be taken when applying this method to large-scale ERLs with extended linacs.

6.3 Local Reflection

The idea behind implementing a local reflector is to map a BBU-induced vertical kick into the horizontal plane, and likewise to map a BBU-induced horizontal kick into the vertical plane. The transport matrix describing a reflection about a plane at 45° to the horizontal or vertical axis takes the following form, where each element represents a 2×2 matrix

$$\begin{pmatrix} 0 & M \\ M & 0 \end{pmatrix} \tag{6.10}$$

The 2×2 sub-block transport matrix M is the same for both exchanges (x to y, y to x). Thus, such a reflector cleanly exchanges the horizontal and vertical phase spaces. To see how a reflection can be effective in suppressing BBU, consider Eqs. (6.10) and (4.21). Because $M_{12} = M_{34} = 0$, for a mode oriented at 0° or 90° the threshold current becomes infinite. However, if an HOM is rotated at an angle α, not equal to 0° or 90°, then the recirculated beam will not come back to the cavity with an angle $(\alpha + 90)°$ and its projection on the HOM will be nonzero. To get an infinite threshold for all HOM polarizations requires that $M_{32} = -M_{14}$.

The statement concerning an infinite threshold current is made in the context for which Eq. (4.21) was derived, namely that only a single mode is present in the cavity. In reality, dipole HOMs come in pairs of orthogonal modes, and the feedback loop between the beam and the mode will be re-established through the coupled beam motions [72]. Nevertheless, some measure of suppression can be achieved by implementing such a scheme.

6.3.1 Implementing a Local Reflector

A practical implementation of a local reflector using 5 skew quadrupoles has been non-invasively embedded in the 3F region of the FEL Upgrade Driver. Each skew quadrupole is simply a normal quadrupole which has been rotated 45°. Operationally, normal quadrupoles upstream and downstream of the module are used as betatron matching telescopes. These allow transverse matching of the phase spaces across the reflector so that the module remains transparent to the rest of the machine [87]. Beam envelopes through the 3F region are shown in Fig. 6.3.

From an operational point of view, the local reflector is activated by first loading

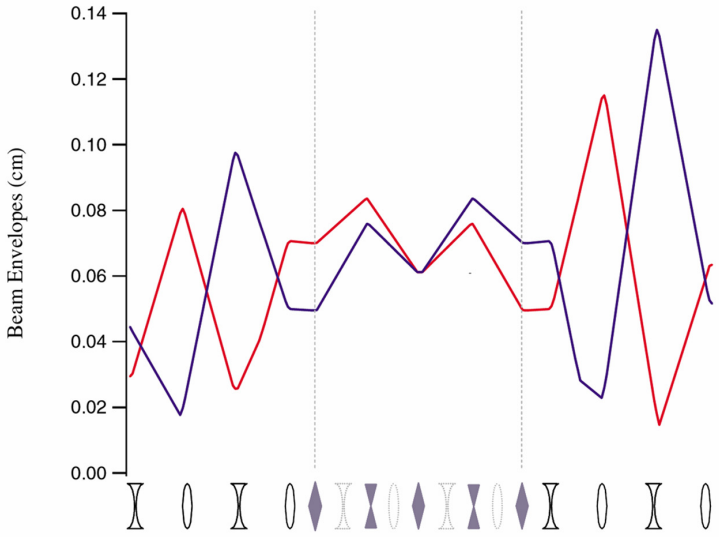

FIG. 6.3: Beam envelopes (horizontal in red and vertical in blue) for the 3F region of the FEL with the five skew quadrupoles (blue) activated and illustrating the exchange of horizontal and vertical phase spaces. The central four normal quadrupoles (dotted) are de-excited during reflector operation and the upstream and downstream quadrupoles (black) are used as betatron matching telescopes.

in the skew quadrupole strengths as determined from a model of the lattice. Directly translating the model values into the machine is typically sufficient to generate a reflection. To verify that the skew quadrupoles are correctly coupling the beam, four principle rays are launched through the local reflector module and the response of the downstream BPMs are monitored. Results of this process are illustrated in Figs. 6.4, 6.5, 6.6 and 6.7 [88].

Because the BPMs in the linac are not able to resolve two beam passes, the first several BPM readings are nonsensical. Figure 6.4 (Fig. 6.5) shows that a cosine-like (sine-like) trajectory in the horizontal plane is fully out-coupled into the vertical plane through the remaining 60 m of the recirculator to the beam dump. Likewise, Fig. 6.6 (Fig. 6.7) shows that a cosine-like (sine-like) trajectory in the vertical plane is fully out-coupled into the horizontal plane. Thus the skew quadrupole strengths are properly set.

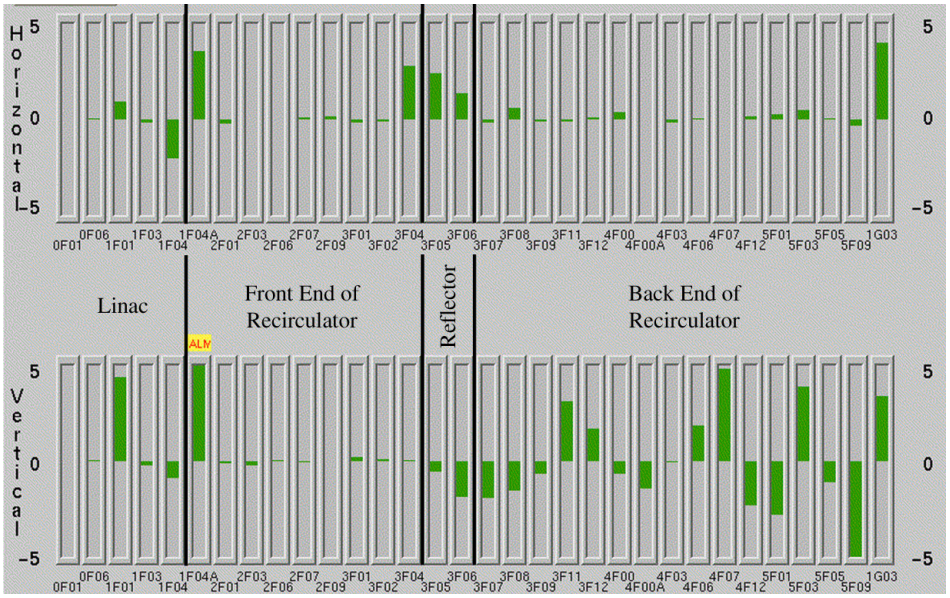

FIG. 6.4: Beam position monitor readings for a cosine-like trajectory launched at the entrance to the local reflector in the horizontal plane. Horizontal (vertical) displacements are displayed on the upper (lower) plot.

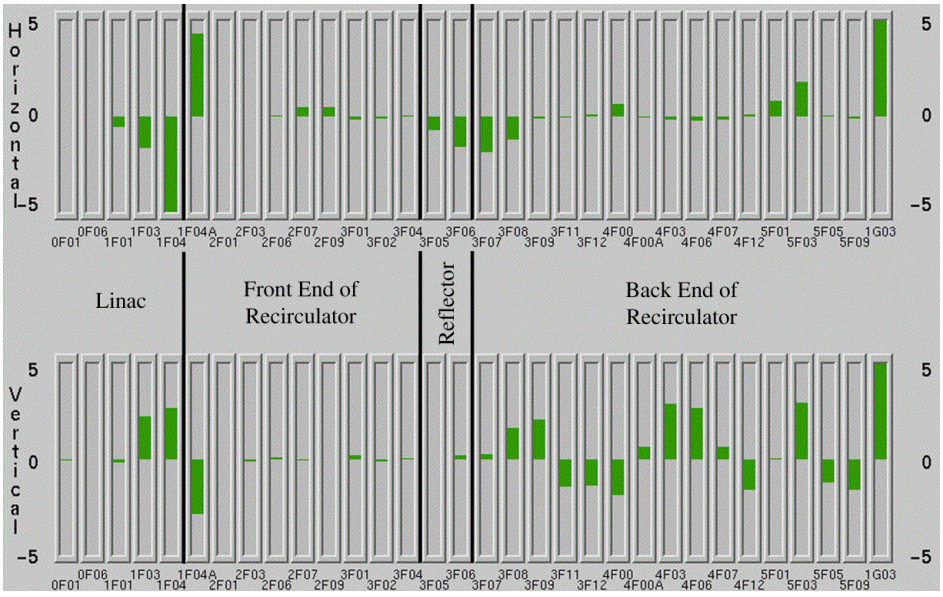

FIG. 6.5: Beam position monitor readings for a sine-like trajectory launched at the entrance to the local reflector in the horizontal plane. Horizontal (vertical) displacements are displayed on the upper (lower) plot.

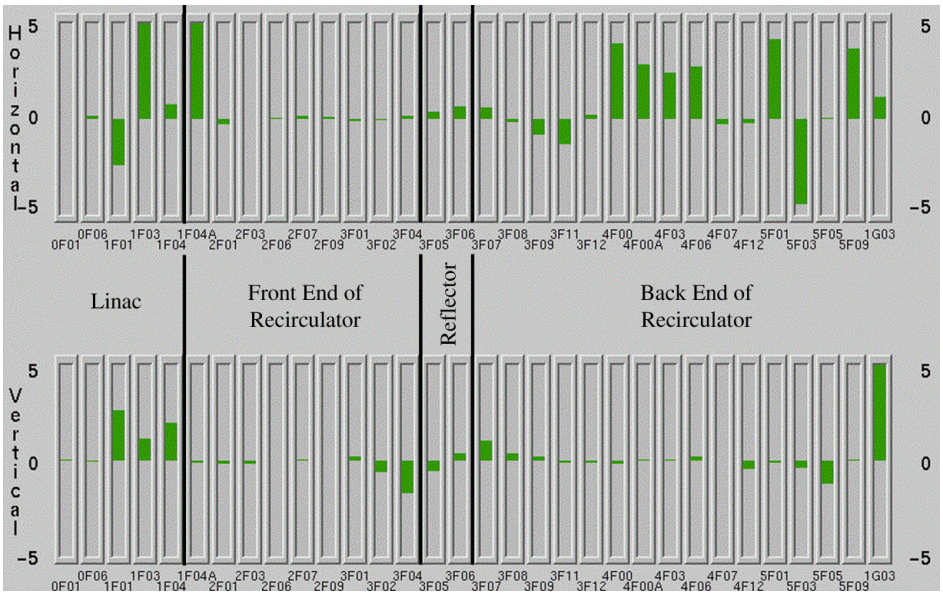

FIG. 6.6: Beam position monitor readings for a cosine-like trajectory launched at the entrance to the local reflector in the vertical plane. Horizontal (vertical) displacements are displayed on the upper (lower) plot.

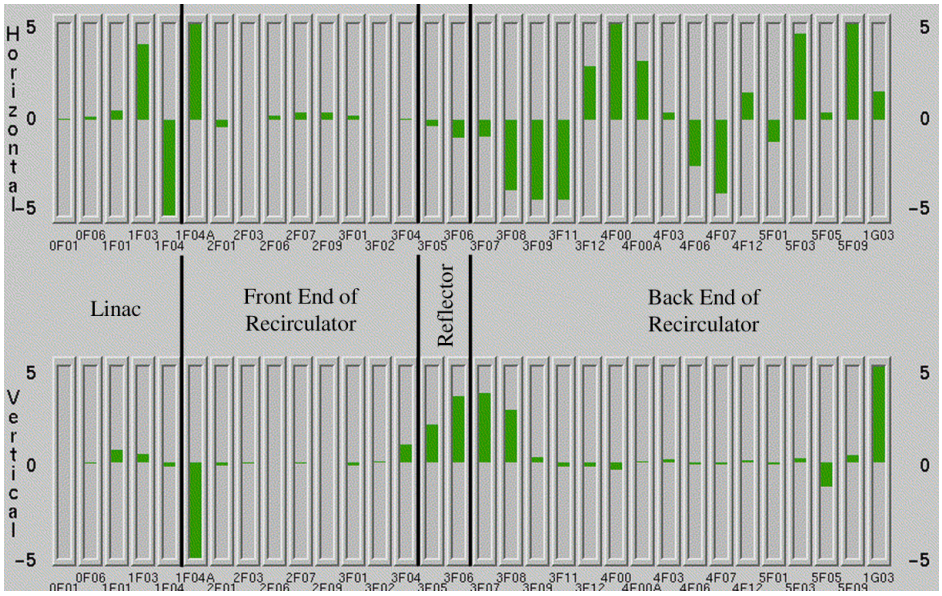

FIG. 6.7: Beam position monitor readings for a sine-like trajectory launched at the entrance to the local reflector in the vertical plane. Horizontal (vertical) displacements are displayed on the upper (lower) plot.

Using this process to verify that the reflector is operating correctly, virtually no remnant coupling is observed through the back end of the recirculator. In fact, the coupling introduced from the RF cavities (see Sections 2.2.3 and 3.3) prove to be more of an operational concern [61].

6.3.2 Measured Effect on the Threshold Current

The threshold current was first established to be 1.8 mA and caused by the 2106 MHz mode without the reflector. The reflector was then activated and operation with 5.0 mA of average beam current was achieved with no indications of BBU. Since direct observation was not possible, a BTF measurement of the 2106 MHz mode was performed. The results of the measurement yielded a new threshold current of (9.2 ± 0.4) mA; an increase by a factor of 5.1 (Fig. 6.8). Additional BTF measurements were performed for the 2116 MHz mode (also located in cavity 7) and the 2114 MHz mode (cavity 4). The concern was that by producing a reflection in the betatron planes, these modes which were stabilized for decoupled optics may become unstable. However, the results of the measurements indicate that the modes remained stabilized and did not pose a threat for causing the instability.

6.4 Global Rotation

The reflector described in Section 6.3 interchanges horizontal and vertical phase spaces, imaging each identically into the other. This will map a horizontal kick into the vertical plane, and a vertical kick to the horizontal plane, and thus is effective for suppressing BBU driven by modes with these specific polarizations. However, it will equally map a diagonal kick back into a similar diagonal displacement, thus failing to suppress BBU driven by an HOM of arbitrary polarization. Therefore a more robust scheme for BBU suppression can be achieved by generating a 90°

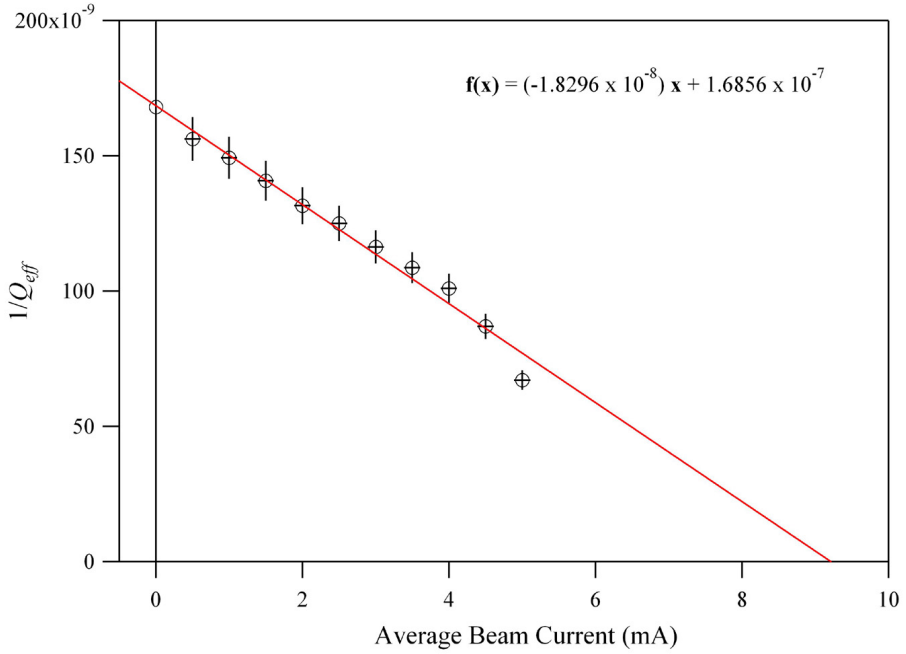

FIG. 6.8: A plot of $1/Q_{\rm eff}$ versus average beam current for the 2106 MHz mode with the local reflector activated. The best fit line is used to determine that the threshold current is 9.2 mA.

rotation of the betatron planes from cavity 7 back to itself.

The 4×4 recirculation transfer matrix for a 90° rotation is completely coupled and the off-diagonal 2×2 matrices are of opposite sign

$$\begin{pmatrix} 0 & M \\ -M & 0 \end{pmatrix} \tag{6.11}$$

From Eq. (6.11), $M_{12} = M_{34} = 0$, $M_{32} = -M_{14}$ and the threshold current given by Eq. (4.21) is infinite independent of the mode orientation, α. For a single mode the idea is conceptually simple and is illustrated in Fig. 6.9. If on the first pass an offending mode imparts an angular deflection α, to a bunch, then on the second pass (and after a 90° rotation), the resultant displacement will be orthogonal to the deflection. Thus the bunch will be unable to couple energy to the mode that caused the deflection. A rotation implemented in a two-pass system effectively

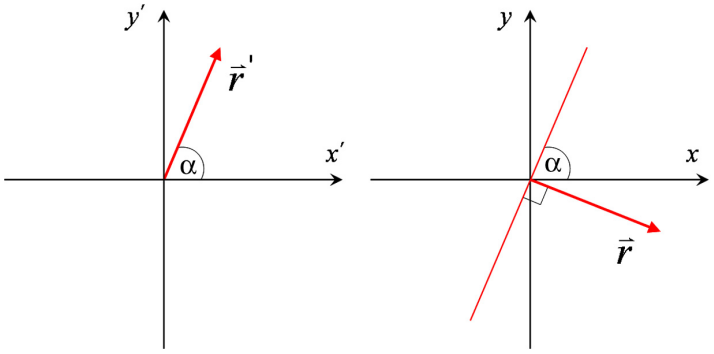

FIG. 6.9: A schematic illustrating the effect of a 90° rotation of the betatron planes. A deflection on the first pass (left) is transformed to a displacement which is orthogonal to the deflection which caused it (right).

breaks the feedback loop formed between the beam and cavity HOM so there can be no exchange of energy.

In reality however, similar to the local reflector, the beam will couple with the orthogonal polarization of the mode and the feedback will be re-established. Through simulations the effects of mode coupling will become evident in Section 6.4.3.

6.4.1 Implementing a Global Rotation

In principle a 90° rotation can be achieved with a solenoid magnet or with skew quadrupoles. Each scheme is briefly discussed below. Ultimately, however, skew quadrupoles were used in the FEL Upgrade Driver.

Solenoid

While utilizing a solenoid to produce a beam rotation seems like a natural choice, it is shown that the strong focusing incurred by its use makes it undesirable in low energy machines, and in high energy machines the large solenoid strength required makes it impractical. The 4×4 transport matrix for a solenoid which provides a 90° rotation is given by

$$\begin{pmatrix} 0 & 0 & 0 & 1/K \\ 0 & 0 & -K & 0 \\ 0 & -1/K & 0 & 0 \\ K & 0 & 0 & 0 \end{pmatrix} \tag{6.12}$$

where $K = B_o/2B\rho$ is the solenoid strength, B_o is the field inside the solenoid, and $B\rho$ is the rigidity of the beam. For initial studies of the feasibility of beam optical suppression methods, an appropriate set of optics was generated for incorporating a solenoid in the FEL Upgrade Driver. Quadrupole triplets upstream and downstream of the solenoid are used to transversely match the optics in the 4F region following the undulator. For a solenoid length of 75 cm, a solution of the matched betatron functions in the 4F region is shown in Fig. 6.10. For a 90° rotation the required solenoid strength, in terms of its length, is given by $K = \pi/2\ell$. The 75 cm solenoid used in this exercise translates to a solenoid strength of 2.1 m^{-1} or a magnetic field of 20 kG. Although this solenoid strength is feasible for the 145 MeV beam in the FEL, the strength required to rotate a beam of energy on the order of a GeV makes this method impractical. Another severe disadvantage of utilizing a solenoid is the undesirable strong focusing required to match the transverse optics (see Fig. 6.10).

Skew Quadrupoles

The goal is to produce a single turn recirculation matrix from the unstable cavity back to itself of the form given in Eq. (6.11). In principle without installing any additional hardware in the FEL, decreasing the unreflected vertical betatron phase advance around the recirculator by a quarter-betatron wavelength and activating the reflector in the 3F region results in a single turn transfer matrix from the middle of the zone 3 back to itself that describes a nearly perfect 90° rotation [88]. Thus an arbitrarily oriented HOM-driven kick returns not only out of plane

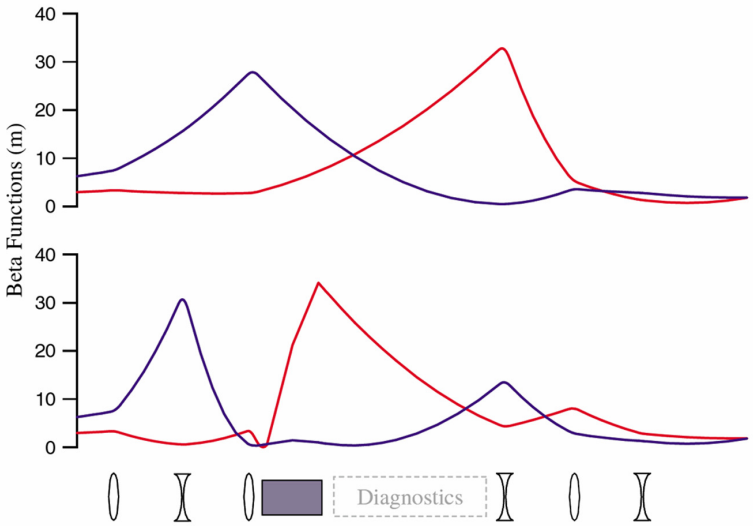

FIG. 6.10: Nominal betatron functions in the 4F region of the FEL (top) and with a solenoid (blue) activated to produce a 90° rotation of betatron planes with the upstream and downstream quadrupole triplets used for matching (bottom). Horizontal betatron functions are denoted in red and vertical in blue.

but also at a node in position.

6.4.2 Measured Effect on the Threshold Current

Having generated a recirculation matrix that describes a rotation, the usual procedure is followed of comparing the extrapolated threshold current from the BTF measurement to the nominal beam optics. The result of the measurement for the 2106 MHz mode with the rotator activated indicates that the mode is stabilized. In Fig. 6.11 the slope of the line that fits the inverse of the effective Q versus beam current data is positive. Extrapolating the line until it crosses the current axis, one concludes that the threshold current is -17.0 mA. This result once again demonstrates the attractiveness of the BTF measurement, by allowing one to determine whether the system is in the pseudo-stable regime or unstable while working at low average currents.

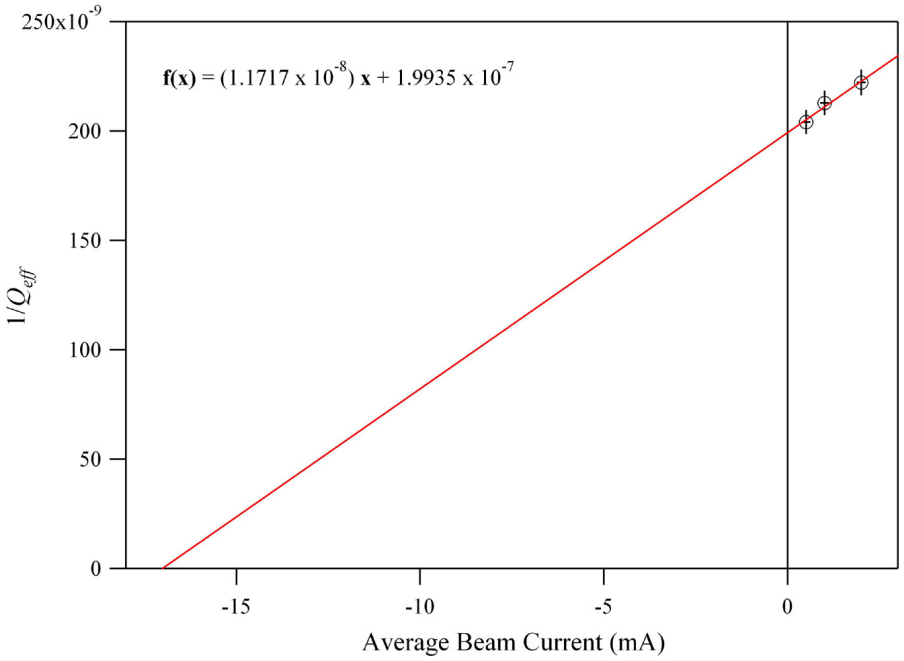

FIG. 6.11: A plot of $1/Q_{\text{eff}}$ versus average beam current for the 2106 MHz mode with the rotator activated. The best fit line is used to determine that the mode is stabilized.

Only a limited number of data points were measured because the machine configuration proved to be extremely sensitive to beam loss in the recirculator. Despite the lack of data, it is clear that a perfect 90° rotation was not achieved. In the case of a true 90° rotation, the effective Q would remain constant as the average beam current is varied.

6.4.3 Simulations of Coupled Optics Suppression Techniques

Simulations using the ERLBBU code were performed to investigate the relationship between the threshold current, the number of dipole HOMs per cavity and the HOM polarization for three different optics in the FEL Driver. The first set of optics is the nominal 88 MeV decoupled optics. The remaining two optics are a local reflector and a 90° rotation. The motivation for the study is: (1) to see if better BBU suppression with coupled optics can be achieved by varying the HOM

polarization and (2) to determine if a global rotation is more robust in its ability to increase the threshold current than a local reflector.

Before discussing the details of each case, a brief explanation of how the simulations were performed is required. Initially, all of the fourteen measured dipole HOMs in each of the eight cavities of zone 3 were simulated for each of the three machine optics. Dipole HOMs were then removed according to their impedance, $(R/Q)Q_L$, the lowest impedance modes being removed first, so that for the case of a single dipole HOM per cavity only the mode with the highest impedance is simulated. Each dipole HOM is assumed to be comprised of two orthogonal polarizations. These polarizations are then rotated by an angle with standard deviations of (0, 5, 10, 15, 20, 25, 30, 35, 40, 45)°. A total of 140 simulations (14 dipole modes × 10 rotation angles) were performed for each optics configuration with the results presented by the two-dimensional surface plots shown in Figs. 6.12, 6.13 and 6.14 for the decoupled optics, local reflector and global rotation, respectively.

In the instance of decoupled optics, the threshold current remains relatively insensitive to changes in the HOM polarizations. As the deviation of the mode orientations from 0° and 90° increases, the threshold current also increases, albeit only slightly, consistent with Eq. (4.21). Because the optics is decoupled and the modes well separated in frequency, coupling between modes is negligible and the current for stability can be determined by the threshold current due to the worst individual mode.

The optics describing the local reflector were derived from machine all-save values used for the measurements described in Section 6.3.1. From the arguments of Section 6.3, the expected increase in the threshold current is observed. The point of interest however, is that as the HOM rotation angle increases, the effectiveness of the local reflector rapidly diminishes. Thus, unless it is known that dangerous HOMs are oriented very nearly to 0° or 90°, a reflection scheme may not adequately

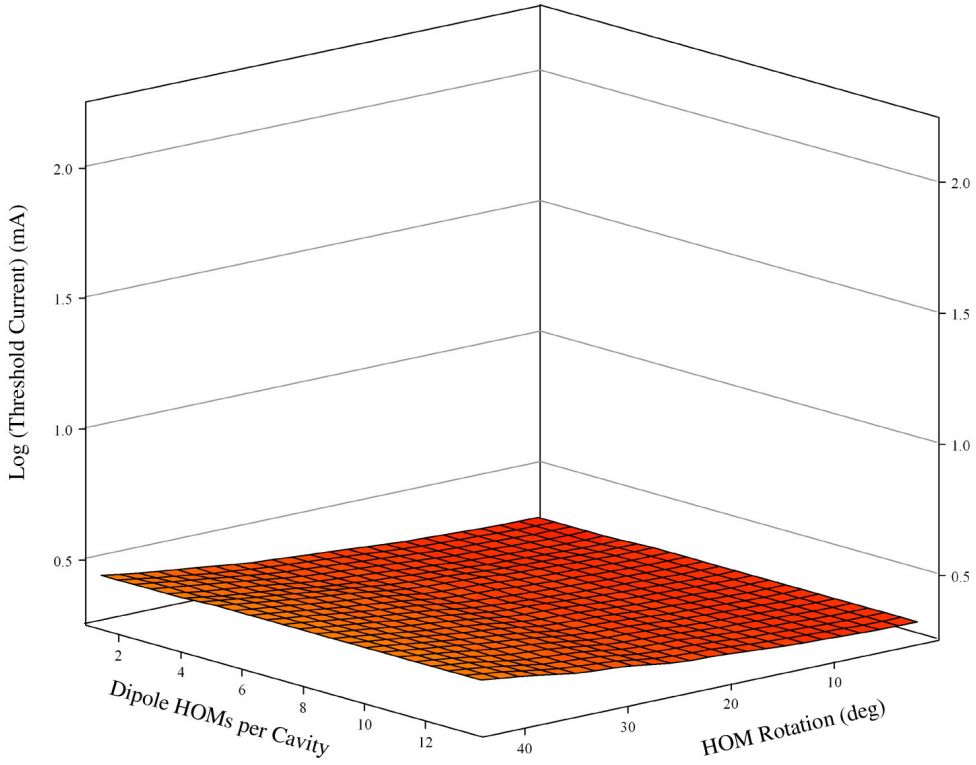

FIG. 6.12: Threshold current for nominal, decoupled optics as a function of the number of dipole modes per cavity and the HOM rotation angle.

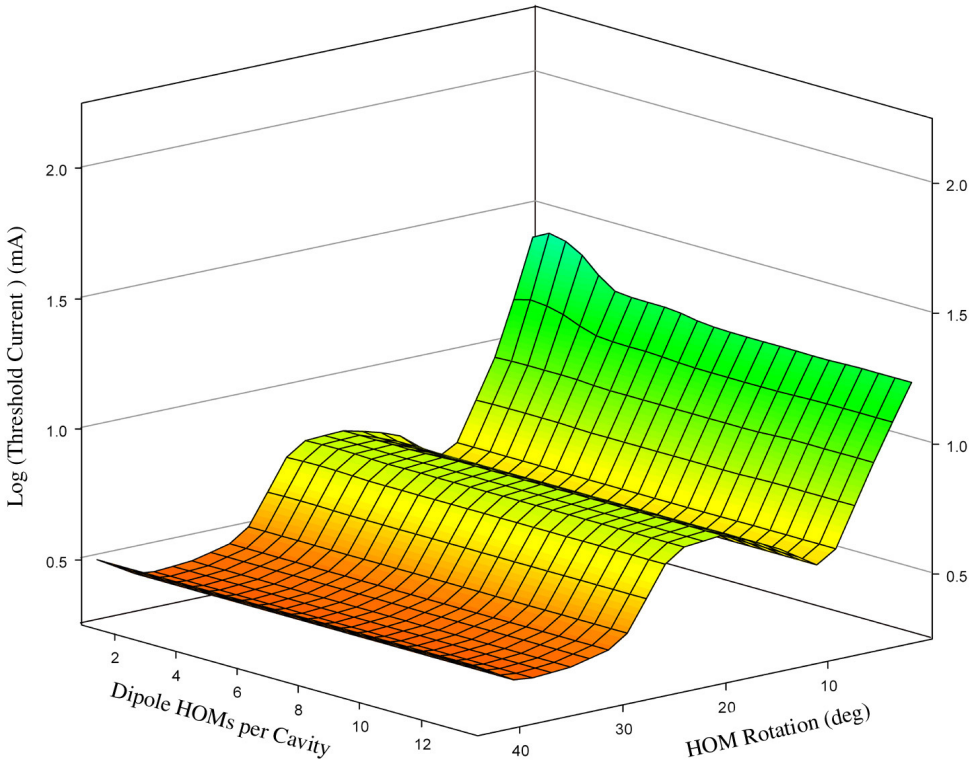

FIG. 6.13: Threshold current utilizing a local reflector as a function of the number of dipole modes per cavity and the HOM rotation angle.

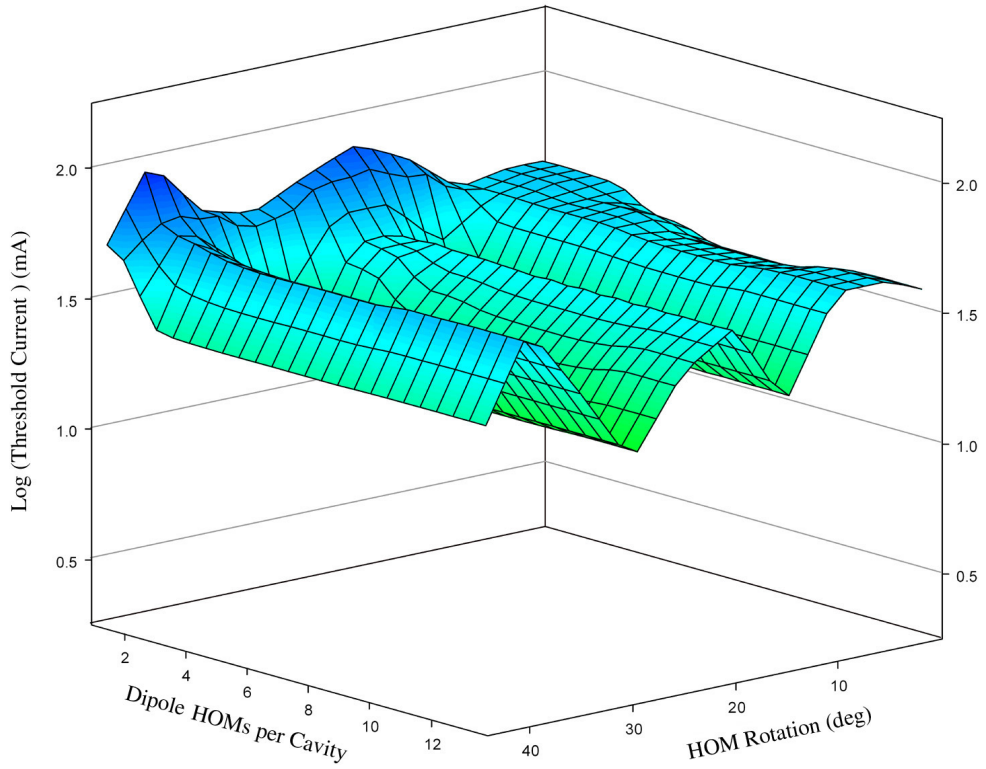

FIG. 6.14: Threshold current utilizing a rotator as a function of the number of dipole modes per cavity and the HOM rotation angle.

suppress BBU.

As mentioned in Section 6.4.2, a true 90° rotation was not achieved in the FEL Upgrade. For the sake of the simulations, a fictitious optics was generated to simulate the effect of a rotator such that a 90° rotation is achieved from cavity 7 back to itself. As the mode polarizations deviate from 0° and 90°, a rotation remains more effective at suppressing BBU than the reflector.

Discussion

Several important conclusions can be drawn from the aforementioned simulations. The first is that varying the angle at which the two orthogonal polarizations deviate from 0° and 90° did not improve the effectiveness of the suppression techniques. In fact, in the special case of the local reflector, as the deviation increased the threshold current became rapidly smaller, from approximately 25 mA to 3 mA when the rotation angle was 45°. Although such a decline does not occur with the rotator, neither does changing the polarization angle bring any significant advantage.

The primary objective of this simulation study, however, was to bring attention to the fact that HOM orientations can play an important role in the choice of suppression techniques, which until recently, has been overlooked [89]. One of the salient conclusions is that a global rotation is clearly a more robust suppression technique for arbitrarily polarized higher-order modes. This can be understood by recalling that the threshold current is inversely proportional to M^*, defined in Eq. (4.19). For a local reflection, $M_{14} = M_{32}$ which will increase M^*. A rotator on the other hand, with $M_{14} = -M_{32}$ will, in general, tend to decrease the value of M^* and thereby increase the threshold current.

It is important to keep in mind that these simulations were performed for the Jefferson Laboratory FEL Upgrade Driver, which is comprised of 3 cryomodules with a small number of dangerous HOMs which are well separated in frequency. As

TABLE 6.1: Summary of the measured effects of suppression techniques on the 2106 MHz mode.

Suppression Technique	Effect on 2106 MHz mode
Point-to-Point Focusing	Stabilized
Local Reflector	$5.1 \times I_{th}$
Rotator	Stabilized

the number of HOMs increases and/or better damping is obtained, the likelihood of overlapping modes increases and optical suppression techniques become less effective. In fact, for large accelerators with many cryomodules, using these beam optical schemes in the presence of many HOMs can cause further destructive mode interference thus rendering these suppression techniques ineffective altogether.

Recently, it has been proposed to fabricate elliptical RF cavities to deliberately break the cylindrical symmetry, thereby lifting the dipole HOM degeneracy and generating a large frequency spread between the two polarizations [90]. Assuming the dipole modes are sufficiently separated in frequency from cavity to cavity, then using elliptical cavities in conjunction with coupled optical suppression techniques can be effective at increasing the threshold current in machines with many cryomodules [91].

6.5 Summary

Beam optical suppression techniques proved to be very effective at increasing the threshold current in the FEL Upgrade Driver. A summary of the various methods and their effect on the 2106 MHz mode is displayed in Table 6.1.

Using point-to-point focusing and the rotator, the 2106 MHz mode could be stabilized. However since point-to-point focusing cannot be arranged for each individual cavity in an accelerator with an extended linac, the usefulness of this method is restricted to smaller machines or machines where dangerous HOMs are well local-

ized. And while it did not provide complete suppression, the local reflector is routinely used in beam operations to achieve high average currents in the FEL Driver. In October 2006, the reflector was activated when the FEL achieved 14.3 kW of laser power at 1.6 microns by running 8 mA of average beam current in cw mode [92].

Despite the ability of the rotator to stabilize the dangerous mode, caution should be exercised when intentionally introducing strong betatron coupling. While it is possible to manipulate the transfer matrix to create reflections and rotations, internal mismatch can generate beam loss that limits machine performance just as readily as BBU [93]. This proved to be the case when implementing the rotator and is the reason for the limited number of data points measured.

Demonstrating through simulations that the threshold current can be made sufficiently high through the use of these coupled optics is one issue. An equally important issue is the operational ramifications of such schemes; that is, meeting the stringent requirements and maintaining sufficient control of a transversely coupled beam. Take for example the largest scale energy recovery experiment to date, CEBAF-ER, where coupled transverse motion was evident as a result of the fields in the cavity HOM couplers. As it was discovered, trying to thread a coupled, energy recovered beam through 200 m of linac, though possible, is a formidable task.

While optical suppression techniques remain promising, ultimately, stronger HOM damping must be provided in future high current ERL applications.

CHAPTER 7

BBU Suppression: Feedback Mechanisms

In addition to modifying the electron beam optics, the threshold current can also be increased by modifying the characteristics of the dipole HOM. The properties that define an HOM are its frequency, Q_L, (R/Q) and the polarization of the mode. Because the cavities have been fabricated and installed, the latter two quantities are fixed. The frequency and Q_L, however, may still be modified.

Damping the HOM quality factors is achieved primarily by HOM couplers. However, since the damping in the zone 3 cavities is insufficient to prevent BBU below 10 mA, two methods to provide further damping were developed. Sections 7.1.1 and 7.1.2 discuss the successful implementation of cavity-based feedback systems which lower the loaded Q of a selected mode.

While it was not pursued as earnestly as other suppression techniques, measurements of the HOM frequency shift as a function of the mechanical tuner position were made. With a sufficient frequency shift of the HOM, the phase factor $\sin(\omega T_r)$ can change sign and the mode will be in a pseudo-stable regime where the thresh-

old current is on the order of several Amperes. As a consequence of this method, the fundamental frequency is also shifted and the cavity must be set to zero accelerating gradient, essentially making it a drift space. Because these measurements were performed in 2004, the effect was measured specifically for the 2114.156 MHz mode as it was causing BBU at the time (see Section 5.3). While the mechanical tuner is capable of shifting the fundamental mode frequency by $\pm$200 kHz, the 2114.156 MHz mode shifted less than 100 kHz. Ultimately, because methods such as point-to-point focusing proved to be so effective, the effects of these frequency shifts on the threshold current were never investigated experimentally.

7.1 Cavity-based Feedback

Cavity-based feedback aims to directly lower the Q_L of a dangerous HOM. Two feedback mechanisms were experimentally tested and are discussed in the following two sections.

7.1.1 Active Q-damping Circuit

The idea of the damping circuit is as follows: couple voltage from one of the HOM ports and using a narrowband filter select the HOM frequency of interest, shift the signal by 180° in phase, amplify the signal and then return it to the cavity through the same HOM port. A schematic of the setup is given in Fig. 7.1. By adjusting the gain and phase shift, the quality factor of the HOM could be reduced by a factor of 20. However, for these optimally tuned values of the gain and phase shift, the feedback loop became very sensitive to external disturbances, such as motion in the cables and the effects of the amplifier warming up. To avoid issues with stability, the feedback circuit was set to reduce the Q_L of the 2106 MHz mode by a factor of 4.8 (see Fig. 7.2). The threshold current was determined to be 2.3 mA

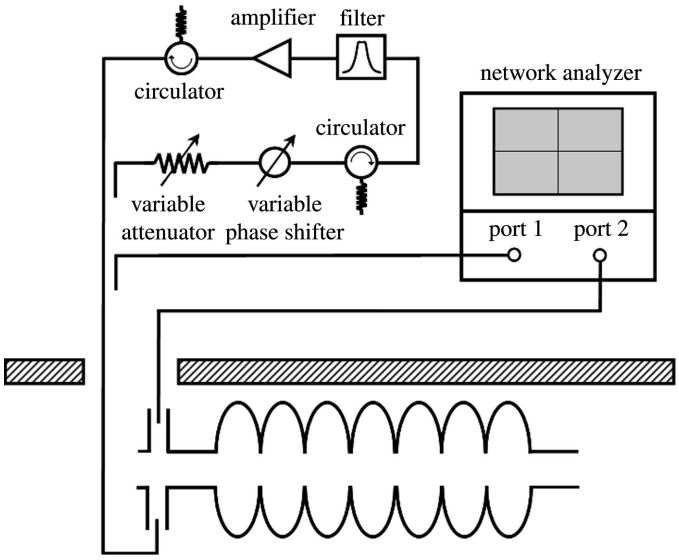

FIG. 7.1: A schematic of the feedback circuit used to damp the loaded Q of a mode.

with the damping circuit off by direct observation. When the beam was turned on, the BBU threshold was determined by the BTF method with the results shown in Fig. 7.3. The threshold current became (7.6 ± 0.2) mA.

7.1.2 Passive Q-damping with a Stub Tuner

A 3-stub tuner acts as an impedance transformer and is shown in Fig. 7.4. A stub tuner was attached to each cable connected to the two HOM ports of cavity 7. A schematic of the setup is illustrated in Fig. 7.5. The idea is to manipulate the stubs in such a fashion that the incident HOM voltage is reflected with a 180° phase shift. Because the stub tuner is a passive device, the attenuation in the cables from the HOM ports becomes a factor and prevented optimal Q-damping. Nevertheless, a modest decrease (a factor of 1.6) in the Q_L of the 2106 MHz mode and the corresponding increase in the threshold current were observed.

In principle, better suppression could be attained by connecting the stub tuner in the FEL vault, closer to the cryomodule, where cable attenuation would be re-

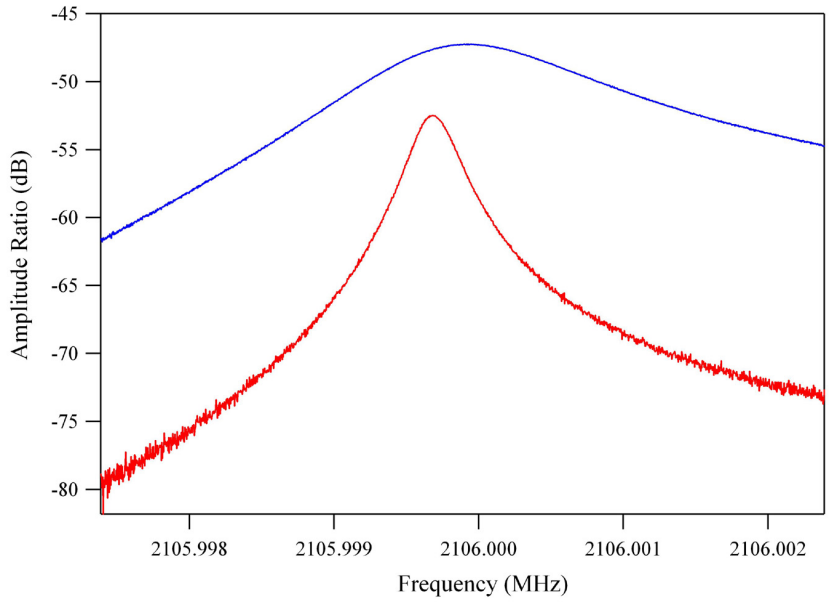

FIG. 7.2: The effect on the loaded Q of the 2106 MHz mode with the cavity-based, narrowband feedback off (red curve represents $Q = 6.2 \times 10^6$) and on (blue curve represents $Q = 1.3 \times 10^6$).

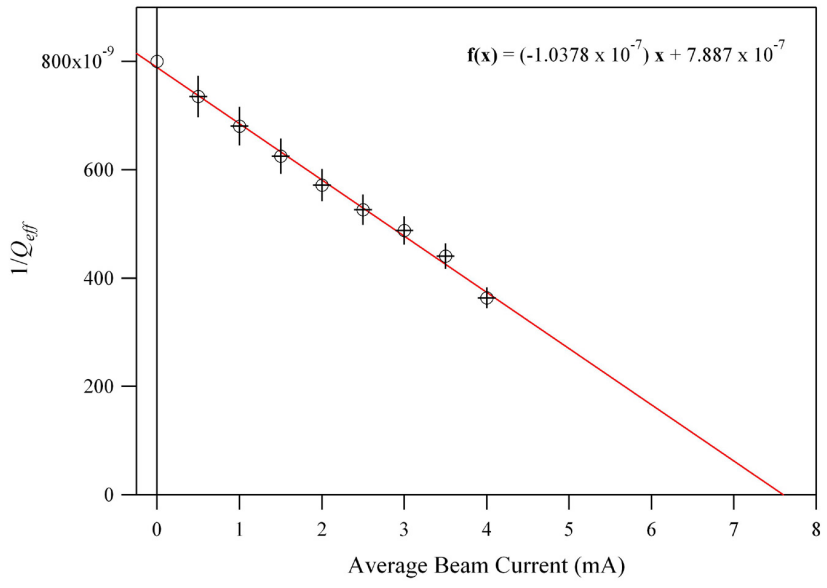

FIG. 7.3: A plot of $1/Q_{\rm eff}$ versus average beam current for the 2106 MHz mode with the Q-damping feedback circuit on.

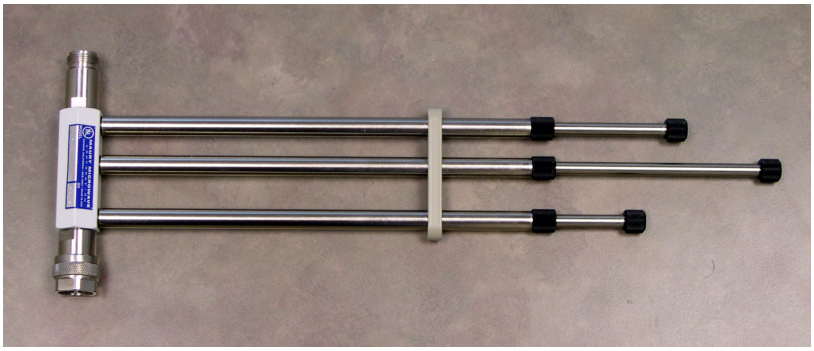

FIG. 7.4: A coaxial 3-stub tuner used for Q-damping.

duced significantly. For a long-term installation, care must be taken to insure only the dangerous dipole mode is affected, lest the stub tuner inadvertently modify the loaded Q of the accelerating mode, for example.

7.1.3 Discussion

Measurements have shown that methods to directly damp the loaded Q can increase the threshold by a factor of 3.3 and 1.6 using the damping circuit and 3-stub tuner, respectively, but can not completely stabilize the mode. If factors of a few are sufficient, then cavity-based feedback is an attractive alternative to the methods described in Chapter 6 because it does not interfere with the beam optics.

Nevertheless, as with the beam optical suppression techniques, the cavity-based feedback systems only treat the symptoms, rather than the source, of the problem. Ultimately the cure for the problem is to provide strong HOM damping.

7.2 Beam-based Feedback

Another class of feedback systems is beam-based, which combines the major advantages of the beam optical suppression techniques and the cavity-based feedback

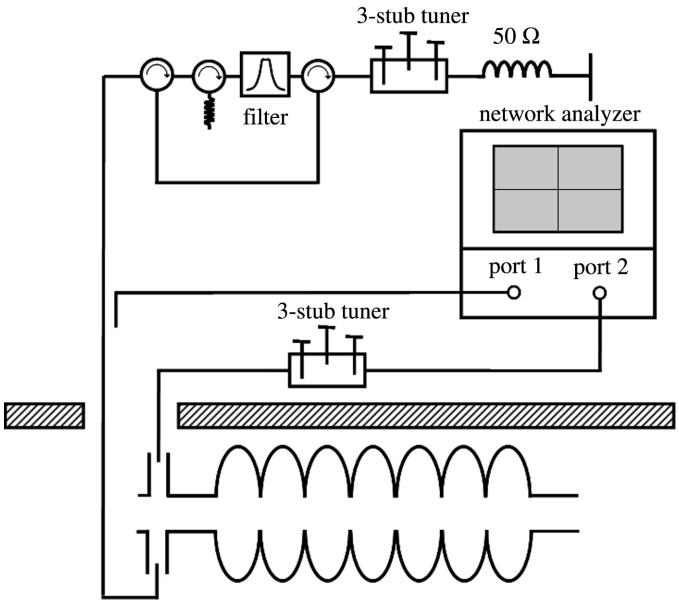

FIG. 7.5: Schematic of the experimental setup using a 3-stub tuner to damp the loaded Q of a mode.

systems. Like the cavity-based feedback, a beam-based feedback does not interfere with the machine optics and like beam optical control, the threshold current can, in principle, be increased by an order of magnitude or more. This section describes the results of initial studies concerning the viability of implementing a beam-based feedback system in an ERL and the anticipated effects on the BBU threshold current.

7.2.1 Overview

Conceptually, a transverse feedback system is simple. A sensor, or pickup, is used to measure the beam displacement at a location in the machine. A kicker is located downstream and imparts an angular kick to the beam proportional to the offset signal detected at the pickup. The correcting kick may be applied on the same turn or on subsequent revolutions, it may be applied to the same bunch that produced the signal at the pickup or it may act on preceding or following bunches.

All of these considerations are contingent upon the type of machine one is dealing with, the type and nature of the beam instability to control and the signal processing required of the system, among other things.

Feedback systems have long been successfully used in storage rings. However, there are fundamental differences in designing a system for an energy recovery linac, namely the fact that the beam spends a relatively short time in the machine. Ideally the feedback system will correct the same bunch that produced the error signal, but in an ERL the beam typically makes only two passes through the machine, requiring that the bunch be corrected on the same turn on which the signal was detected. This imposes stringent requirements on the signal processing time and instrumentation electronics to the extent that such a system may not be practical.

Consider, for example, the feedback time budget for the FEL Upgrade Driver. The recirculation time is 433.200 ns. In terms of time management, the ideal placement of the pickup is immediately downstream of zone 4 and the ideal placement of the kicker is immediately upstream of zone 2 and the distance between the two is approximately 50 m. For optimal feedback performance, for each bunch that gets a correcting kick, the error signal used is the one generated by that same bunch - that is, the condition where the feedback time delay, t_d, is zero. Yet, after taking into account the propagation time for a signal from the pickup to reach the kicker, only a few tens of nanoseconds remain in the time budget for processing the raw BPM signal, generating a suitable error signal and supplying sufficient gain. It is therefore not immediately clear whether adequate suppression can be achieved for $t_d \neq 0$.

Using an analytic model of BBU which incorporates the effects of a feedback system and also using the results of a recently developed BBU code to simulate the effects of feedback on the system's stability, it appears that a bunch-by-bunch feedback system may be feasible. Section 7.2.2 derives an expression for the threshold

current in the presence of feedback. Section 7.2.3 describes the tracking algorithm of a BBU simulation code which models a feedback system and Section 7.2.4 presents the results of simulations which provide insights into the effectiveness of such a system.

7.2.2 Analytic Model of BBU with Feedback

In this section an analytic model of beam breakup including the effects of a simple beam-based feedback system is described. Using the wake potential formalism from Section 4.4 the effect of the feedback is easily incorporated and a modified threshold current formula is derived [94].

For simplicity, consider the special case of a single HOM oriented in the vertical plane ($\alpha = 90$) and with uncoupled transverse optics ($M_{14} = M_{32} = 0$). A transverse kick on the first pass translates to a displacement of the beam bunch on the second pass and is given by

$$y_2(t') = M_{34}\left[\frac{V(t' - T_r)}{p_b(c/e)}\right] \tag{7.1}$$

The displacement of the beam bunch at the cavity on the second pass also includes a term that describes the effect of the feedback system. The feedback system to be modeled is a simple beam-based scheme in which a pickup downstream of the cavity is used to detect an error signal (i.e. bunch displacement) and is used to drive a kicker. A schematic of the setup is shown in Fig. 7.6. The kick applied is proportional to the detected displacement at the pickup and is amplified by a gain factor, g.

The displacement detected at the pickup can be written as

$$y_p(t') = M_{34}^p\left[\frac{V(t' - T_r - t_d)}{p_b(c/e)}\right] \tag{7.2}$$

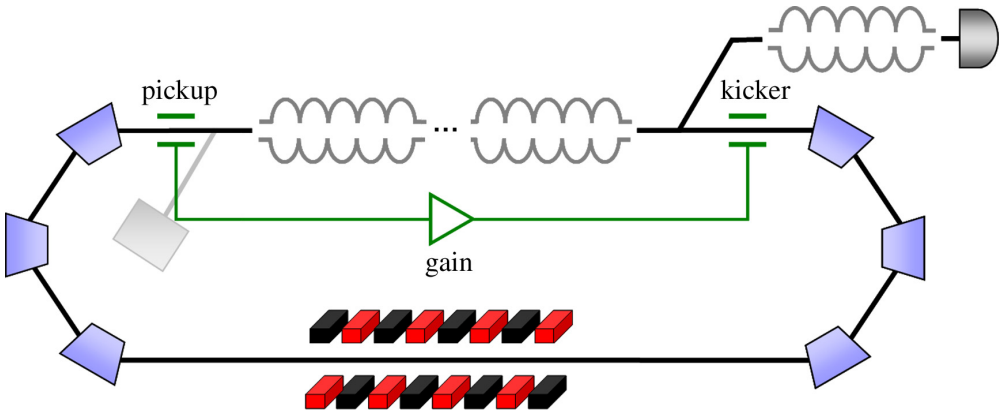

FIG. 7.6: Generic layout for a feedback system in an ERL.

where M_{34}^{p} is the matrix element that transforms an angular kick from the cavity HOM to a vertical displacement at the downstream pickup and t_d is the feedback delay time. For $t_d = 0$, the feedback is a bunch-by-bunch system in the sense that each bunch generates its own error signal and then is corrected by the kicker using that signal. For the situation where $t_d \neq 0$, a bunch generates an error signal which is only applied to the n^{th} trailing bunch, for example.

The displacement on the second pass at the cavity due only to the effects of the feedback is written as

$$y_{FB}(t') = gM_{34}^{k} y_p(t') = gM_{34}^{p} M_{34}^{k} \left[\frac{V(t' - T_r - t_d)}{p_b(c/e)} \right] \tag{7.3}$$

where M_{34}^{k} is the matrix element that transforms an angular kick from the feedback kicker to a vertical displacement at the cavity. Finally, the net displacement on the second pass is given by the sum of Eq. (7.1) and Eq. (7.3)

$$y_2(t') = \frac{1}{p_b(c/e)} \left[M_{34} V(t' - T_r) + gM_{34}^{p} M_{34}^{k} V(t' - T_r - t_d) \right] \tag{7.4}$$

With this new expression for the bunch displacement, the threshold current can be derived following the same steps outlined in Section 4.4 by replacing Eq. (4.33)

with Eq. (7.4). It follows that

$$K_{FB} \equiv \left(\frac{et_o \omega k (R/Q) M^{\text{eff}}}{2(c/e)p_b} \right) \tag{7.5}$$

where M^{eff} takes the place of M^* in Eq. (4.37) and is given by

$$M^{\text{eff}} = M_{34} + gM_{34}^p M_{34}^k e^{i\omega t_d} \tag{7.6}$$

After explicitly performing the sum, a modified dispersion relation is found

$$\frac{1}{I_o} = K_{FB} e^{i\Omega T_r} \left(\frac{\xi \sin(\omega t_o)}{1 - 2\xi \cos(\omega t_o) + \xi^2} \right) \tag{7.7}$$

where ξ is given by Eq. (4.42). After assuming a perturbative solution and expanding in Ω, the threshold current is found to be

$$I_{th} = -\frac{2V_b}{k(R/Q)Q_L M^{FB}} \tag{7.8}$$

where

$$M^{FB} = M_{34} e^{\frac{\omega T_r}{2Q_L}} \sin(\omega T_r) + gM_{34}^p M_{34}^k e^{\frac{\omega(T_r + t_d)}{2Q_L}} \sin(\omega(T_r + t_d)) \tag{7.9}$$

As expected, with no feedback $g = 0$, the threshold current derived in Section 4.2 (and using an alternative method in Section 4.4) is recovered.

For a physically viable solution, the threshold current must be a positive quantity. This condition requires that $M^{FB} < 0$ for Eq. (7.8) to be valid. Equation (7.8) is based on a perturbative treatment of the problem. Thus, for the perturbative solutions to be valid, the gain, g, must be less than $|M_{34}/M_{34}^p M_k^{34}|$ for $\sin(\omega(T_r + t_d)) > 0$ and greater than $|M_{34}/M_{34}^p M_k^{34}|$ for $\sin(\omega(T_r + t_d)) < 0$.

When these conditions are not met, the system is said to be in a pseudo-stable regime, where the negative threshold current implies beam stability. As discussed

in Section 4.2.1, however, in the pseudo-stable regime the threshold can be on the order of Amperes. For the 10 mA FEL Upgrade, and even for the proposed 100 mA ERL-based drivers, this represents, for all practical purposes, a stable system.

Because it is assumed that the pickup can generate a position signal for each beam bunch and likewise, that the kicker can impulsively kick each bunch independently, this represents an idealized model. In reality, the signal produced by a single bunch through a pickup-amplifier-kicker system will affect more than a single bunch [95]. This model does not take these effects into account, nevertheless, important insights can be gained about the performance of a feedback system.

7.2.3 BBU Code with Feedback

The ultimate goal of the feedback system is to put the system in the pseudo-stable regime, effectively pushing the threshold current to several Amperes. While the analytic models provide insights into the behavior of the system in the regime where $M^{FB} < 0$, the region of greatest interest is the pseudo-stable regime, for which the analytic model can offer no information. Therefore it is necessary to investigate this region with numerical methods using computer simulation codes.

Initial studies were performed in 2003 by modifying the code TDBBU to include a simple feedback system for the case of $t_d = 0$. Results from those simulations indicated that an unstable system could be stabilized by implementing such a feedback [94].

A code to simulate beam dynamics in a two-pass machine for a cavity containing a single HOM which is assumed to be oriented either purely horizontally or vertically was developed. The code was written using Igor Pro so that generating input files, executing the code and post-run analysis could be performed with the same program.

The tracking algorithm is the same as described in Section 4.3.1 except that

now step 5 is replaced with the following steps:

1. The first pass beam is propagated from the cavity to a downstream pickup according to a user-input transfer matrix. The beam displacement at the pickup, which is used as the error signal to drive the feedback system's kicker, is stored in an array.

2. The bunch is then transported to the kicker according to a user-input transfer matrix. The kicker imparts a transverse deflection which is proportional to the displacement at the pickup with a gain set by the user. For a feedback time delay of zero, the kicker simply imparts a kick to the bunch in proportion to the displacement of that same bunch at the pickup. The code also handles the more interesting case involving nonzero feedback time delays. In these instances the beam displacement is stored in an array and used at the kicker only after the passage of $t_d(f_{RF}/h)$ bunches, where t_d is the specified feedback time delay and f_{RF}/h is the bunch repetition frequency.

3. The beam bunch is transported from the kicker to the cavity according to a user-input transfer matrix.

The reason for creating a code capable of modeling only a single mode is due to the fact that, to a high degree of accuracy, BBU in the FEL Upgrade Driver can be described with the single mode analytic formula (see Section 4.7). By simulating even a single mode, important insights into the behavior of a feedback system can be gained.

Benchmarking the Code

To make certain that the simulation code was working correctly, it was first benchmarked with the results of ERLBBU for the case of no feedback, that is, with

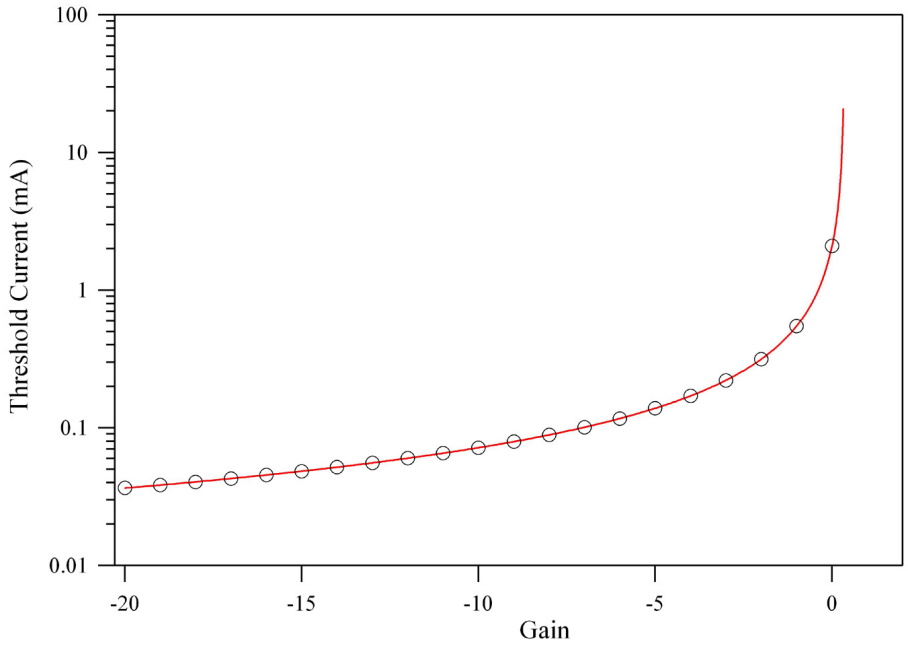

FIG. 7.7: The threshold current as a function of gain for $t_d = 0$ from the analytic model (red line) and the results of the simulation code (black open circles).

$g = 0$ in Eq. (7.8). The two codes were found to be in perfect agreement.

The next step requires benchmarking the code with the analytic model for the case of bunch-by-bunch feedback with $t_d = 0$. The results of simulations for the remainder of this chapter use the input parameters in Table 7.1. The matrix elements were extracted from all-save values from an 88 MeV setup. The value for M_{34} is from zone 3 cavity 7 (the location of the unstable mode) back to itself, the value for M_{34}^p is for a pickup located in the 2F region and the value for M_{34}^k reflects a kicker located in the 5F region. For the model to be valid, recall that $g < |M_{34}/M_{34}^p M_k^{34}|$ which is satisfied for these parameters.

The agreement between the analytic formula and the results of the simulation are summarized in Fig. 7.7. Without feedback, the threshold current is 2.1 mA. It is clear that the analytic model is correct in its region of validity. The more interesting situations, however, are for time delays in the feedback system ($t_d \neq 0$)

TABLE 7.1: Parameters used for simulations to study the effect of a bunch-by-bunch feedback system on the BBU threshold current.

Parameter	Value
ω	2106.007 MHz
Q_L	6.11×10^6
(R/Q)	29.9 Ω
V_b	39 MV
T_r	433.200 ns
M_{34}	-5.1 m
M_{34}^p	1.1 m
M_{34}^k	13.7 m

and the behavior of the system in the pseudo-stable regime ($M^{FB} > 0$) where the feedback system acts to increase, rather than decrease, the threshold current.

7.2.4 Simulation Results

A number of simulations were performed to ascertain some of the parametric dependencies in the pseudo-stable regime. All simulations were performed with the parameters in Table 7.1. The remaining free parameters are the feedback time delay (t_d) and the feedback gain (g).

As discussed in the previous section, the effect of feedback time delay is the most important issue for determining if sufficient suppression can be achieved if the bunch corrected/kicked uses an error signal derived from a different bunch. Simulation results showing the dependence of the threshold current on the time delay (for $g = 1$) are given in Fig. 7.8. The value of threshold current oscillates and as the time delay increases, the maximum achievable threshold decreases according to a power law. The functional dependence of the maximally achieved threshold current (represented by black markers in Fig. 7.8) as a function of the time delay is shown in the log-log plot in Fig. 7.9. The data is fit with a straight line of slope -0.93. Thus, for the parameters used in these studies, the maximum threshold

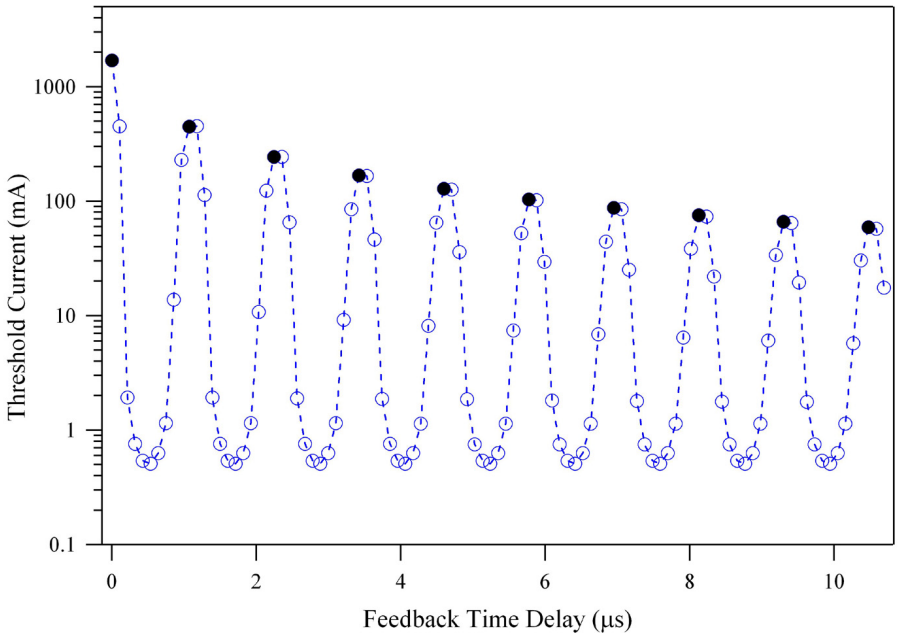

FIG. 7.8: Threshold current versus the feedback time delay. As the time delay gets longer the maximum achievable threshold decreases according to a power law (see Fig. 7.9). Black circles mark the highest threshold current for each period of the oscillation.

possible by implementing a bunch-by-bunch feedback system scales as $t_d^{-0.93}$.

Figure 7.10 shows the threshold current as a function of the feedback gain for several different values of time delay. The values of t_d were chosen such that they correspond to the maximum achievable threshold current (i.e. the black markers in Fig. 7.8). In the region for which the analytic model is valid ($g < 0.35$) the simulations show excellent agreement, save for the case of the longest time delay (423 μs) where the perturbative treatment of the problem begins to fail.

From a practical point of view, for $t_d < 423$ μs and for $g = 1$, the threshold current can be increased with a feedback system. Not surprisingly, the best suppression occurs when $t_d = 0$ and the feedback is truly on a bunch by bunch basis. To achieve an order of magnitude increase in the threshold current, from 2.1 mA to 21 mA, requires a feedback time delay of less than 30 μs. Conversely, for delays greater than 423 μs, the threshold current becomes completely ineffective, independent of

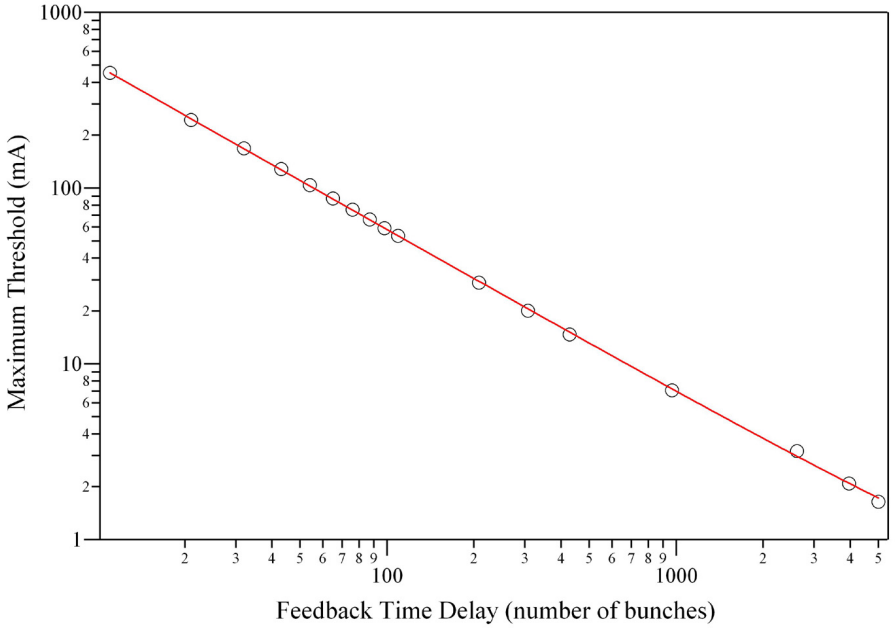

FIG. 7.9: The maximum threshold current that can be achieved with feedback as a function of time delay. The best fit line has a slope of -0.93.

the gain.

Finally, the relationship between the required feedback time delay to achieve a threshold current of 2.1 mA as a function of the gain was investigated. The resulting isoline is given on the log-log plot in Fig. 7.11. The data is fit with a straight line of slope -0.86. Thus, for the parameters used in these studies and for a 2.1 mA threshold current, the feedback time delay scales as $g^{-0.86}$. For each value of the gain, time delays which lie below the best fit line will lead to a threshold current which exceeds 2.1 mA while points above lead to thresholds less than 2.1 mA.

7.2.5 Conclusions and Implications

A simple BBU code has been developed to study, in particular, the effects of time delays for implementing a bunch-by-bunch feedback system. While the details of the results reported in the previous section depend largely on the specific choice

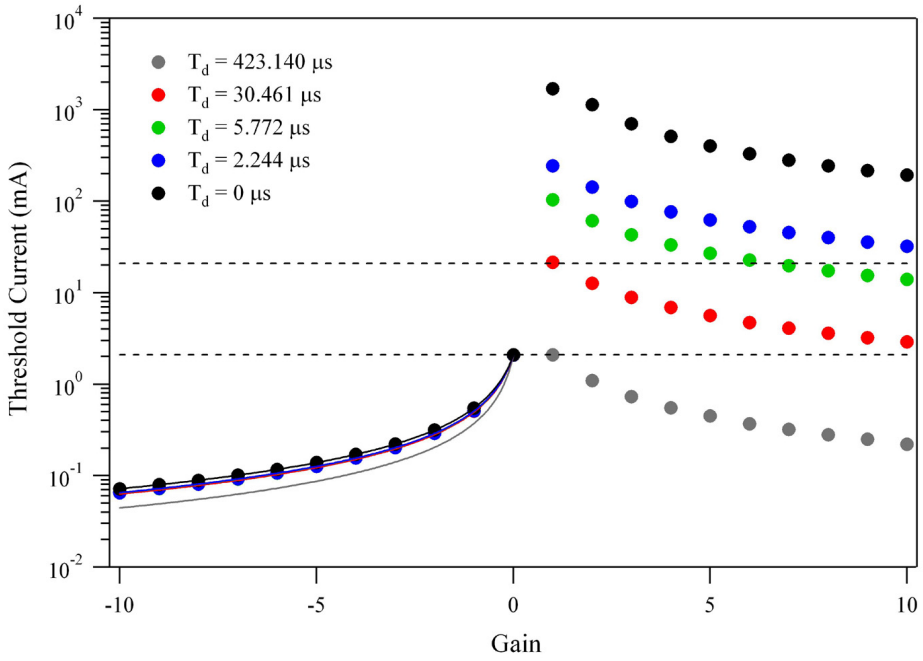

FIG. 7.10: The threshold current as a function of feedback gain for several different time delays. The lower and upper dotted lines mark threshold currents of 2.1 mA and 21 mA, respectively.

of simulation parameters, in general, the following conclusions can be drawn:

1. The most effective suppression for BBU occurs when $t_d = 0$, although effective suppression of BBU can be arranged for finite feedback time delays

2. The maximum threshold current that can be obtained by implementing feedback decreases as the time delay increases (the rate at which this occurs depends on the simulation input parameters)

3. For large time delays, a feedback system will only decrease the threshold - regardless of the gain.

The last point is worth emphasizing; unless the required time budget can be met, the feedback will be completely ineffective. In fact, using the feedback in this regime will act to only decrease the threshold current further.

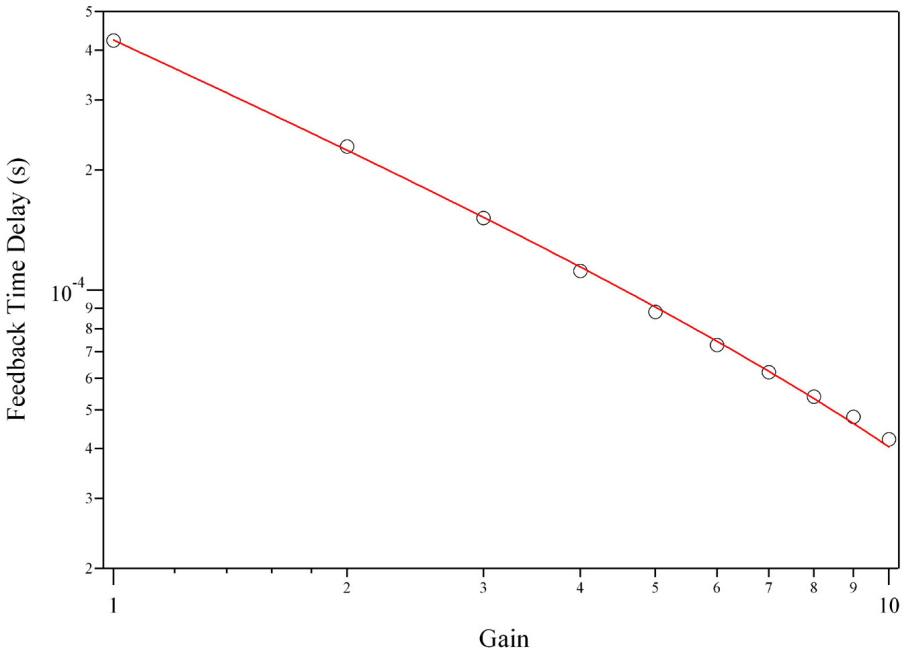

FIG. 7.11: The feedback time delay as a function of gain. The best fit line has a slope of -0.86.

CHAPTER 8

Conclusions

The work presented in this dissertation addresses some of the most relevant issues regarding pushing the frontier of ERLs, in particular, exploring energy recovery with high energy and on a large scale, and the high average current effects that arise. The contributions in these two regimes are described in the following sections.

8.1 CEBAF with Energy Recovery

The experiment to energy recover the beam in the CEBAF accelerator represents the first attempt to bridge the gap between the existing low energy (order 100 MeV), compact (up to 3 cryomodules), SRF-based ERLs and the proposed ERL drivers of the future. While it would have been ideal to have more quantitative measurements of the second pass beam, by successfully energy recovering the beam several important milestones were established. To date, CEBAF-ER has demonstrated energy recovery

- of the highest energy beam (1 GeV)
- on the largest scale (through a 1.3 km transport channel)

- through the largest SRF environment (312 cavities)
- with the highest final-to-injector energy ratio (51:1)

8.2 Studies of Beam Breakup

The form of beam breakup discussed in this dissertation was first observed in an independent orbit recirculating linac (SCA) and then in a microtron (MUSL-2) in 1977. In 2004 BBU developed in the FEL Upgrade Driver and represents the first observations of the instability in an energy recovering linac.

Beam breakup is well understood from a theoretical point of view and now, as result of the work presented in this dissertation, from an experimental point of view. The primary contribution is the successful benchmarking of BBU simulation codes with experimental data with agreement to within 10%. These codes are a valuable tool whose results dictate many of the most important parameters in the design of future high average current ERLs, such as HOM damping requirements of the SRF cavities and the means by which it is achieved and the choice of machine optics. With a number of design proposals for ERL drivers on the horizon, it is vitally important that the BBU codes can be applied with confidence.

In the process of benchmarking the codes, several important auxiliary contributions were made. First, the validity of the analytic model used to describe BBU has been demonstrated in small machines where HOM frequencies do not overlap. In particular, the threshold current formula for a single cavity containing a single mode, if applied correctly, has been proven to describe BBU with a high degree of accuracy. Secondly, several important experimental techniques were introduced and applied to BBU-related measurements.

To adequately benchmark the codes, as many of the input parameters as possi-

ble were experimentally measured. Due to the nature of BBU - that it involves the properties of the beam (average current and energy), the machine lattice (transfer matrices) and the properties of the HOMs (frequency, Q_L, (R/Q) and polarization) - a number of different measurements were required. There also is the necessity for techniques to accurately measure the threshold current. The beam transfer function measurement has been used for many decades and has now been successfully applied, along with measuring the HOM growth rates, to measure the threshold current.

It is important to keep in mind that BBU work reported in this dissertation addresses a specific regime; namely, a machine with only a few very high Q dipole modes which are localized in a single cryomodule in a relatively compact machine. Furthermore, in frequency space, the modes are well separated so that for decoupled optics, coupling between modes is not an issue. Because of these characteristics, all of the suppression techniques implemented were, to varying degrees, successful at increasing the threshold current for stability.

Three different beam optical suppression techniques were implemented; point-to-point focusing, a rotator and a local reflector. The first two were able to suppress BBU due to the 2106 MHz mode completely, while the local reflector increased the threshold by a factor of 5.1. The latter two techniques are notable in that they required the introduction of strong transverse coupling in the electron beam optics. Additionally, two different cavity-based feedback systems were developed and proved to be successful at increasing the threshold current by factors of a few.

Finally, some initial studies of the feasibility of a beam-based feedback system for an ERL were presented. Such a beam-based system incorporates the advantages of both beam optical control and cavity-based feedback methods of suppression. In addition to showing the validity of a modified threshold current formula to include feedback, simulation results also explored the behavior of the BBU threshold current

in the pseudo-stable regime. Based on these results, implementing a bunch-by-bunch feedback system in an ERL, specifically the FEL Upgrade Driver, is feasible. However, technical issues regarding the hardware, such as the placement of pickups and kickers, BPM resolution, kicker power and other similar issues, have as of yet, not been addressed.

While currently there is a push to construct large scale ERLs for light sources and other uses, there is also a movement towards constructing more affordable, compact ERL drivers [5, 96]. Therefore, the BBU work presented here, which applies to such machines, will continue to be relevant in the coming years.

8.3 Future Work

An important area of research for the future will be implementing beam-based feedback systems in ERLs, in particular to combat the effects of BBU and other beam instabilities that may degrade machine performance at high average currents. Continued development in the area of HOM damping is required for the next generation of ERLs. To date, 9 mA of average beam current has been successfully energy recovered through an SRF environment without any indications of multipass beam breakup developing. Demonstrating the ability to accelerate 100 mA of average beam current with no harmful effects from HOMs will be an important milestone for the development of future ERL-based particle accelerators. Ultimately, the next step is to demonstrate energy recovery with a high energy, high average current beam.

APPENDIX A

The Pillbox Cavity

Starting from Maxwell's equations for a source free region and assuming solutions with a harmonic time dependence, $e^{-i\omega t}$, one can write

$$\nabla \cdot \vec{E} = 0 \tag{A.1}$$

$$\nabla \cdot \vec{H} = 0 \tag{A.2}$$

$$\nabla \times \vec{H} = -i\epsilon_o \omega \vec{E} \tag{A.3}$$

$$\nabla \times \vec{E} = i\mu_o \omega \vec{H} \tag{A.4}$$

By taking the curl of Eq. (A.3) and making use of Eq. (A.4) on the right hand side results in

$$\left(\nabla^2 + \mu_0 \epsilon_o \omega^2\right) \vec{H} = 0 \tag{A.5}$$

Similarly, by taking the curl of Eq. (A.4) and making use of Eq. (A.3) on the right hand side yields

$$\left(\nabla^2 + \mu_0 \epsilon_o \omega^2\right) \vec{E} = 0 \tag{A.6}$$

Equations (A.5) and (A.6) are sometimes referred to as the Helmholtz equations.

Assume solutions of the following form, which can be used to describe either traveling or standing waves

$$\vec{E}(x,y,z) = \vec{E}(x,y)e^{\pm ikz} \tag{A.7}$$

$$\vec{H}(x,y,z) = \vec{H}(x,y)e^{\pm ikz} \tag{A.8}$$

Note that the Laplacian operator can be separated into a transverse and longitudinal component and rewritten as

$$\nabla^2 = \nabla_t^2 + \frac{\partial^2}{\partial z} \tag{A.9}$$

Using Eq. (A.9) and the form of the solutions in Eq. (A.7) and Eq. (A.8), the Helmholtz equation reduces to a 2D wave equation

$$\left(\nabla_t^2 + \gamma^2\right) \left\{ \begin{array}{c} \vec{E} \\ \\ \vec{H} \end{array} \right\} = 0 \tag{A.10}$$

where

$$\gamma^2 \equiv \epsilon_o \mu_o \omega^2 - k^2 \tag{A.11}$$

It is useful to rewrite the Maxwell equations in terms of components parallel and transverse to the z-axis. The transverse components of $\vec{E}$ and $\vec{H}$ can then be expressed in terms of E_z and H_z, thereby simplifying the problem considerably

$$\vec{E}_t = \frac{i}{\gamma^2}\left[k\nabla_t \vec{E}_z - \mu_0 \omega \left(\hat{z} \times \nabla_t \vec{H}_z\right)\right] \tag{A.12}$$

$$\vec{H}_t = \frac{i}{\gamma^2}\left[k\nabla_t \vec{H}_z + \epsilon_0 \omega \left(\hat{z} \times \nabla_t \vec{E}_z\right)\right] \tag{A.13}$$

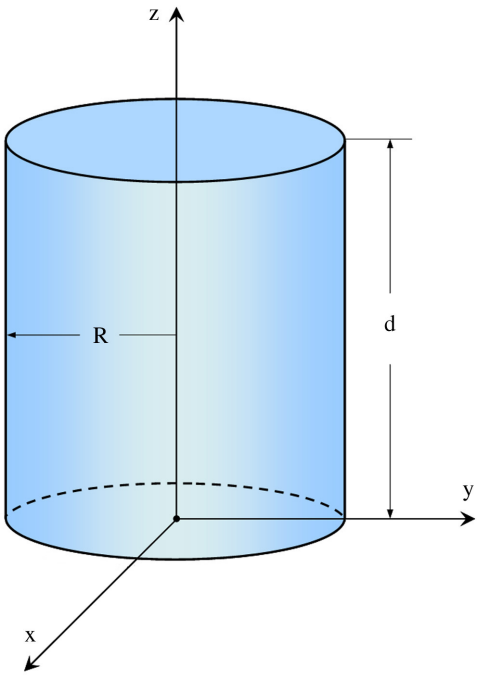

FIG. A.1: A pillbox cavity exhibiting azimuthal symmetry. The resonator has a cross sectional radius R and a length d.

Considering only TM modes, for which $H_z = 0$ everywhere, Eq. (A.12) and Eq. (A.13) reduce to

$$\vec{E}_t = \frac{ik}{\gamma^2}\nabla_t \vec{E}_z \tag{A.14}$$

$$\vec{H}_t = \frac{i\epsilon_0\omega}{\gamma^2}\left(\hat{z} \times \nabla_t \vec{E}_z\right) \tag{A.15}$$

Thus given the longitudinal electric field component, E_z, the remaining electric and magnetic field components can be derived. Up to this point, a cylindrical waveguide of arbitrary (but constant) cross section has been considered. An accelerating cavity is a resonator which is created by placing end plates at $z = 0$ and $z = d$ as shown in Fig. A.1.

Due to the reflections at the end plates, standing waves are created and the z-dependence can be described by

$$E_z(z) = A \sin kz + B \cos(kz) \tag{A.16}$$

The boundary conditions require that the tangential components of $\vec{E}$ must vanish at $z = 0$ and $z = d$. These conditions are satisfied when

$$E_z(\rho, \phi, z) = E_o \cos\left(\frac{p\pi z}{d}\right) \psi(\rho, \phi) \qquad (p = 0, 1, 2, ...) \tag{A.17}$$

where $\psi(\rho, \phi)$ describes the azimuthal dependence of the fields. It follows from Eq. (A.14) and Eq. (A.15) that the transverse components of the electric and magnetic field are given by

$$\vec{E}_t = -\frac{p\pi}{d\gamma^2} \sin\left(\frac{p\pi z}{d}\right) \nabla_t \psi(\rho, \phi) \tag{A.18}$$

$$\vec{H}_t = \frac{i\epsilon_o \omega}{\gamma^2} \cos\left(\frac{p\pi z}{d}\right) [\hat{z} \times \nabla_t \psi(\rho, \phi)] \tag{A.19}$$

The problem can be simplified further by taking advantage of the azimuthal symmetry in the problem and writing

$$\psi(\rho, \phi) = \psi(\rho) e^{\pm im\phi} \tag{A.20}$$

where m is an integer. Substituting Eq. (A.20) into Eq. (A.10) yields

$$\frac{d^2\psi}{d\rho^2} + \frac{1}{\rho}\frac{d\psi}{d\rho} + \left(\gamma^2 - \frac{m^2}{\rho^2}\right)\psi = 0 \tag{A.21}$$

which is Bessel's equation and whose solutions are Bessel functions of order m and denoted as $J_m(\gamma\rho)$. One of the solutions diverges for $\rho = 0$ which is physically unacceptable and so this solution is disregarded.

From Eq. (A.17), Eq. (A.20) and the solution to Eq. (A.21), E_z can be written as

$$E_z(\rho,\phi) = \psi(\rho,\phi) = E_0 J_m(\gamma\rho)e^{im\phi} \tag{A.22}$$

Applying the condition that at $E_z(\rho = R) = 0$ requires $J_m(\gamma R) = 0$. Define $x_{mn} \equiv \gamma_{mn} R$ as the n^{th} root of the Bessel function of order m. Finally, the two components of primary interest, E_z and H_ϕ for TM_{mn0} modes, are given by

$$\begin{aligned} E_z(\rho,\phi,z) &= E_0 J_m\left(\frac{x_{mn}\rho}{R}\right)\cos(m\phi) && \text{(A.23)} \\ H_\phi(\rho,\phi,z) &= \left(\frac{i\epsilon_o\omega_{mn0}}{\gamma_{mn}^2}\right)\frac{\partial E_z}{\partial\rho} && \text{(A.24)} \\ &= iE_0\left(\frac{\epsilon_0\omega_{mn0}R}{x_{mn}}\right)J_m'\left(\frac{x_{mn}\rho}{R}\right)\cos(m\phi) && \text{(A.25)} \end{aligned}$$

where the eigenfrequencies are determined by combining Eq. (A.11) and the definition of x_{mn} to give

$$\omega_{mn0} = \frac{1}{\sqrt{\mu_o\epsilon_o}}\frac{x_{mn}}{R} \tag{A.26}$$

The two important properties of TM_{110} modes in particular, are that

1. $E_z \propto \rho$

2. H_ϕ is nonzero for $\rho = 0$

The first property is due to the fact that J_1 is linear for small values of ρ which means that E_z grows linearly with off-axis displacement. The second property implies that a beam bunch traveling on-axis can still be deflected by the magnetic field since $J_1'(0) \neq 0$.

APPENDIX B

Network Analyzer

A network analyzer (NWA) is one of the most important instruments used for making microwave measurements. A network analyzer measures the response of the device under test (DUT) to an applied sinusoidal input over a range of frequencies [97]. For a given input, the incident wave is reflected, transmitted and attenuated or amplified. The normalized (by the square root of the characteristic impedance) reflected voltages from ports 1 and 2 can be written as a linear combination of the incident waves as

$$V_{R,1} = \mathrm{S}_{11} V_{I,1} + \mathrm{S}_{12} V_{I,2} \tag{B.1}$$

$$V_{R,2} = \mathrm{S}_{21} V_{I,1} + \mathrm{S}_{22} V_{I,2} \tag{B.2}$$

where the S_{ij} are the scattering or S-parameters and refer to the ratio of the reflected voltage from port i to the incident voltage from port j. A schematic illustrating how the S-parameters are related to the incident and reflected voltages from each port is shown in Fig. B.1.

In terms of accelerator applications, one of the most common uses of a NWA is making an S_{21}, or transmission, measurement of RF cavities. The DUT is the RF

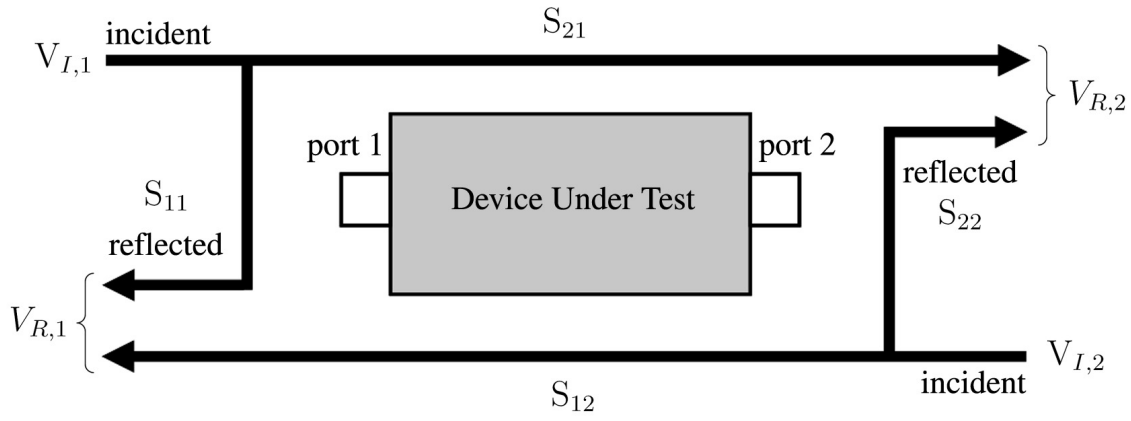

FIG. B.1: Relationship of the S-parameters in terms of the incident and reflected voltages from ports 1 and 2 for a network analyzer.

cavity and there are several ways to couple power in and out of the cavity. Given the easy access to the HOM coupler ports of the zone 3 cryomodule, oftentimes the HOM1 port was connected to port 1 of the NWA and the HOM2 port was connected to port 2 of the NWA. The scattering parameter S_{21} is a measure of the power emerging from port 2 as a result of applying an RF signal to port 1. The output of the NWA displays the amplitude ratio versus the frequency. Near the frequency of a resonant mode, the transmission becomes large and, depending on the Q of the mode, rapidly decreases as the frequency deviates from the resonant frequency. A screenshot from a NWA of a typical S_{21} measurement on an SRF cavity is shown in Fig. 4.6. This type of measurement was used to determine the loaded quality factors of the dipole modes in the zone 3 and was also the setup used for the beam transfer function measurement in the experimental studies of BBU (see Section 5.4.3).

APPENDIX C

Zone 3 HOM Impedances and Frequencies

The results of the HOM measurements in zone 3 are summarized graphically by plotting the impedance of each mode, $(R_d/Q_o)Q_L$, as a function of HOM frequency for all 8 cavities.

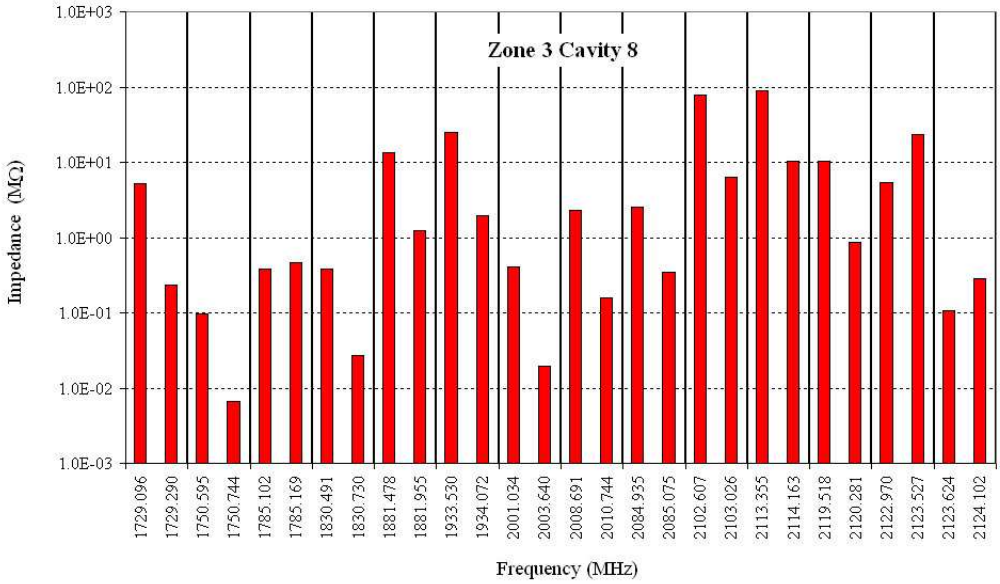

FIG. C.1: Impedance and frequency of dipole HOMs in zone 3 cavity 8.

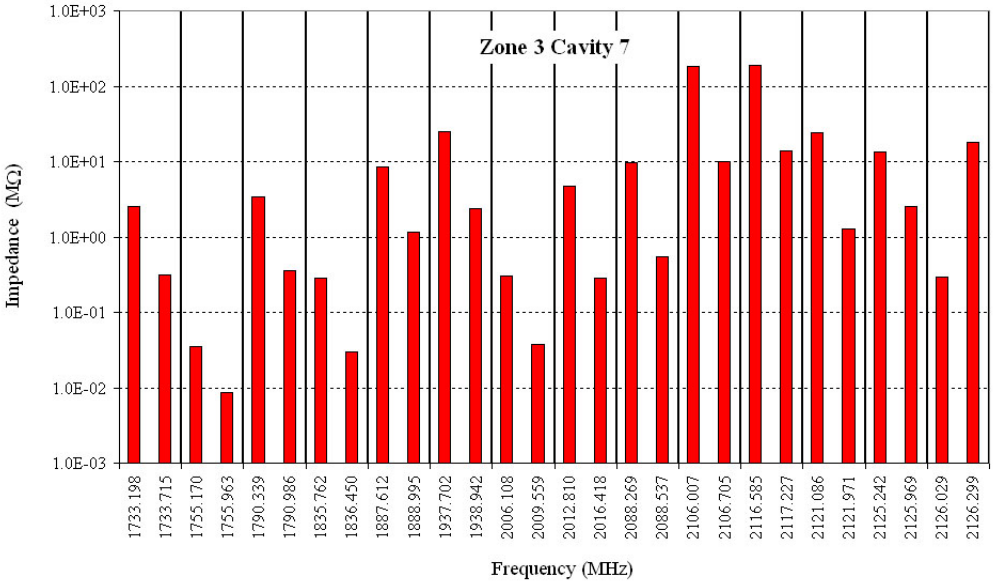

FIG. C.2: Impedance and frequency of dipole HOMs in zone 3 cavity 7.

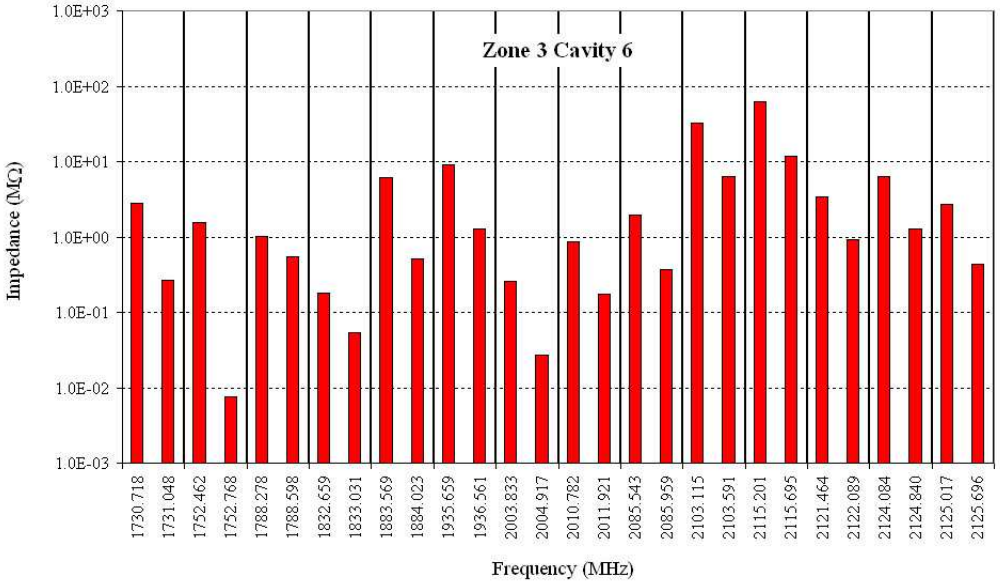

FIG. C.3: Impedance and frequency of dipole HOMs in zone 3 cavity 6.

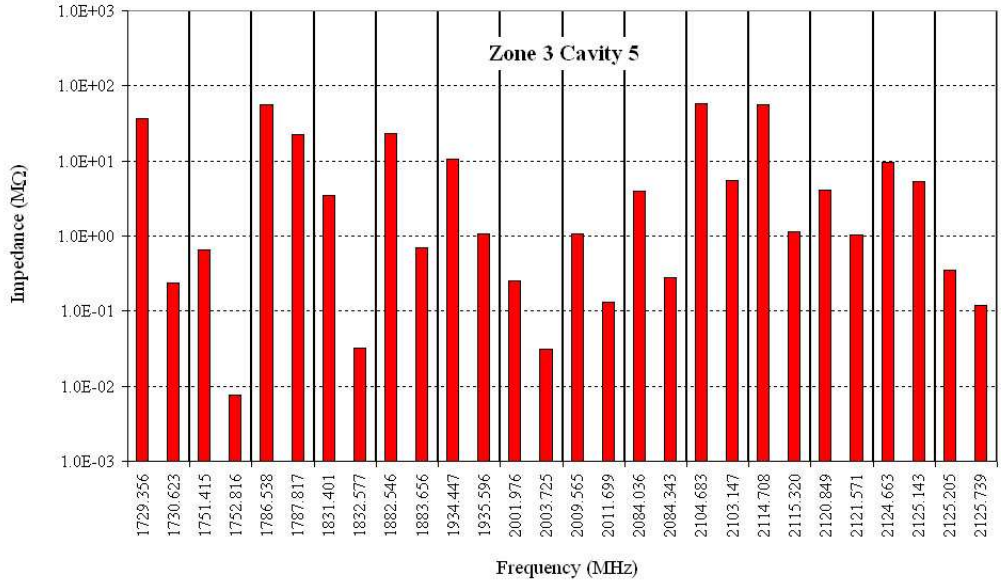

FIG. C.4: Impedance and frequency of dipole HOMs in zone 3 cavity 5.

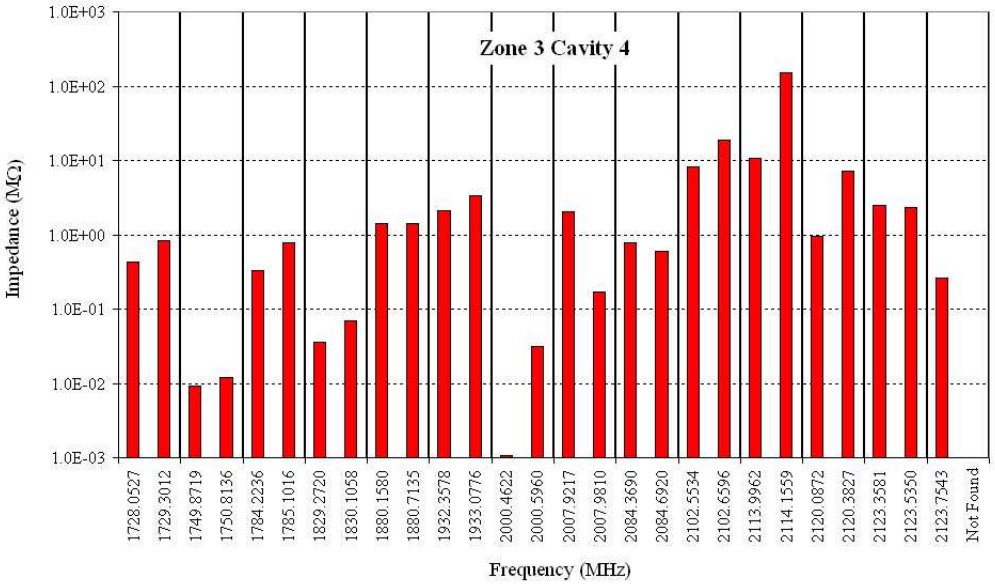

FIG. C.5: Impedance and frequency of dipole HOMs in zone 3 cavity 4.

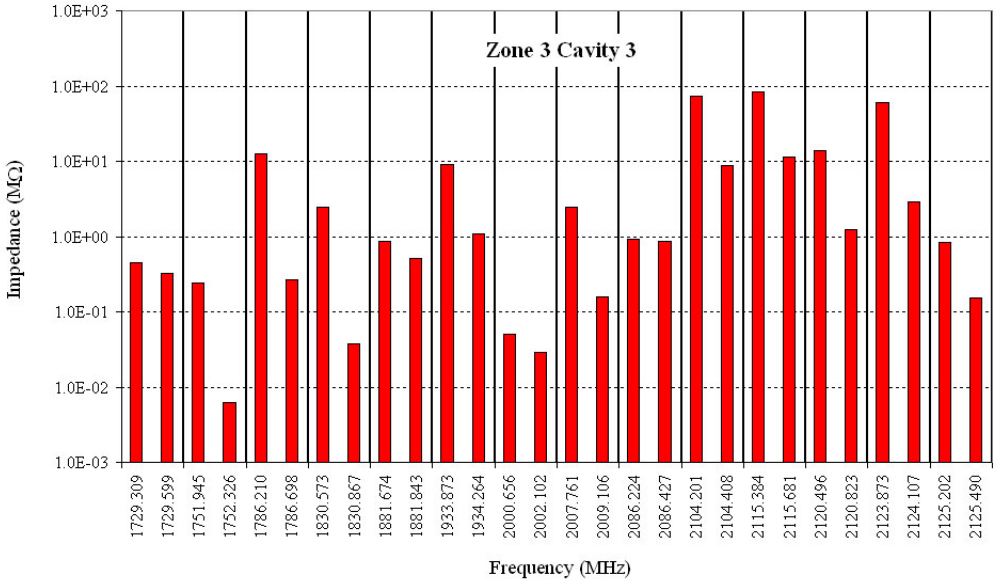

FIG. C.6: Impedance and frequency of dipole HOMs in zone 3 cavity 3.

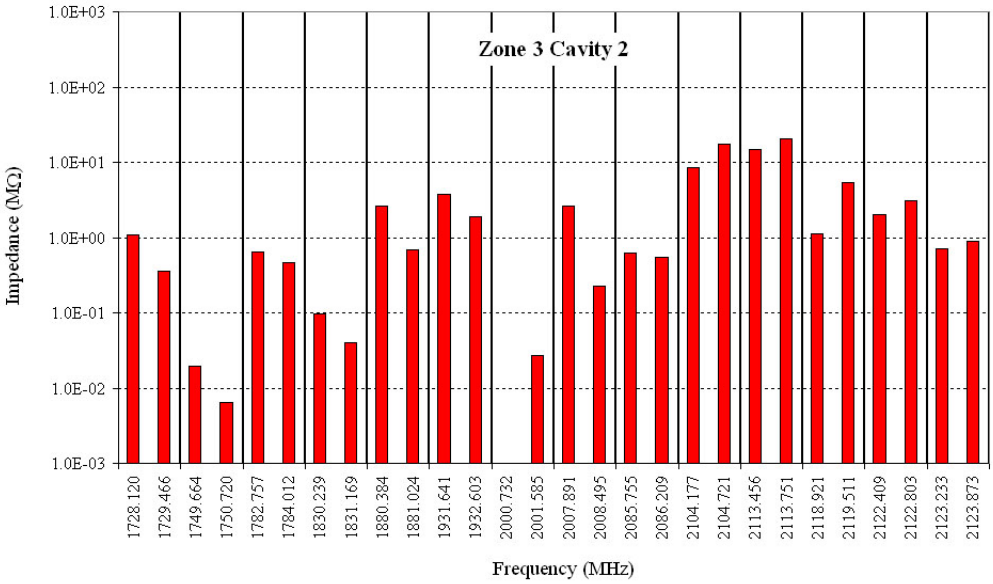

FIG. C.7: Impedance and frequency of dipole HOMs in zone 3 cavity 2.

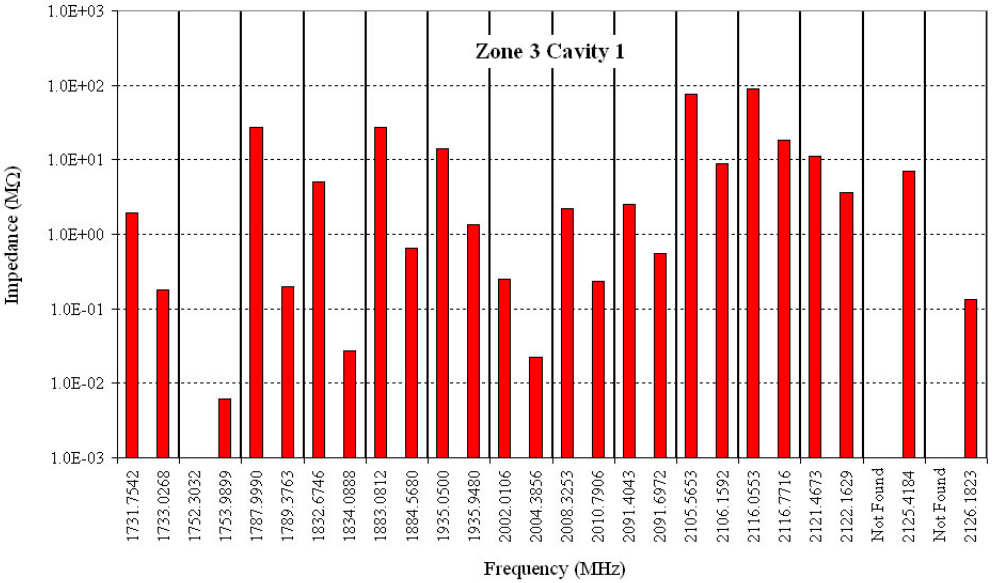

FIG. C.8: Impedance and frequency of dipole HOMs in zone 3 cavity 1 .

BIBLIOGRAPHY

[1] M. Tigner, Nuovo Cimento **37**, 1228 (1965).

[2] H. Padamsee, J. Knobloch, and T. Hays, *RF Superconductivity for Accelerators*, Wiley Series in Beam Physics and Accelerator Technology (John Wiley and Sons, Inc., 1998), ISBN 0-471-15432-6.

[3] J. Preble, Talk presented at ONR\NAVSEA FEL Upgrade Review, Newport News, VA (2004).

[4] G. Krafft and L. Merminga, unpublished.

[5] L. Merminga, D. Douglas, and G. Krafft, Annu. Rev. Nucl. Part. Sci. **53**, 387 (2003).

[6] S. Schriber et al., in *Proceedings of the Particle Accelerator Conference, Chicago, IL, 1977* (IEEE, Piscataway, NJ, 1977), pp. 1061–1063.

[7] J. Flanz and C. Sargent, in *Proceedings of the Particle Accelerator Conference, Vancouver, British Columbia, 1985* (IEEE, Piscataway, NJ, 1985), pp. 3213–3215.

[8] T. Smith et al., Nucl. Instrum. Methods A **259**, 1 (1987).

[9] D. Feldman et al., in *Proceedings of the Particle Accelerator Conference, Washington, DC, 1987* (IEEE, Piscataway, NJ, 1987), pp. 221–223.

[10] M. Brittan et al., in *Proceedings of the 10th International Conference on High Energy Accelerators, Serpukov, USSR, 1977* (1977), pp. 283–292.

[11] C. Lyneis et al., in *Proceedings of the Particle Accelerator Conference, San Francisco, CA, 1979* (IEEE, Piscataway, NJ, 1979), pp. 3246–3248.

[12] Report Project 87-R-203, Continuous Electron Beam Accelerator Facility (1985).

[13] N. Sereno et al., in *Proceedings of the Particle Accelerator Conference, Washington, DC, 1993* (IEEE, Piscataway, NJ, 1993), pp. 3246–3248.

[14] N. Sereno, Ph.D. thesis, University of Illinois at Urbana-Champaign (1994).

[15] G. Krafft and J. Bisognano, in *Proceedings of the Particle Accelerator Conference, Chicago, IL, 1989* (IEEE, Piscataway, NJ, 1989), pp. 1256–1258.

[16] R. Rohatgi, H. Schwettman, and T. Smith, in *Proceedings of the Particle Accelerator Conference, Washington, DC, 1987* (IEEE, Piscataway, NJ, 1987), pp. 230–232.

[17] D. Douglas et al., Technical Note 91-017, Jefferson Laboratory (1991).

[18] G. Neil et al., Phys. Rev. Lett. **84** (2000).

[19] D. Douglas, Technical Note 01-018, Jefferson Laboratory (2001).

[20] C. Tennant et al., in *Proceedings of the 11th Workshop on RF Superconductivity, Travemunde, Germany, 2003* (2003).

[21] S. Benson et al., in *Proceedings of the Free Electron Laser Conference, Trieste, Italy, 2004* (Comitato Conferenze Elettra, 2004), pp. 229–232.

[22] L. Merminga, in *Proceedings of the European Particle Accelerator Conference, Lucerne, Switzerland, 2004* (2004), pp. 16–20.

[23] A. Todd, Nucl. Instrum. Methods A **557**, 36 (2005).

[24] C. Hernandez-Garcia et al., in *Proceedings of the Particle Accelerator Conference, Knoxville, TN, 2005* (IEEE, Piscataway, NJ, 2005), pp. 3117–3119.

[25] M. Liepe and J. Knobloch, Nucl. Instrum. Methods A **557**, 354 (2005).

[26] J. Bisognano and R. Gluckstern, in *Proceedings of the Particle Accelerator Conference, Washington, DC, 1987* (IEEE, Piscataway, NJ, 1987), pp. 1078–1080.

[27] P. Axel et al., in *Proceedings of the Particle Accelerator Conference, San Francisco, CA, 1979* (IEEE, Piscataway, NJ, 1979), pp. 3143–3145.

[28] C. Tennant et al., Phys. Rev. ST Accel. Beams **8**, 074403 (2005).

[29] C. Leemann, D. Douglas, and G. Krafft, Annu. Rev. Nucl. Part. Sci. **51**, 413 (2001).

[30] R. York and D. Douglas, in *Proceedings of the Particle Accelerator Conference, Washington, DC, 1987* (IEEE, Piscataway, NJ, 1987), pp. 1292–1294.

[31] Z. Li, Ph.D. thesis, College of William and Mary (1995).

[32] D. Douglas, Presentation at CEBAF-ER working group meeting (2003).

[33] R. York and C. Reece, in *Proceedings of the Particle Accelerator Conference, Washington, DC, 1987* (IEEE, Piscataway, NJ, 1987), pp. 1307–1309.

[34] M. Tiefenback, Comments in accelerator physics group meeting (2001).

[35] M. Tiefenback, CEBAF ELOG 1140939 (2003).

[36] M. Tiefenback, Talk presented at Tesla Collaboration Meeting, Frascati, Italy (2003).

[37] J. Walecka, *Fundamentals of Statistical Mechanics: Manuscript and Notes of Felix Bloch* (Imperial College Press and World Scientific, 2000), ISBN 981-02-4420-7.

[38] S. Lee, *Accelerator Physics* (World Scientific, 1999), ISBN 981-02-3710-3.

[39] http://www.jlab.org/accel/beam_diag/harp/harp_dummy.html.

[40] Igor Pro (http://www.wavemetrics.com/).

[41] Optim (http://www-bdnew.fnal.gov/pbar/organizationalchart/lebedev/OptiM/optim.htm).

[42] M. Fripp and D. Douglas, Technical Note 91-052, Jefferson Laboratory (1991).

[43] P. Kloeppel, Technical Note 89-191, Jefferson Laboratory (1989).

[44] R. Servranckx et al., SLAC Report No. SLAC-R-285, SLAC (1990).

[45] M. Tiefenback, Private communication (2006).

[46] A. Freyberger, in *Proceedings of the 7th European Workshop on Beam Diagnostics and Instrumentation for Particle Accelerators, Lyon, France, 2005* (2005), pp. 12–16.

[47] D. Douglas, Private communication (2003).

[48] G. Krafft et al., in *Proceedings of the 20th International Linac Conference, Monterey, CA, 2000* (2000), pp. 721–725.

[49] D. Douglas, Technical Note 00-012, Jefferson Laboratory (2000).

[50] C. Hernandez-Garcia et al., in *Proceedings of the 26th International Free Electron Laser Conference, Trieste, Italy, 2004* (Comitato Conferenze Elettra, 2004), pp. 558–561.

[51] C. Hernandez-Garcia et al., in *Proceedings of the 26th International Free Electron Laser Conference, Trieste, Italy, 2004* (Comitato Conferenze Elettra, 2004), pp. 363–366.

[52] J. Flanz and C. Sargent, Nucl. Instrum. Methods A **241**, 325 (1985).

[53] D. Douglas, Private communication (2006).

[54] D. Douglas, Talk presented at 32$^{\text{nd}}$ Advanced ICFA Beam Dynamics Workshop on ERLs, Newport News, VA (2005).

[55] D. Douglas, Technical Note 01-024, Jefferson Laboratory (2001).

[56] D. Douglas and C. Tennant, Technical Note 01-043, Jefferson Laboratory (2001).

[57] D. Douglas, FEL FLOG 1167311 (2003).

[58] D. Douglas, Technical Note 00-013, Jefferson Laboratory (2000).

[59] D. Douglas et al., Technical Note 95-015, Jefferson Laboratory (1995).

[60] P. Piot, D. Douglas, and G. Krafft, Phys. Rev. ST Accel. Beams **6**, 030702 (2003).

[61] D. Douglas, Private communication (2006).

[62] P. Evtushenko, FEL FLOG 1314073 (2006).

[63] J. Bisognano and M. Fripp, in *Proceedings of the Linac Conference, Newport News, VA, 1988* (1988), pp. 388–390.

[64] L. Merminga, Nucl. Instrum. Methods A **483**, 107 (2002).

[65] E. Pozdeyev, Phys. Rev. ST Accel. Beams **8**, 054401 (2005).

[66] E. Pozdeyev, Private communication (2005).

[67] G. Krafft, J. Bisognano, and S. Laubach, unpublished.

[68] B. Yunn, in *Proceedings of the Particle Accelerator Conference, San Francisco, CA, 1991* (IEEE, Piscataway, NJ, 1991), pp. 1785–1787.

[69] G. Hoffstaetter and I. Bazarov, Phys. Rev. ST Accel. Beams **7**, 054401 (2004).

[70] G. Krafft and J. Bisognano, in *Proceedings of the Particle Accelerator Conference, Washington, DC, 1987* (IEEE, Piscataway, NJ, 1987), pp. 1356–1358.

[71] K. Beard, Technical Note 02-045, Jefferson Laboratory (2002).

[72] B. Yunn, Phys. Rev. ST Accel. Beams **8**, 104401 (2005).

[73] K. Beard, Technical Note 02-044, Jefferson Laboratory (2002).

[74] Z. Li, L. Ge, and K. Ko, Presentation at Collaboration Meeting of JLab-SLAC Computer Simulations on SRF Structures (2005).

[75] H. Wang et al., in *Proceedings of the Particle Accelerator Conference, Portland, OR, 2003* (IEEE, Piscataway, NJ, 2003), pp. 1104–1106.

[76] I. Campisi and L. Merminga, Technical Note 98-011, Jefferson Laboratory (1998).

[77] K. Jordan, Private communication (2004).

[78] Herotek, Inc. (http://www.herotek.com/).

[79] L. Merminga et al., in *Proceedings of the Particle Accelerator Conference, Chicago, IL, 2001* (IEEE, Piscataway, NJ, 2001), pp. 173–175.

[80] A. Vetter, Ph.D. thesis, Stanford University (1980).

[81] K. Mittag et al., Nucl. Instrum. Methods **76**, 245 (1969).

[82] D. Sagan and J. Smith, in *Proceedings of the Particle Accelerator Conference, Knoxville, TN, 2005* (IEEE, Piscataway, NJ, 2005), pp. 4159–4161.

[83] I. Bazarov and G. Hoffstaetter, in *Proceedings of the European Particle Accelerator Conference, Lucerne, Switzerland, 2004* (2004), pp. 2194–2196.

[84] R. Rand and T. Smith, Part. Accel. **11**, 1 (1980).

[85] D. Douglas, in *Proceedings of the Particle Accelerator Conference, San Francisco, CA, 1991* (IEEE, Piscataway, NJ, 1991), pp. 449–451.

[86] D. Douglas, Technical Note 04-017, Jefferson Laboratory (2004).

[87] D. Douglas, Technical Note 04-016, Jefferson Laboratory (2004).

[88] D. Douglas, Technical Note 04-025, Jefferson Laboratory (2004).

[89] C. Tennant and E. Pozdeyev, Technical Note 04-020, Jefferson Laboratory (2004).

[90] E. Pozdeyev, Talk presented at 32$^{\text{nd}}$ Advanced ICFA Beam Dynamics Workshop on ERLs, Newport News, VA (2005).

[91] G. Hoffstaetter, I. Bazarov, and C. Song, physics/0508089 (2006).

[92] S. Benson, FEL FLOG 1345135 (2006).

[93] D. Douglas, Technical Note 04-023, Jefferson Laboratory (2004).

[94] B. Yunn, in *Proceedings of the European Particle Accelerator Conference, Lucerne, Switzerland, 2004* (2004), pp. 2218–2220.

[95] G. Krafft, Private communication (2006).

[96] G. Krafft, Phys. Rev. ST Accel. Beams **7**, 060704 (2004).

[97] J. Byrd and F. Casper, *Beam Measurements* (World Scientific, 1999), ISBN 981-02-3881-9.

VITA

Christopher D. Tennant

Christopher Daniel Tennant was born June 25, 1979 in Sidney, NY. He graduated from Bainbridge-Guilford High School in Bainbridge, New York in June of 1997. He graduated *summa cum laude* with a Bachelor of Arts in physics and a minor in mathematics from Ithaca College in Ithaca, New York in May 2001. He received a Master of Science degree in physics from the College of William and Mary in Williamsburg, Virginia in December 2002. This dissertation was defended on October 26, 2006 at the College of William and Mary in Virginia.

STUDIES OF ENERGY RECOVERY LINACS AT JEFFERSON LABORATORY

1 GeV Demonstration of Energy Recovery at CEBAF and Studies of the Multibunch, Multipass Beam Breakup Instability in the 10 kW FEL Upgrade Driver

ABSTRACT

An energy recovering linac (ERL) offers an attractive alternative for generating intense electron beams by approaching the operational efficiency of a storage ring while maintaining the superior beam quality typical of a linear accelerator. Two primary physics challenges exist in pushing the frontier of ERL performance. The first is energy recovering a high energy beam while demonstrating operational control of two coupled beams in a common transport channel. The second is controlling the high average current effects in ERLs, specifically a type of beam instability called multipass beam breakup (BBU). This work addresses each of these issues.

A successful 1 GeV energy recovery demonstration with a maximum-to-injection energy ratio of 51:1 was carried out on the Continuous Electron Beam Accelerator Facility at Jefferson Laboratory in an effort to address issues related to beam quality preservation in a large scale system. With a 1.3 km recirculation length and containing 312 superconducting radio frequency (SRF) cavities, this experiment has demonstrated energy recovery on the largest scale, and through the largest SRF environment, to date.

The BBU instability imposes a potentially severe limitation to the average current that can be accelerated in an ERL. Simulation results for Jefferson Laboratory's 10 kW free electron laser (FEL) Upgrade Driver predict the occurrence of BBU below the nominal operating current. Measurements of the threshold current are described and shown to agree to within 10% of predictions from BBU simulation codes. This represents the first time the codes have been benchmarked with experimental data. With BBU limiting the beam current, several suppression schemes were developed. These include direct damping of the higher-order mode using two different cavity-based feedbacks and modifying the electron beam optics. Each method increased the threshold current for stability. Beam optical control methods proved to be so effective that they are routinely used in normal operation of the 10 kW FEL Upgrade.

CHRISTOPHER D. TENNANT

DEPARTMENT OF PHYSICS

THE COLLEGE OF WILLIAM AND MARY IN VIRGINIA

KEITH GRIFFIOEN

PROFESSOR OF PHYSICS